This electronic thesis or dissertation has been downloaded from the King's Research Portal at https://kclpure.kcl.ac.uk/portal/

A structural approach to investigate glycation effect on protein aggregation

Milordini, Giulia

Awarding institution:
King's College London

The copyright of this thesis rests with the author and no quotation from it or information derived from it may be published without proper acknowledgement.

END USER LICENCE AGREEMENT

Unless another licence is stated on the immediately following page this work is licensed under a Creative Commons Attribution-NonCommercial-NoDerivatives 4.0 International licence. https://creativecommons.org/licenses/by-nc-nd/4.0/

You are free to copy, distribute and transmit the work

Under the following conditions:

- Attribution: You must attribute the work in the manner specified by the author (but not in any way that suggests that they endorse you or your use of the work).
- Non Commercial: You may not use this work for commercial purposes.
- No Derivative Works - You may not alter, transform, or build upon this work.

Any of these conditions can be waived if you receive permission from the author. Your fair dealings and other rights are in no way affected by the above.

Take down policy

If you believe that this document breaches copyright please contact librarypure@kcl.ac.uk providing details, and we will remove access to the work immediately and investigate your claim.

Download date: 07. Jan. 2025

A structural approach to investigate glycation effect on protein aggregation

Giulia Milordini

Thesis submitted for the degree of
Doctor of Philosophy

Department of Basic and Clinical Neuroscience
Institute of Psychiatry, Psychology and Neuroscience
King’s College London
2019

1st supervisor: Prof Annalisa Pastore

2nd supervisor: Dr Rivka Isaacson

To my family and to Alberto,
who supported me unconditionally.

Acknowledgments

Nothing in life is to be feared, it is only to be understood.
Now is time to understand more, so that we may fear less.
Marie Sklodowska Curie

I would like to thank my first supervisor, Annalisa Pastore who was with me from the start of my PhD journey and who gave me this unique opportunity to work in the amazing field of structural biology, and who believed on me and supported me during difficult times. I would also like to thank Rivka Isaacson, my second supervisor for her support and her encouragement.

I'd also like to thank my parents for being so encouraging and having faith in me, and for instilling a love of learning and a freedom to choose my own path. I really appreciate how much they encouraged me in all of my pursuits and inspired me to choose my own path. I want to thank my mum, who taught me what feminism is without labelling it, and my dad, who supported me emotionally.

I am especially grateful to Alberto who accepted my choices and supported me in this journey despite living in different countries. I always knew you believed in me and that you wanted the best for us. Thanks too to my sister Sveta, with who I share an incredibly strong bond and who gave me the chance to be part of Vladik's life, the sweetest creature in the world.

This work would not have been possible without the members of Pastore lab, both past and present, who have been such a big part of the past few years, providing me with their support, friendship and so many fun times. In particular, I owe a debt of gratitude to Dr Elsa Zacco, Dr Tommaso Vannocci and Dr Rita Puglisi taking time out of their busy days to help me with my thesis.

To Elsa, my friend who inspires me every day and helps me to improve to be a better person, thank you for all that you taught me, both in the lab and out. I cannot be more grateful for being part of your life. To Tommaso, who taught me about beer, about English culture and a lot about Sciences, thank you for making the trips to the Diamonds super fun. You are the fun scientist everyone wants to work with. To Rita, my running mate, who taught me about NMR and a lot more, thank you for chats and your positivity.

To Dr Alessandro Sicorello, thank you for being so supportive, open exploring new ideas and always there for a chilled beer. To my sweetest lab mates, Martina Gilodi, Anna Fricano, Chiara Beghè, Francesca Venturella and Emanuele Astoricchio, it has been a wonderful pleasure to work with you who have helped me so much and brightened my days here. To Caterina and Domenico, thank you for showing me that though this job is tough, it's worth it.

The past four years have been made wonderful by the friendship of so many people, including Martina de Majo, Natalias Arias, Joana Furtado, Jenny Craig, Seb Paulisson, Silvia Rota, Isabella Premoli, Alfredo Iaconelli, Andrea Biondi and many others. I am grateful to Jean-Marc Gallo, a very inspirational person, for his valuable support and reassurance.

I would like to give special thanks to Saviana, my partner in crime, a true friend who does not need a word to understand me and who made the past year a truly amazing and memorable experience; to Giacomo, my buddy from the beginning of this journey, perfect running mate, amazing cook, opera expert and authentic friend with a big heart; to Maria, my smart, sophisticated and extremely generous friend, who has always been there for me; to Giuseppe, dear friend, both a super fun and inspiring man; to Greta and Giulia, my friends since we were tiny for so many amazing memories teaching me that friendship lasts no matter where we live.

I would particularly like to mention the wonderful friendship of my friend Cristina, the girl I met by coincidence on a random bus, in a random day. I never imagined I would have found such an empowering and inspiring woman. Thank you for helping me to find confidence that I did not know I had. Thank you to Francesca, one of the most generous, friendly and active persons I have ever met. Your love for life is just contagious. Thanks to my dear friend Giulia G who shared the PhD path with me and the ups and downs along the way. You are such a delight to be with. Thank you Marella and Mirko for the fun nights out and for showing the world that success does not exclude love in life.

Special thanks to Max, the most respectful, coherent and upright person but also generous who opened his house with Elsa to me when I was homeless or just lonely. To Ambra, thank you for the yoga lessons, the fun moments, your smart suggestions and mainly your friendship. To Leo, my official English teacher, thank you for making the effort to teach me English expressions and working on my pronunciation. To Ross, thank you for being so caring and for sharing your projector to watch Juventus and Liverpool together.

I owe a debt of gratitude to the Spanish community who adopted me in London: Ana and Paula, my friends who taught me that Erasmus life can be forever. I will never forget you shared your house when I had no place to stay. Thank you for your sweet words and for making me feel part of your family. To Elena, thank you not just for partying together but also for listening and supporting me in my decisions.

This work would also not have been possible without Diabetes UK and the Dementia Research Institute and who are ultimately the driving force behind this work. I am also very grateful to EMBO and BIRAX for the short-term fellowships to continue my work in collaborations with great international institutions abroad.

Author’s declaration

I hereby declare that, as the author of this thesis, this work is my own composition and the work reported here was performed by myself unless otherwise stated. This work has not been submitted for any other degree.

Content, quotes or images previously published by third parties are indicated by referring to the original work. Additional contributions are reported below:

- AFM micrographs have been acquired with the help of Dr Richard Thorogate at the London centre for nanotechnology at University College London.
- MS spectra have been acquired by Dr Fabrizio Dal Piaz at the University of Salerno (Italy).
- The work presented in this dissertation resulted in the following publication:
  G. Milordini#, A. Emendato#, E. Zacco, F. Dal Piaz, M Adrover, R. Guerrini, A. Pastore, D. Picone. Glycation affects fibril formation of Aβ peptides. J Biol Chem. 2018 24;293(34):13100-13111G #These authors have equally contributed.

Table of contents

Abbreviations

This is a list of the useful abbreviations I used in my thesis:

Abeta	Amyloid beta peptide
Abeta40	Abeta(1-40)
Abeta42	Abeta(1-42)
AD	Alzheimer’s disease
AFM	Atomic force microscopy
AGE	Advanced glycation end-product
AICD	APP intracellular C-terminal domain
APP	Amyloid precursor protein
ArgP	Argpyrimidine
C	Concentration
CBD	Chitin-binding domain
CD	Circular dichroism
CEL	Nε-carboxyethyl-lysine
CML	Nε-carboxymethyl-lysine
CMC	Critical micelle concentration
Cryo-EM	Cryo-electron microscopy
C99	C-terminal fragment

Da	Dalton
Dihydroxyacetone-3-P	Dihydroxyacetone-3-phospate
DMSO	Dimethyl sulfoxide
DSS	4,4-dimethyl-4-silapentane-1-sulfonic acid
EM	Electron microscopy
E. coli	*Escherichia coli*
EPR	Electron paramagnetic resonance
ESI	Electrospray ionisation
Fructose-1,6-bis-P	Fructose-1,6-bisphophate
Glyceraldehyde-3-P	Glyceraldehyde-3-phospate
HFIP	1,1,1,3,3,3-hexafluoro-2-propanol
HPLC	High-performance liquid chromatography
IAPP	Islet amyloid polypeptide
IDP	Intrinsically disordered protein
IPTG	Isopropyl-beta-D-thiogalactopyranoside
l	Optical path length
LB	Luria-Bertani medium
LC-MS	Liquid chromatography–mass spectrometry
Lcp	Left-handed circularly polarised light

MALDI	Matrix-assisted laser desorption/ionisation
MS	Mass spectrometry
MGO	Methylglyoxal
MW	Molecular weight
NMR	Nuclear magnetic resonance
NOESY	Nuclear Overhauser effect spectroscopy
OD	Optical density
ppm	Parts per million
PTM	Post-translational modification
PBS	Phosphate-buffered saline
PDB	Protein data bank archive
RAGE	Receptor for AGEs
Rcp	Right-handed circularly polarised
rIAPP	Rat orthologue of Islet amyloid polypeptide
ROS	Reactive oxygen species
SCOP	Structural classification of proteins
SDS	Sodium dodecyl sulphate
SDS -PAGE	Sodium dodecyl sulphate–polyacrylamide gel electrophoresis)
ssNMR	Solid-state nuclear magnetic resonance

STEM	Scanning transmission electron microscope
TFA	Trifluoracetic acid
ThT	Thioflavin T
TMD	Transmembrane domain
TOCSY	Total correlation spectroscopy
T2D	Type 2 diabetes
2D-NMR	Two-dimensional nuclear magnetic resonance
^{1}H NMR	Proton-nuclear magnetic resonance

Index of tables

Index of figures

1. Introduction

3. Techniques employed

4. Results - Abeta

5. Results - IAPP

Index of schemes

Abstract

The increase in life expectancy observed over the last century has led to the emergence of a new set of pathologies that constitutes a new threat for the world population. Among these pathologies, neurodegenerative diseases have gained an increased impact on society. Despite originating from different genetic, environmental and regulatory factors, many neurodegenerative disorders show similarities at sub-cellular and molecular levels. A characteristic common feature of ageing-related diseases is the self-assembly of misfolded proteins into neurotoxic oligomers and fibrils, which are resistant to degradation and lack the functionality of the native protein.

Among these increasingly concerning diseases, Alzheimer's disease (AD) affects over 80 individuals every day. Substantial epidemiological evidence shows an increased risk for developing AD in people affected by diabetes, which is associated with increased hyperglycaemia. The molecular mechanisms underlying the link between diabetes and AD remain elusive. For this reason, when approaching the study of AD, it is essential to consider the role that sugars play in disease development and, therefore, the role of post-translational modifications such as glycation. Contrary to glycosylation, glycation is an enzyme-free reaction that leads to attachment of a carbohydrate molecule to the protein and the formation of advanced glycation end-products (AGEs). Glycation is one of the pathological processes involved in diabetes and is thought to influence the structure of the islet amyloid polypeptide (IAPP), which plays a role in glycaemic regulation. Misfolded IAPP aggregates into toxic amyloid-like structures, very similar to the Abeta peptide (variants 1-40 and 1-42) deposits, often also heavily glycated, observed in AD patients.

The aim of this thesis is to unravel the effects of glycation on the structure and aggregation of the peptides IAPP and two of the most common variants of Abeta by means of an integrative structural approach.

Several biophysical techniques were employed to gain insights into the structural effects of glycation on the aggregation process of the IAPP and Abeta peptides. The occurrence and location of the glycation reaction was elucidated by mass spectrometry. The secondary structure variations upon glycation were observed by circular dichroism and nuclear magnetic resonance. Spectrofluorometric assays were employed to follow protein aggregation and glycation concomitantly. Finally, the morphological effects of glycation on amyloid fibrils were evaluated by high-resolution structural atomic force microscopy (AFM) studies.

Introduction

1.1 Protein misfolding and aggregation

Neurodegenerative diseases are an increasing health concern for which there are no treatments for the underlying pathologies. Many, but by no means all, of these diseases, despite having a multitude of different symptoms, are associated with the misfolding of normally soluble, functional peptides and proteins, and their subsequent conversion into intractable aggregates, of which the archetypal examples are amyloid fibrils (**Table 1**) (1). To understand the impact of amyloid diseases on our society, it has been estimated that every 67 seconds someone in the USA develops Alzheimer's disease, while only 45% of these people have been told of this diagnosis. In the UK the cost of Alzheimer's and dementia already exceeded 30 billion pounds, while the global cost of Alzheimer's and dementia is estimated to be around 480 billion pounds.

Table 1. Some human diseases associated with protein misfolding and amyloid aggregation. Modified from (2).

Disease	**Aggregating protein or peptide**	**Number of residues (a)**	**Native structure of protein or peptide (b)**
Neurogenerative disease			
Alzheimer's disease (c)	Amyloid beta peptide	37-43	IDP (e)
Spongiform encephalopathies (c,e)	Prion protein or fragments thereof	230	IDP, alpha-helix
Parkinson's disease (c)	α-Synuclein	140	IDP
Amyotrophic lateral sclerosis (c)	Superoxide dismutase 1	153	Beta-sheet, Ig-like
Huntington's disease (d)	Huntingtin with polyQ expansion	Variable	Mostly IDP
Non-neuropathic systemic amyloidosis			
Amyloid Light chain amyloidosis (c)	Immunoglobulin light chains or fragments	~90	Beta-sheet, Ig-like
Amyloid A amyloidosis (c)	Fragments of serum amyloid A protein	76–104	Alpha-helix and unknown fold
Senile systemic amyloidosis (c)	Wild-type transthyretin	127	Beta-sheet,
Hemodialysis-related amyloidosis (c)	beta2-microglobulin	99	Beta-sheet, Ig-like
Lysozyme amyloidosis (d)	Lysozyme mutants	130	Alpha-helical, beta-sheet
Non-neuropathic localised amyloidosis			
Injection-localised amyloidosis (c)	Insulin	21 and 30	Alpha-helical, insulin like
Type II diabetes (c)	Islet amyloid polypeptide	37	IDP

[a] Data refer to the number of residues of the processed polypeptide chains that deposit into aggregates, not of the precursor protein

[b] According to structural classification of proteins (SCOP), these are the structural class and fold of the native states of the processed peptides or proteins that deposit into aggregates prior to aggregation.

[c] Predominantly sporadic, although in some cases hereditary forms associated with specific mutations are well documented.

[d] Predominantly hereditary, although in some cases sporadic forms are documented.

[e] Intrinsically disordered protein or peptide.

Amyloid fibrils are thread-like structures, the formation of which is associated both with a loss of function of the involved proteins and with the generation of often toxic intermediates (2,3).

Commonly, the formation of amyloid fibrils follows the misfolding, the incorrect folding of the protein. If a molecule of the protein cannot form the correct intramolecular bonds required to fold correctly, it can interact and combine with other molecules to form aggregates. Therefore, protein misfolding and aggregation is the phenomenon by which a natively folded protein undergoes an aberrant conformational transition with subsequent formation of energetically stable, high molecular weight amyloid fibrils (**Fig. 1 A**). Aggregation can be triggered by post-translational modification (PTM) such as protein hyperphosphorylation, by mutations that cause the protein instability or by events that increase a specific protein concentration in the cell (e.g. lack/defect of clearance, chaperone imbalance, etc.).

At the molecular level, amyloids are insoluble protein aggregates, characterised by a cross-beta quaternary structure (4). The reaction mechanism is not usually a simple transition from monomer to fibril. Most of the time, the transition between monomer and fibril has an intermediate step characterised by soluble prefibrillar oligomers that can vary in size, structure, stability and toxicity (1). An aggregated state represents a state of minimum free energy and is the theoretically most stable state for the majority of proteins (5). The aggregated conformation is energetically favourable, due to the minimum of free energy that is reached; however, it is blocked by a high-energy barrier (**Fig. 1 B**). The beta sheet structures allow the formation of a large number of intermolecular hydrogen bonds, which are energetically very favourable (**Fig. 1 C**). Thus, the main driving force for the formation of amyloid fibrils is their high thermodynamic stability.

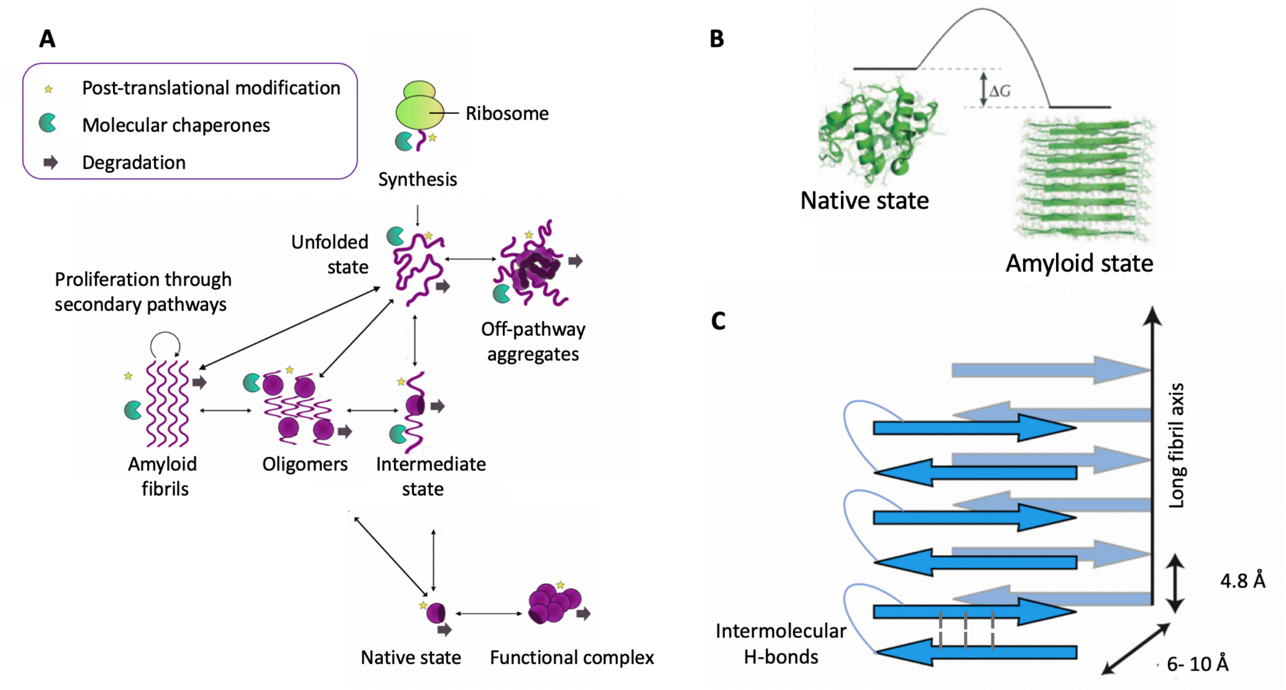

Figure 1. A protein can exist in various different states. A. After synthesis, unfolded proteins can follow different pathways. The initiating event in aggregation may be covalent modification of the disease protein, facilitating conversion of the protein to an abnormal conformation. Oligomeric (globular) intermediates may form, and then protofibrillar structures are assembled. Amyloid fibres can then form, possibly through association of protofibrillar intermediates, resulting in aggregates or inclusions. The intermediate species are hypothesised to be more toxic than either the precursor protein. Modified from (1). B. The relative thermodynamic stability of a protein's native and amyloid states is regulated by the free energy difference, ΔG, of the two forms. Free energy of the amyloid state depends on the protein concentration, whereas the free energy of the native state is usually independent of it. Although, at certain concentration, the amyloid state and the native state have the same stability. Indeed, at concentrations over that critical one, a protein is more stable in the amyloid state than in its native state, but the native state can still exist briefly if there are high free-energy barriers that prevent the transition into the amyloid state. Modified from (1). C. Model of parallel beta-strand arrangement in amyloid fibrils. Adapted from (6), intermolecular H-bonds, loop between beta sheets and measurements in Å were added.

Proteins characterised by complex or unstable conformation sometimes have difficulty achieving their native state. In these cases, the cell has several defence systems to help them to find their native functional conformation. For example, clearance mechanism and molecular chaperone should prevent aberrant protein aggregation. Disfunction of these cellular processes for control of protein homoeostasis can be trigger for protein misfolding diseases (7).

Once the aggregation process has taken place, the aggregated proteins are resistant to degradation and lack functionality. In addition, intermediate and end products of the aggregation process are acknowledged to be toxic to cells. Moreover, increasing evidence suggests that prefibril oligomer intermediates may be even more toxic than mature amyloid fibres (8). Protein misfolding, therefore, leads to depletion of cellular function, cell death, and reduction of functional tissue volume (3).

Protein aggregation diseases are not exclusively related to the central nervous system; they can also appear in peripheral tissues. In general, the genes and protein products involved in these kinds of diseases are called amyloidogenic. Such diseases include type 2 diabetes (T2D), inherited cataracts, some forms of atherosclerosis, haemodialysis-related disorders, and short-chain amyloidosis, among many others. All these diseases have in common the expression of a protein outside its normal context, leading to an irreversible change into a sticky conformation rich in beta sheets that makes the protein molecules interact with each other.

In summary, the propensity of a protein to undergo misfolding processes is determined by its thermodynamic stability, the free energy barriers associated with the transition, the rates of synthesis and degradation, the interaction with chaperones and the occurrence of PTM. Among these, glycation, an ageing-correlated PTM, is becoming increasingly implicated in the pathogenesis of misfolding diseases and it will be the further subject of investigation of this project.

1.2 Amyloid fibrils

A wide range of biophysical techniques have been employed to characterise the structure of amyloid fibrils formed from different types of proteins. Among these approaches, the most used have been X-ray fibre diffraction, X-ray crystallography of crystallised fragments, solid-state nuclear magnetic resonance (ssNMR), electron paramagnetic resonance (EPR), atomic force microscopy (AFM), electron-microscopy (EM), and recently also cryo-electron microscopy (cryo-EM) (4,9-14).

On the microscopic scale, amyloid fibres are typically manifested in the form of thread like fibrils, characterised by 5 to 15 nm in diameter and with a length ranging up to the μm scale. Some fibrils also display a regular twist around their long axis. The fibrils are characterised by a cross-beta structure firstly identified in 2004 by means of X-ray fibre diffraction (15). These beta strands are characterised by a specific pattern that is made up of single beta-strands that run perpendicular to the long fibril axis (4). These results were lately corroborated by means of Fourier transform infrared spectroscopy, solid-state nuclear magnetic resonance (ssNMR), and further X-ray crystallography (3,16,17). Another approach to follow the formation of amyloid fibrils is to use dyes that intercalate into the beta structures such as thioflavin-T (ThT), Congo red, or their derivatives (18,19).

The beta-strands found in the fibrils are stacked on top of each other with an inter-strand distance of 4.8 Å as shown by the first reflection in the X-ray fibre diffraction pattern. Mostly, two or more beta-strands are found per layer of the fibril and the distance between these strands ranges from 6 Å to 10 Å and this distance is recorded as a second reflection in the X-ray diffraction pattern (4). The beta-strands when stacked, are connected by inter-molecular hydrogen bonds that provide a surprising strength and stability to the amyloid fibrils (**Fig. 1 C**). In this pattern the consecutive beta-strands alternate directions so that the N-terminus of one strand is adjacent to the C-terminus of the next one. This distribution allows the inter-strand hydrogen bonds between carbonyls and amines to be planar, which is their preferred orientation. Furthermore, this arrangement produces the strongest inter-strand stability, further enhanced by the presence of multiple closely interacting sheets.

Side chains face either the inside of the fibril core to build an interface, also called steric-zipper, or they stick out and are in contact with the surrounding environment (9). A model showing a parallel arrangement of beta-strands within a fibril is shown in figure 1 C.

1.3 Formation of amyloid fibrils

Most of the amyloid fibrils are characterised by a repetitive and highly ordered structure undergoing a specific process of fibril growth. The aggregation process is promoted by conditions that destabilise the native fold of the protein, such as high temperature, high pressure, low pH, organic solvents, natural or post-translational mutations (20-22).

Their aggregation process is characterised by at minimum three microscopic steps: primary nucleation of monomers only, secondary nucleation of monomers on fibril surface, and elongation of fibrils by monomer addition.

According to the classical nucleation process, monomer-dependent secondary nucleation is defined as a process whereby nucleus formation from monomers is catalysed by aggregates composed of the same type of monomeric piece (**Fig. 2**). In this manner, the monomers form a nucleus on the surface of an already existing aggregate: secondary nucleation occurs in the presence of a parent seed aggregate of the same kind of monomers. In most cases, a nucleus is formed on the surface of an already existing aggregate, thus elongation process proceeds promptly. During elongation, monomers attach themselves to one end of the protofibrils.

It is crucial to identify whether or not the monomer concentration affects the process. If it does, a high concentration dependence of the lag time is possible, otherwise only a weak dependence can emerge because a change in the monomer concentration has no direct effect on the nucleation pathway (23).

Reason behind the occurrence of either primary or secondary nucleation is still under investigation. However, it is well known that certain proteins tend to preferentially follow one or the other mechanism. For example, monomer-dependant secondary nucleation has been inferred for several proteins including Abeta (23-26), IAPP (27), insulin (28), alpha-synuclein (29,30), and carbonic anhydrase (31).

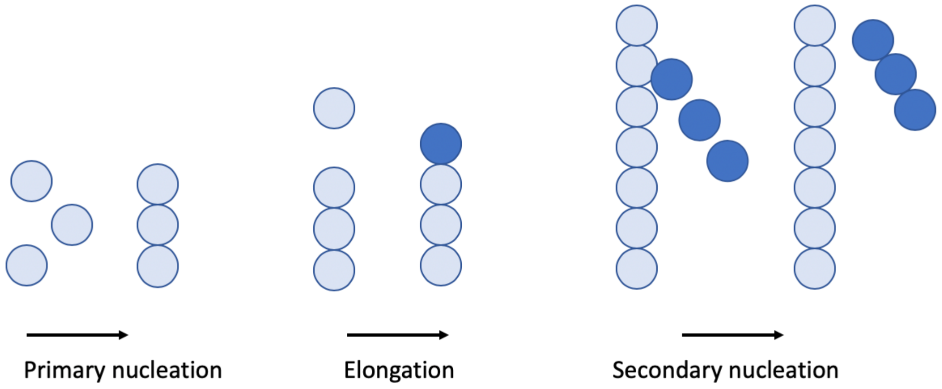

Figure 2. Mechanisms of fibrils formation. Primary nucleation involves monomers of one substance in solution. Elongation occurs by monomer addition to the ends of fibril, whereas secondary nucleation involves monomers of one substance on the surface of an already existing aggregate of the same substance. Light blue spheres symbolise monomers. Adapted from (20) or (21).

1.4 The kinetics of amyloid fibrils formation

The investigation of how different experimental conditions can influence the speed of protein aggregation is the focus of kinetics studies. To do so, it is crucial to follow the process leading to the formation of amyloid fibrils. One of the most common techniques takes advantage of the characteristic tinctorial property of amyloid structures, namely the ability to bind specific dyes such as Thioflavin T (ThT). Since the first description in 1959, ThT has become one of the most widely used fluorescent dyes for the staining of amyloid fibrils both *in vivo* and *in vitro* (32). When ThT binds to beta sheet-rich structures, a distinctive feature of amyloid aggregates, its fluorescence gets enhanced, leading to a characteristic red shift of its emission spectrum (6).

Generally, when aggregation prone proteins are incubated *in vitro* with the ThT dye, the kinetic pattern of the spontaneous formation of amyloid fibrils, recorded as the variation in fluorescence, during the time, is shown as a sigmoidal curve. The curve is typically characterised by three main components: the lag phase, the growth phase, and the plateau phase (**Fig. 3)**.

The nucleation step, which happens in the lag phase, is characterised by monomers that undergo conformational changes and associate with each other. These monomers generate an oligomeric nucleus, characterised by the presence of beta structures. The transition to elongation depends on the amount of accumulated oligomeric nuclei, which act as seeds for protofibril formation. During the elongation phase, the nuclei rapidly grow by further association of monomers and form larger fibrils until saturation.

As mentioned, the nucleation phase is thermodynamically unfavourable and occurs gradually, whereas the elongation phase is a much more favourable process and proceeds quickly. The limiting step in the process is the formation of nuclei/seeds to promote aggregation. Thus, amyloid formation can be substantially accelerated by the addition of preformed seeds (nuclei). The addition of seeds lowers the lag time and induces faster aggregate formation.

The presence of seeds is not the only factor that affects the aggregation kinetics. Post-translational modifications, which can strongly influence the proteins subcellular localisation, activity, protein-protein interaction, and their stability also plays a crucial role in protein aggregation (33). Post-translational modifications are modification of proteins, occurring after protein biosynthesis, such as phosphorylation, arginine methylation, acetylation. Most of them involve an enzymatic reaction and produce a covalent bond. However, post-translational modifications can naturally occur without the help of an enzyme. Among these, glycation has come to the light as a possible factor affecting the aggregation pathway and, therefore, it will be the subject of this project.

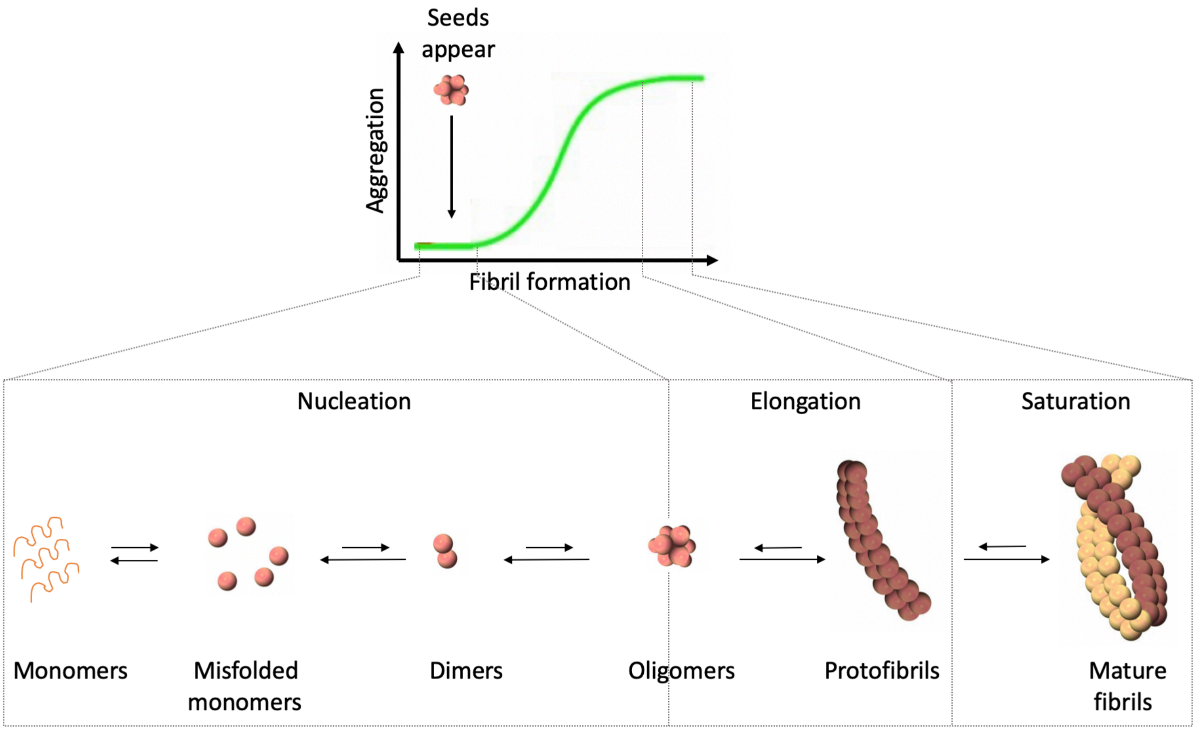

Figure 3. Steps of amyloid fibrils formation. The kinetics of amyloid fibrils formation is represented by a sigmoidal curve, corresponding to consecutive steps of nucleation, elongation, and saturation. During nucleation, misfolded monomers associate with each other. They generate an oligomeric nucleus, characterised by the presence of beta structures. The transition to the elongation depends on the amount of accumulated oligomeric nuclei, which performs as seeds for protofibril formation. During saturation, mature fibrils are produced from protofibrils. Figure adapted from (34).

1.5 Glycation

Glycation is the result of a covalent bonding of a protein with a glycating agent, such a sugar molecule, without controlling action of an enzyme, as opposed to protein glycosylation that is characterised by an enzymatic reaction.

Protein glycation occurs through the Maillard reaction of a protein amino group with glucose to yield a Schiff base, which undergoes a rearrangement to form a so called Amadori compound (**Fig. 4 A**) (34). Subsequently, this compound is subject to decomposition, fragmentation and condensation, to yield advanced glycation end-products (AGEs). Glucose, Schiff base and Amadori compound can also exhibit auto-oxidation reactions that are responsible for the formation of oxygen free radicals and production of highly reactive carbonyl compounds. AGEs can affect protein structure and function in nearly every type of cell in the body, in particular, they are believed to play the causative role in the vascular complications of type-2 diabetes (T2D). Under certain pathological conditions, such as oxidative stress due to hyperglycaemia in diabetic patients, AGE formation can increase beyond normal levels.

In biological systems, glycation can occur with the N-terminal of proteins and peptides and the side chain of amino acids such as lysine, arginine, cysteine and histidine (35). The reaction is not available to non-reducing sugars, such as sucrose, where the aldehyde or ketone groups have been converted to a glycosidic bond. In addition to glucose, glycation can be initiated by other carbonyl-containing compounds, such as methylglyoxal (MGO) and oxidized lipids (36). In particular, glucose is relatively unreactive compared to MGO, a short, open-chained dicarbonyl compound. MGO, a metabolite of glucose, primarily reacts with arginine or lysine residues and is estimated to be 20,000-50,000 times more reactive than glucose (**Fig. 4 B**) (37-39). Since it is such a powerful glycating agent, the accumulation of the cell-permeant MGO can be extremely harmful. The glycation reaction involves first the production of a reversible Schiff base which can slowly rearrange to give rise to the stable Amadori compound product (**Fig. 4 A**). Subsequently, these species can undergo further rearrangement and eventually various chemical reactions, resulting in the formation of advanced glycation end-products (AGEs), of which there are over 300 variants (40).

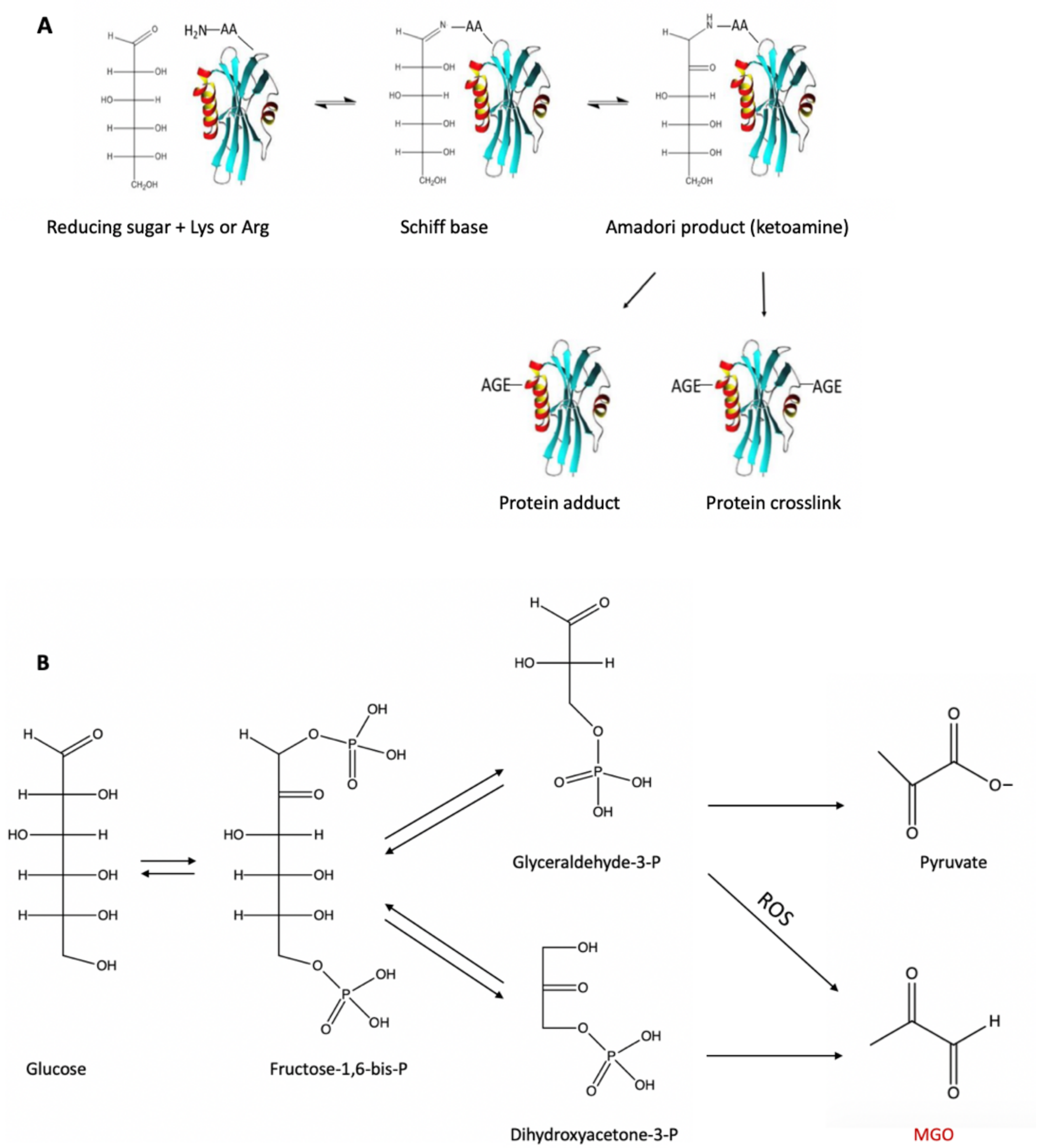

Figure 4. A. Schematic presentation of the Maillard reaction. Reactive carbonyl groups of a reducing sugar react with neutrophilic free amino groups of proteins to form a reversible Schiff base. Through rearrangement a more stable Amadori product is formed. B.Fischer projections of the simplified glycolysis process, the metabolic pathway converting glucose into pyruvate. This pathway involves the intermediate metabolite fructose-1,6-bisphophate (fructose-1,6.bis-P) that can be converted into two trioses: glyceraldehyde-3-phospate (glyceraldehyde-3-P) and dihydroxyacetone-3-phospate (dihydroxyacetone-3-P). MGO is formed from glyceraldehyde-3-P and dihydroxyacetone-3-P th

at accumulate when glyceraldehyde-3-phosphate dehydrogenase activity is inhibited by hydrogen peroxide (41,42). Modified from (43).

1.6 Advanced glycation end-products

In the last years, advanced glycation end products (AGEs) have received particular attention in the context of aging. AGEs can be obtained from the diet or can be formed endogenously. High-heat and dry-cooking methods produce a very large amounts of AGEs in food, whereas raw food, boiled, or simmered tend to be lower in AGEs (44). Fatty foods such as butter or oil have the highest amounts of AGEs per gram, even prior to heating, followed by cooked meats (45,46).

AGE endogenous formation is typically a slow process that occurs on long-lived extracellular proteins (40). However, MGO-modified peptides can rapidly generate AGEs. MGO-induced glycation of arginine residues forms argpyrimidine (ArgP) and hydroimidazolone, while the lysine-derived AGEs are Nε-carboxymethyl-lysine (CML) and Nε(1-carboxyethyl) lysine (CEL). (**Fig. 5**) (38,40,47-49). The methylglyoxal-derived hydroimidazolone is one of the most quantitatively and functionally important AGEs in physiological systems, as early indicator of atherosclerotic process in diabetes (50). Interestingly, increased levels of circulating CML was able to predict hospitalisation and it was independently associated with a higher risk of mortality in a large cohort of heart failure patients (51).

High concentrations of AGEs may induce toxicity via aberrant cross-linking with proteins, binding to cell-surface receptor RAGE (receptor for AGEs) and production of oxygen free radicals (52). RAGE stimulation can inhibit and induce cytoprotective and cytotoxic signalling pathways, respectively, and is becoming increasingly implicated in the pathogenesis of misfolding diseases (53,54).

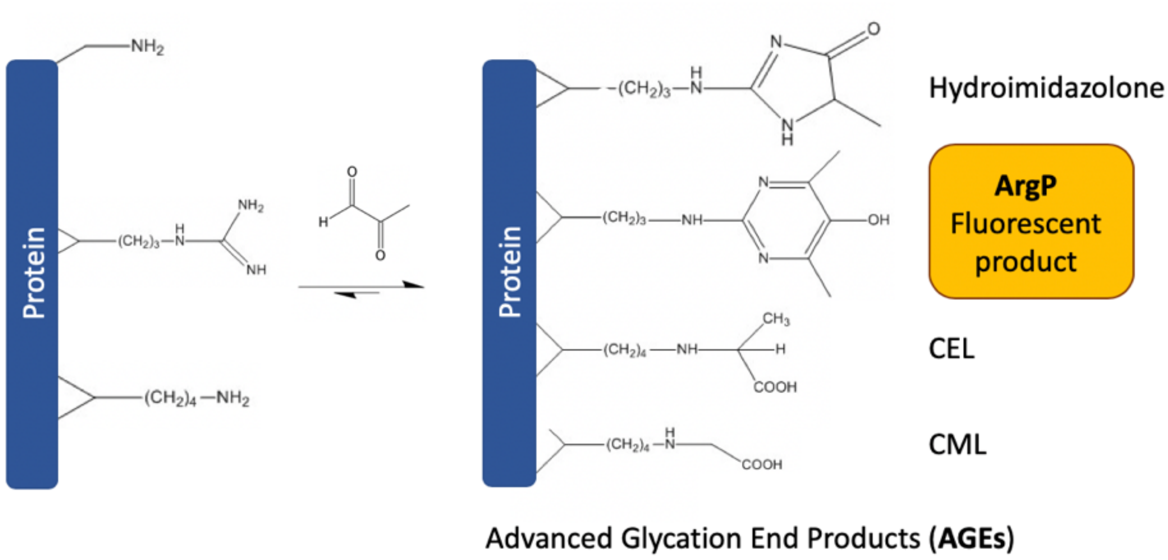

Figure 5. MGO-induced glycation reaction. Glycation involves MGO with primary or secondary amine groups on protein residues (N-terminus, Arg, Lys) producing advanced glycation end-products (AGEs) such as hydroimidazolone, the fluorescent argpyrimidine product (ArgP), carboxyethyl-lysine (CEL), carboxymethyl-lysine (CML) etc.

1.7 AGEs and their association with neurodegenerative diseases and diabetes

The formation of AGEs promotes the deposition of proteins leading to the abnormal accumulation of the modified proteins. Numerous proteins involved in neurodegenerative diseases such as Abeta, tau, alpha-synuclein, and prions are glycated, and the extent of glycation is correlated with the pathologies, suggesting that AGEs encourage the development of neurodegenerative diseases (55,56). Southern et al (57) analysed brain sections from 25 AD patients with varying degrees of cognitive dysfunction and cerebrovascular pathologies and found that impaired cognition was correlated with higher content of AGEs such as carboxymethyl-lysine in the vasculature and the cortical neurons. The amount of AGEs measured was also proportional to the severity of diabetes. Moreover, Valente et al (58) demonstrated that the brains of people affected by both AD and diabetes have higher amounts of AGEs' deposits and upregulation of RAGE compared to non-diabetic patients affected just by AD. Patients with both diseases had a greater presence of dense plaques. The large presence of AGEs in the neurofibrillary pathology of AD heavily supports that AGEs have a crucial role in the neuropathogenesis of AD (47,56). Due to their implication in the progression of neurodegenerative and diabetic diseases, AGEs represent a hotspot and could give more information about the aetiology of both diseases.

1.8 Glycation and protein misfolding

Glycation is well known to play a significant role in modifying protein structure and functions, as reported for a broad range of folded proteins (59). Moreover, it is expected to have a drastic effect on the biological function and biophysical properties of intrinsically unfolded polypeptides (59), although much less is currently known on this topic. Two of such examples are the aggregation-prone peptides amyloid-beta peptide (Abeta) and islet amyloid polypeptide (IAPP). IAPP is a peptide associated with glycation in T2D patients (60). It is generally accepted that aggregation of IAPP in T2D causes loss of insulin-producing pancreatic beta-cells (61). The associated hyperglycaemia increases the occurrence of glycation (62): Ma et al. (60) showed that the extracted IAPP displayed glycation by *in situ* investigations in human pancreatic deposits. Moreover, Abeta, associated with AD, is also subject to glycation and amyloid fibrils have been found to be glycated in patients affected by this disease (63). This evidence again suggests a central role of glycation in both diabetic complications and neurodegenerative processes such as AD. For this reason, it is crucial to investigate if glycation affects molecular events responsible for protein aggregation and self-assembly of proteins involved in AD and in T2D, such as Abeta and IAPP respectively.

1.9 Abeta

One of the main hallmarks of AD is the deposition of amyloid plaques and neurofibrillar tangles in the brain (64-67). The major component of the amyloid plaques is a peptide called amyloid beta peptide (Aβ or Abeta), which was first identified by Glenner and Wong in 1984 (68,69). On the other hand, neurofibrillary tangles mainly consist of aggregated tau protein, a protein involved in the stabilisation of microtubules (70). Abeta denotes peptides of 36–43 amino acids, and the two most common forms are Abeta40 and Abeta42 that have a molecular mass of about 4.3 and 4.5 kDa, respectively. Abeta is a product generated through a sequential cleavage of the amyloid precursor protein (APP). APP is a glycoprotein, expressed in several tissues, especially in the synapses of neurons and its role has been described as crucial in AD pathogenesis (65,67). It is a membrane protein with one transmembrane helix where the C-terminus is intracellular and the Abeta domain is localised both in the membrane and extracellularly. APP covers a regulatory role in synaptic formation and repair (71), anterograde neuronal transport (72) and iron export (73). This membrane protein is produced as several different isoforms, ranging in size from 695 to 770 amino acids. The sequential proteolytic process of APP can follow a non-amyloidogenic and an amyloidogenic pathway, through the enzymes α, β and γ-secretase (**Fig. 6A**) (64,65,67).

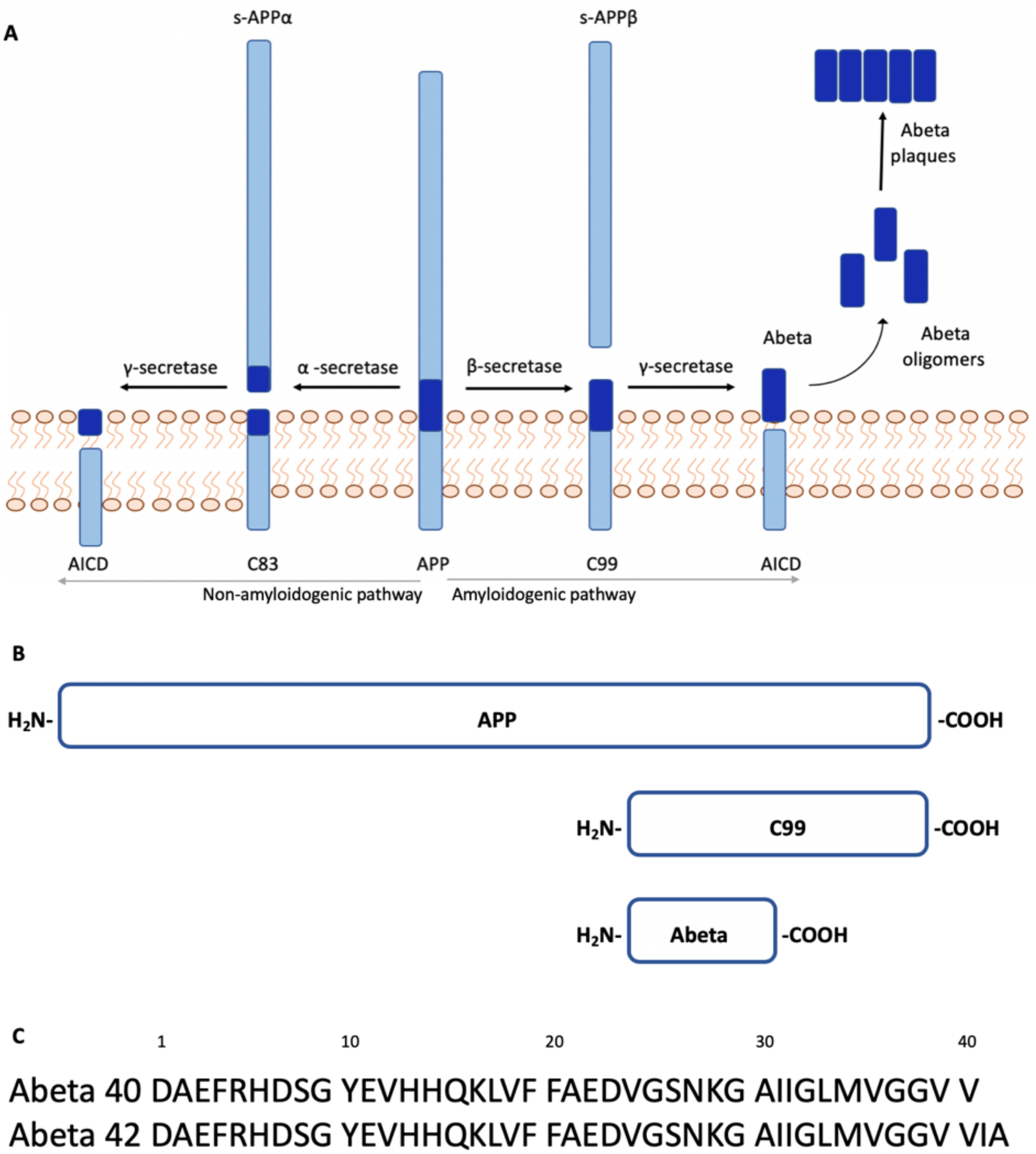

Figure 6. Amyloidogenic and non-amyloidogenic pathways of APP, the Abeta precursor protein. A. APP undergoes a sequential proteolytic cleavage by α- and γ-secretase via a non-amyloidogenic pathway. The α-secretase produces sAPPα extracellularly and C83 embedded in the membrane. C83 can be further cleaved by γ-secretase producing P3 and AICD, which are not toxic. The amyloidogenic pathway, which generates Abeta, is initiated by β-secretase cleavage producing the secreted sAPPβ extracellularly and the C99 embedded in the membrane. C99 can be subsequentially cleaved by γ-secretase, producing Abeta extracellularly and AICD intracellularly. Adapted from (69). B. Schematic structure of APP, C99 and Abeta. C. Primary structure of Abeta40 and Abeta42.

In the non-amyloidogenic pathway, APP undergoes serial proteolytic cleavages by α- and γ-secretase, precluding Abeta generation. This pathway is initiated by α-secretase, that acts on the extracellular membrane side and releases the extracellular fragments, called s-APPα The resulting C-terminal fragment C83 ($APP_{688-770}$), which is still embedded in the membrane, can be further cleaved by the γ-secretase, releasing a non-amyloidogenic fragment P3 and the APP intracellular C-terminal domain (AICD) (**Fig. 6 A, B**).

In contrast, the amyloidogenic pathway is mediated by the β and γ-secretase, leading to extracellular release of amyloidogenic Abeta. B-secretase cleavage produces the secreted s-APPβ, and the C-terminal fragment, C99 ($APP_{672-770}$). C99 can be cleaved by γ-secretase, producing extracellular Abeta and intracellular AICD (64,65,67). The cleavage by γ-secretase can occur on several sites between residues 38-42 (64). This process produces mainly Abeta(1-40) and Abeta(1-42) (from now on called Abeta40 and Abeta42) and their ratio is believed to play a crucial role in the rate of amyloid formation (64). Despite Abeta40 and Abeta42 differ for just two amino acids (isoleucine and alanine), they act differently: Abeta42 is more prevalent in amyloid plaques and it is the more fibrillogenic of the two (66,74). The sequences of Abeta40 and Abeta42 are shown in figure 6 C.

1.9.1 Abeta secondary structure

Abeta is an aggregation-prone peptide, that varies its structural state at different stages in the aggregation process. Abeta may adopt different secondary structures including random coil-like, beta-structured and alpha-helical states depending on the environmental conditions (75).

Before the γ-secretase cleavage, Abeta is part of the transmembrane domain of C99, which is characterised by two helical domains. A short extracellular N-helix ($APP_{688-694}$) is connected by an N-loop ($APP_{695-699}$) to the helical transmembrane domain (TMD or $APP_{700-723}$) (76). The N-helix is embedded in the membrane surface and will be part of cleaved Abeta peptides combined with the helical TMD (77) (**Fig. 7**). Thus, Abeta exhibits an alpha-helical structure in a membrane environment. This secondary structure was described firstly in 1994 using NMR spectroscopy on the fragment Abeta (1-28). Once Abeta was dissolved in solution and abandoned the membrane-like environment, a transition from alpha-helix to beta-sheet conformation was described (78). The presence of alpha-helix structure was lately confirmed using the entire full-length peptide: in the presence of sodium dodecyl sulphate (SDS) micelles, Abeta formed two alpha-helices involving residues $\text{Abeta}_{15\text{–}24}$ and $\text{Abeta}_{29\text{–}35}$ corresponding to the N-helix and the helical TMD belonging to the C99 fragment of APP (79,80) (**Fig. 7**).

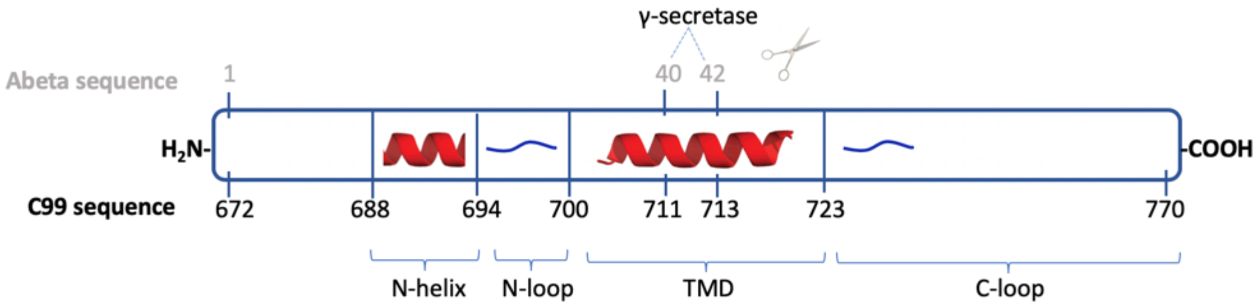

Figure 7. Schematic representation of C99 tertiary structure. C99 is the peptide resulting from the cleavage of APP by γ-secretase. In C99 two helical domains are identified: a short extracellular N-helix (APP688-694) and a helical transmembrane domain (TMD or APP700-723). They are connected by an N-loop (APP695- 699) (71). When C99 undergoes γ-secretase cleavage, Abeta is released, whose number sequence is in grey above.

However, Abeta is classified as an intrinsically disordered protein (IDP) i.e. under physiological conditions, the peptide lacks a stable tertiary structure (81,82). For this reason, it cannot be crystallised by common methods, but NMR, CD and molecular dynamics are suitable techniques to carry out structural investigation on its secondary structure. Thus, NMR and CD spectroscopy were used to elucidate how Abeta monomers are predominantly unstructured (83,84). Despite the typical IDP properties, NMR studies showed that Abeta could exhibit alpha-helix or beta-sheet conformation dependant on the environment conditions.

In 1998 and 2000, two studies were carried out incubating Abeta peptide in the presence of SDS micelles to mimic the membrane-like environment and in hydrophilic conditions, respectively. In the presence of SDS micelles, Abeta40 exhibited alpha-helix conformation at the C-terminus ($\text{Abeta}_{15\text{-}36}$) with a kink or hinge at around amino acids 25-27. While the N-terminus of the peptide ($\text{Abeta}_{1\text{-}14}$), whose residues are mainly polar and likely solvated by water, was unstructured. The deprotonation of two acidic residues in the helix promoted a helix-to-coil conformational transition that preceded the aggregation of Abeta40 (85). Whereas, in aqueous environment, Abeta collapsed into a compact series of loops and strands and did not exhibit any alpha-helical or beta-sheet structure. Almost one fourth of the surface was continuously hydrophobic and the compact random coil structure would lead to a general conformational rearrangement with the formation of an intermolecular beta-sheet secondary structure generated by fibrillisation (86).

The presence of helical structure in a lipidic environment was further confirmed in 2002 and 2004 by means of NMR spectroscopy. Two distinct helical regions in Abeta core were described, by analysing 3D NMR structures of the Abeta peptide (8-25) and Abeta peptide (28-38). In addition, the Abeta peptide (25-35), which is a very toxic derivative, behaved as a typical transmembrane helix in a membrane-like environment, leading to fibrillar aggregates. These results suggested a direct link between structure and neurotoxicity (87,88).

In the late 2000, different conformational states of Abeta40 and Abeta42 were described by means of molecular dynamics and NMR spectroscopic studies. NMR-guided simulations showed that the C-terminus of Abeta42 was more structured than previously assumed and that residues 31-34 and 38-41 formed a protein structural motif called beta-hairpin. This particular structure consists of two strands that were adjacent in the peptide's primary structure where the N-terminus of one sheet lied on the C-terminus of the other. In this study, the beta-hairpin reduced the C-terminal flexibility, a factor that could be responsible for the more fibrillogenic behaviour of Abeta42 than Abeta40 (89). Moreover, molecular dynamics studies suggested that Abeta40 and Abeta42 were characterised by the rapid transition between alpha-helix and beta-sheet conformers (89). However, in 2011, a NMR study indicated that Abeta40 displayed a significant secondary and tertiary structure in aqueous environment (90). This outcome was the foundation for further studies showing that the hydrophobic C-terminal of Abeta played a crucial role in the transition from alpha-helical to beta-sheet structure (91).

1.9.2 Abeta secondary structure organisation

Abeta undergoes an aggregation process leading to the formation of long and mature amyloid fibrils characterised by a high content of secondary beta-sheet structures. Using X-ray diffraction, Abeta fibrils show a highly regular cross-beta diffraction pattern, characterised by an intersheet distance of 4.8 and 10 Å along and perpendicular to the fibril axis, respectively, which is characteristic of amyloid aggregates. Numerous structural biology techniques have been employed to investigate the structure of amyloid fibrils (92-102).

Scanning transmission electron microscope (STEM), EM and ssNMR, suggested that the supramolecular structures of fibrils derived from Abeta40, Abeta42 and from the peptide

Abeta(10-35) were organised as beta-sheets (92,93). Several ssNMR methods revealed that amyloid fibril cross-beta structures exist in two patterns: parallel and antiparallel depending on the direction of the peptide strands (**Fig. 8**) (94-96). Parallel structures are more stable due to the fact that they have more ordered residues, longer beta strand segments and more ordered packing of hydrophobic side chains (97). Antiparallel fibrils are thermodynamically metastable i.e they are in an equilibrium state, which does not correspond to an absolute minimum of energy.

When the beta strands are in parallel, they can be in-register with aligned residues or out-of-register with non-aligned residues (**Fig. 8**).

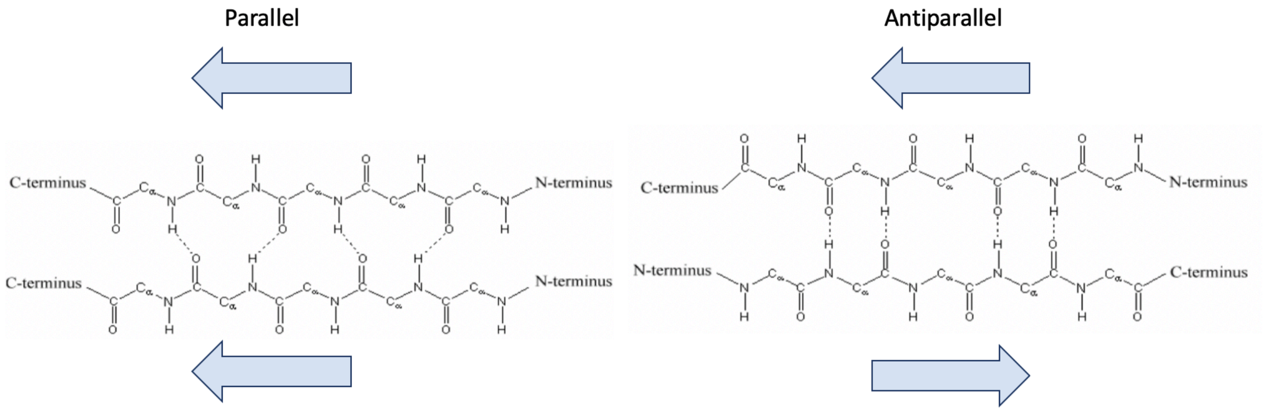

Figure 8. Hydrogen bond pattern in the parallel and anti-parallel arrangements of the beta strands in beta-sheets. Beta strands can be in the parallel and anti-parallel arrangements and they are characterised by a specific hydrogen bond pattern. Beta sheets are parallel if the polypeptide strands run in the same direction, N-terminus to C-terminus, indicated by the blue arrows. The N-terminus of one beta strand is opposite the N-terminus of the other beta strand. The hydrogen bonds are not perpendicular to the individual strands. Anti-parallel beta-sheet arrangement occurs when a polypeptide chain sharply reverses direction. This can occur in the presence of two consecutive proline residues, which create an angled kink in the polypeptide chain and bend it back upon itself. The hydrogen bonds pattern is perpendicular to the individual strands.

Multiple quantum ^{13}C NMR data indicated that beta strands were arranged in parallel, in particular in parallel an in-register, parallel organisation in Abeta peptide (94). In addition, the cross-beta structure pattern was confirmed on both Abeta40 and Abeta42 by means of various ssNMR studies (16,94-96,99,103) (**Fig. 9**). Among these studies, a parallel alignment of the beta-sheets was described in both Abeta variants (94-96) (**Fig. 9 A**). However, when Abeta was subject to a single substitution described by Iowa et al. (D23N-Abeta), which is associated with early onset familial AD, showed both parallel and anti-parallel patterns suggesting a correlation between beta-sheet alignment and certain AD onset (97,101) (**Fig. 9 B**). The anti-parallel alignment in Abeta resulting from the Iowa variant is thermodynamically less favourable compared to parallel arrangement (97). Nonetheless, the anti-parallel form appeared to be more common when Iowa-mutant Abeta aggregates without additional seeding, pointing out the higher propensity for spontaneous nucleation of this mutated Abeta (97).

It is remarkable that Abeta can exhibit both parallel and anti-parallel arrangements in different conditions. Tycko's research group presented several works about this compelling subject. They compared Abeta fibrils formed from parallel and antiparallel beta sheets demonstrating that antiparallel sheets nucleated faster and were metastable with respect to parallel structure conversion. Both types of fibrils were demonstrated to be equally neurotoxic (97).

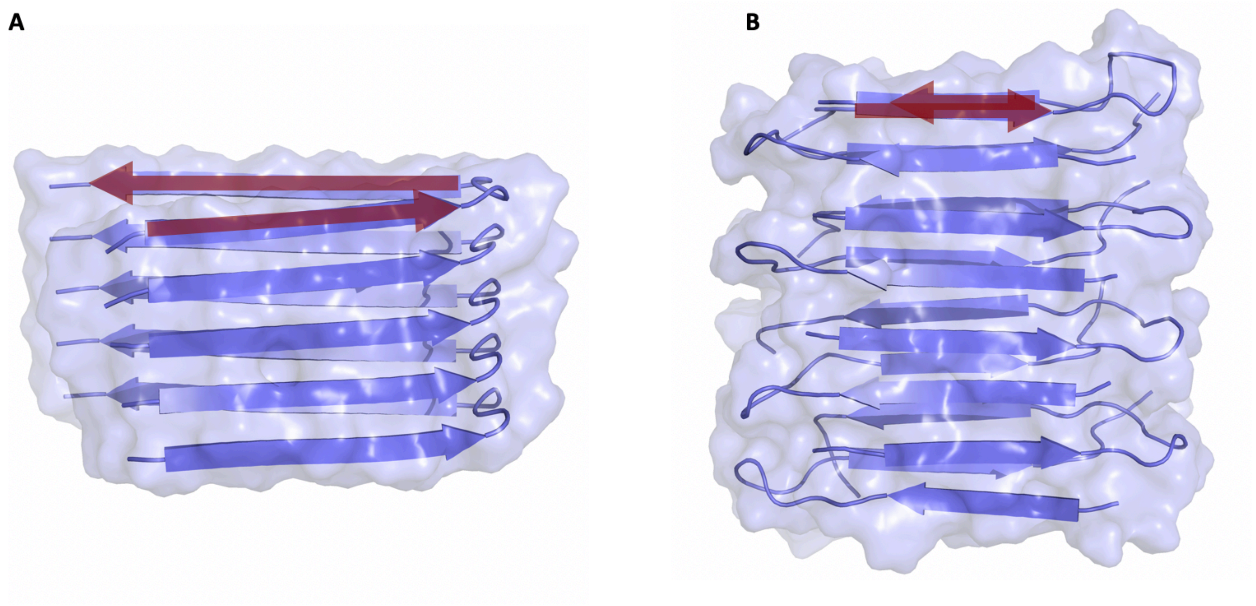

Figure 9. Structural states of Abeta in fibrils showing a parallel or antiparallel pattern. A. Abeta42 fibrils contain two parallel beta sheets in residues 18–26 and 31–42 (protein data bank - PDB code 2BEG) (90). B. Abeta40 with the Iowa variant D23N exhibits an anti-parallel alignment (PDB code 2LNQ) (92). Red arrows indicate the repeating unit of protein for each beta sheet structure.

1.10 IAPP

The primary pathology in T2D is hyperglycaemia, i.e. high blood glucose, caused by a combination of insulin resistance and pancreatic beta-cell loss, leading to a lack of insulin production (104). One major accepted cause of pancreatic beta-cell death is the aggregation of IAPP, a small peptide hormone co-produced and co-secreted along with insulin from the endocrine beta-cells of the pancreas (105). IAPP is the primary constituent of amyloid deposits in the pancreatic islets. The extent of beta-cell loss is correlated with extracellular accumulation of IAPP aggregates and over 90% of T2D patients have pancreatic islet IAPP aggregates (104,106,107).

IAPP, also called amylin, is derived from an 89 residue pre-pro-hormone. After cleavage of the signal sequence, it results in the 67-residue pro-form, which is processed in the Golgi and in the insulin beta-cell secretory granule to yield the mature hormone. The mature 37-residue peptide requires further processing and post-translational modifications such as amidation of the C-terminus and the formation of an intramolecular disulphide bridge between Cys2 and Cys7.

Despite the cytotoxicity of the non-amidated variant, the lack of amide group on the C-terminus may initiate different aggregation processes by affecting the hydrophobic structures, conformations, and intra-sheet interactions of the peptides (108). It was extensively demonstrated that both features resulting from post-translational modifications, C-terminus amidation and disulphide bridge, are necessary for full biological activity (109,110). For this reason, obtaining the IAPP C-terminal amidation is extremely relevant, as suggested by Cottingham et al. who presented a suitable protocol to produce C-terminal amidated IAPP expressed as a fusion protein (111).

At physiological pH, IAPP is slightly positively charged, thanks to residues Lys1, Arg11, and His18. Despite the charged residues, IAPP is also characterised by hydrophobic features because of 16 residues carrying hydrophobic side chains. The sequence of mature IAPP is shown in figure 10.

Figure 10. Primary structure of human IAPP. The sequence of mature human IAPP with oxidised intramolecular disulfide bridge and amidate C-terminus.

As an intrinsically disordered peptide, IAPP does not adopt a compact globular structure in its physiological soluble form. This was demonstrated by means of solution NMR studying the interactions between amylin and membranes. Patil et al. elucidated IAPP behaviour in several environments such as water, ranging pH from 4.3 to 7.3 and using different SDS micelles concentrations (112,113) (**Fig. 11 A**). IAPP is stored in secretory granules at pH 5.5 (114), an environment that favours the protonated state of His18 and contributes to stabilise the soluble monomer, due to electrostatic repulsion (115). In addition, co-storing of IAPP and insulin in the granules stabilises the soluble form of IAPP.

IAPP is widely regarded as a natively unstructured protein (116,117), however, it is highly prone to aggregation and formation of insoluble cytotoxic amyloid aggregates and fibrils (61). In patients affected by T2D, IAPP undergoes conformational changes to form highly-ordered beta sheets organised into amyloid fibres. Amyloid plaques are formed by masses of fibrils, but growing evidence suggests that the toxic species may be prefibrillar intermediates (2,116).

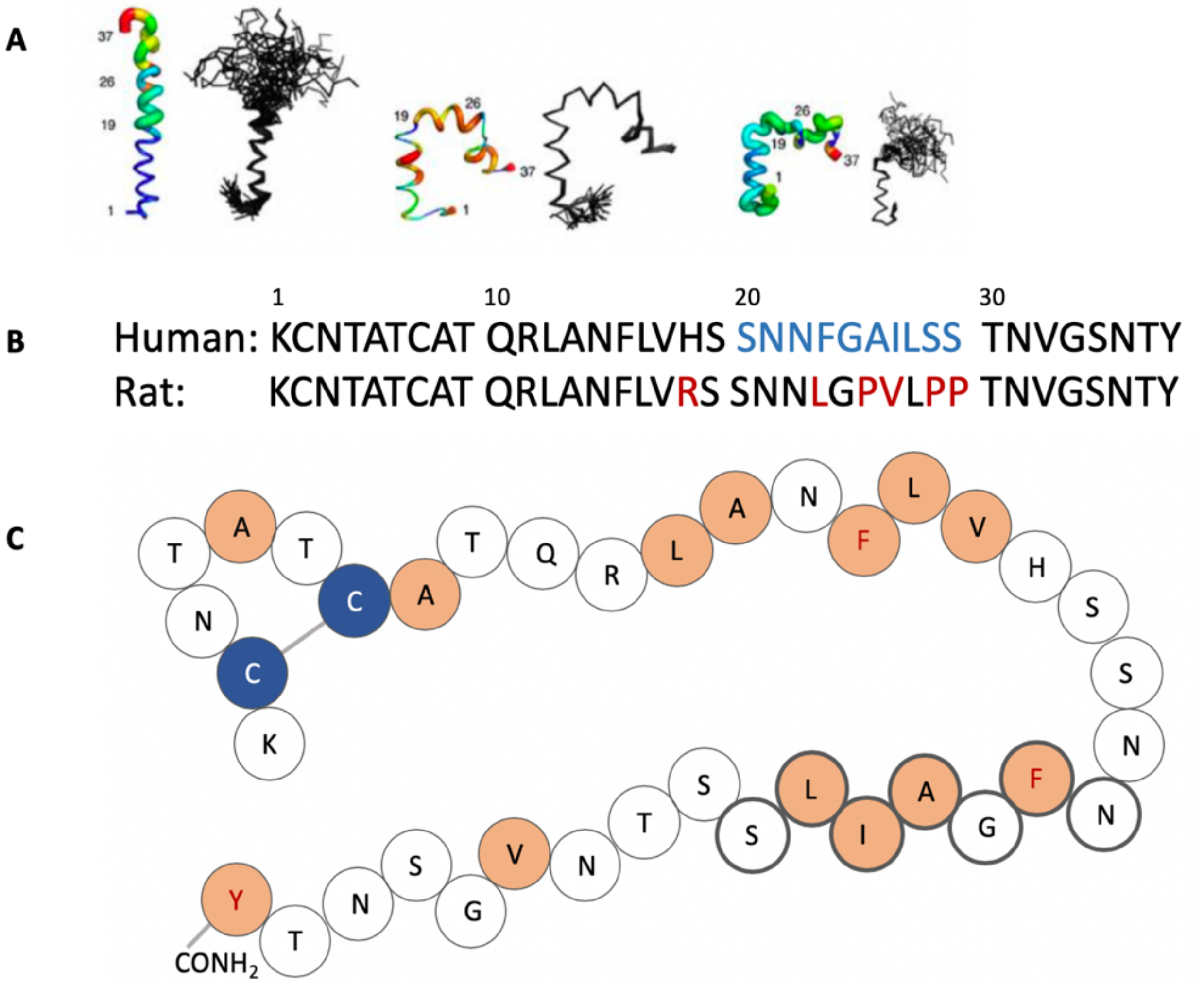

Figure 11. IAPP structure. A. Structures of human IAPP. (left) Monomeric IAPP in 100mM SDS micelles, pH 4.3 (PDB: 2KB8), (middle) 200mM SDS micelles pH 7.3 (PDB: 2L86) and (right) water (PDB: 5MGQ). Adapted from (109). B. Primary structure of human and rat IAPP. Residues belonging to the region considered the most amyloidogenic in human IAPP are in blue. Residues in red correspond to sequential differences in the primary sequences. C. Schematic diagram of the primary sequence of hIAPP. Blue circles indicate the cysteine amino acid C2-C7 disulphide bond. Orange circles indicate hydrophobic regions, with the aromatic residues (Phe15, Phe23 and Tyr37) in red. Bolt-circled represent some amino acids implicated in IAPP amyloidogenicity. Modified from (110).

1.10.1 IAPP amyloidogenicity and its aggregation structure

There is much interest in understanding the mechanism by which these proteins form fibrils and identifying intermediates in the aggregation pathway. However, obtaining structural information about intermediate species is difficult due to their transient nature. For this reason, slowing down the aggregation process could be a successful approach to understand the dynamics of aggregation and glycation of IAPP.

The variant frequently employed to study the self-assembly process of IAPP is the rat one (rIAPP), due to its lower tendency to aggregate. The sequence of rIAPP differs from the human IAPP particularly in the region of amino acids 25-29 (IAPP$_{25\text{-}29}$) (**Fig. 11 B**), which is important for amyloid fibril formation. The main difference in three proline residues at 25, 28, and 29 positions: human IAPP mutated to contain these three proline residues aggregates to a lesser extent (118).

Proline imposes a restriction on backbone conformational freedom and is known to be a beta-sheet breaker. The aggregation properties of segment 20-29 (IAPP$_{20\text{-}29}$) have been subject of study as it was first believed to be the only segment of human IAPP responsible for amyloid formation.

Studies probing the minimum number of residues required for amyloidogenicity of region IAPP$_{20\text{-}29}$ elucidated Phe23 as an important residue: fragment IAPP(24-27) lacked amyloidogenicity and cytotoxicity whereas fragment IAPP(23-27) aggregated at the fastest rate of all fragments and maintained cytotoxicity (119). However, other substitutions and/or chemical additions can inhibit or induce aggregation of the same fragment, and substitutions outside of the major amyloidogenic region can also influence aggregation propensity (**Fig**. **11 C**) (120-124).

Upon the unquestionable crucial role of region 20-29, subsequent investigations identified other segments as amyloidogenic in human IAPP. In particular, segments IAPP(8-20), IAPP(30-37) and also the N-terminus IAPP(1-8) are able to form fibrils (125-127).

1.10.2 IAPP’s amyloid fibril structure models

Different biophysical approaches were employed to elucidate the IAPP fibrils structure and the obtained insights were combined to build several structural models. Figure 12 shows the beta-strand regions as defined in the studies mentioned on the right.

Figure 12. Location of beta-strands in IAPP fibrils as found in different studies. The arrows show the beta-strand regions. From the top, first represents the serpentine model, obtained from EM studies (128), the solid-state NMR model (122), the model based on crystallised segments (123), d) the EPR model with staggering about 3 fibril layers (124), and e) the model derived from 1H solvent protection (125).

In 2004, X-ray and electron diffraction studies demonstrated the cross-beta diffraction pattern (15). The same year, electron paramagnetic resonance (EPR) was employed to describe an in-register-parallel arrangement of beta-strands in the fibrils (128). These outcomes and prior evidence from electron microscopy (129) were combined in 2005 to generate a serpentine model (130). The authors proposed a beta-serpentine fold composed of three beta-strands, separated by two turns. In particular, segment $\text{IAPP}_{22\text{-}27}$ was responsible of forming a beta-strand in this model.

The most detailed structural models of IAPP fibrils come from solid-state NMR (ssNMR). A highly cited structural model based on a ssNMR study was published in 2007 (131). It corroborated the in-register-parallel arrangement by distance constraints gained from dipolar re-coupling experiments and it shared the steric-zipper motif, where the side chains of the beta strands are firmly interdigitated, another common structural motif of amyloid fibrils (132).

In addition, inter-strand side-chain contacts of residues from opposing beta-strands were illustrated. In this model, two beta-strands per monomer were described, located at positions $\text{IAPP}_{8\text{-}17}$ and $\text{IAPP}_{28\text{-}37}$ and separated by a non-constrained loop. A symmetric dimer model was proposed, with a C2 symmetry about the long fibril axis. The inner beta sheets were composed of segments $IAPP_{28-37}$ and the outer sheets of segments $IAPP_{8-17}$. The N-terminus was not constrained in this model (131) (**Fig. 13**).

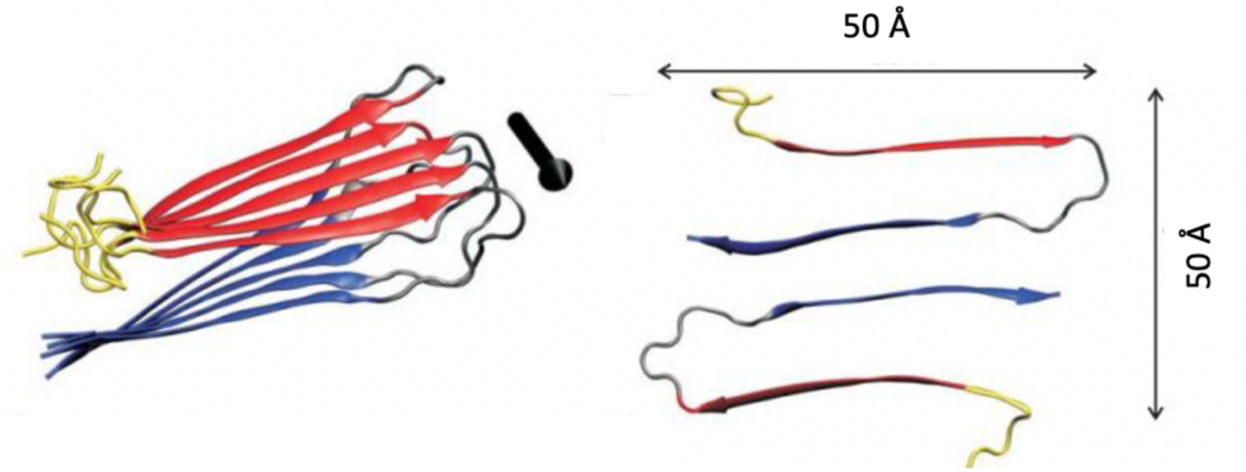

Figure 13. Molecular structural models for the protofilament in IAPP fibrils. Proposed by Luca et al. (122). Left. Ribbon representation of one cross-beta molecular layer, with N-terminal and C-terminal beta-strand segments in red and in blue, respectively. The black arrow indicates the fibril axis. Right. Cross-sectional view of two IAPP molecules in the protofilament, characterised by a configuration, with approximate C2 symmetry about the fibril axis. Modified from (131).

In 2008, straight after the model proposed by ssNMR, X-ray crystallography yielded a similar model (133) which, however, differed in the details of the packing of side chains. In this study, segments 21NNFGAIL27 and 28SSTNVG33 were crystallised. The model also described two beta-strands per monomer located at positions $IAPP_{8-17}$ and $IAPP_{24-37}$, and also confirmed a symmetric dimer as subunit, with a C2 symmetry about the long fibril axis. The outer beta sheets were composed of segments $IAPP_{24-37}$ (instead of $IAPP_{28-37}$ as suggested by the ssNMR) which built the dry steric-zipper interface in between two symmetric monomers in one fibril layer (133).

The fourth structural model, presented in 2012, was based on EPR studies and it was based on previous work from 2004 (13,128). This EPR-based model proposed two beta-strands at the following positions: $IAPP_{12-19}$ and $IAPP_{31-36}$. This model is the only one describing a stagger of the two strands about three peptide layers (**Fig.14 A**) (128). In this study, the fibril was a left-handed helix that contained IAPP monomers in a novel staggered conformation. The two beta-strands of the monomer adopted out-of-plane positions and were staggered by about three peptide layers (~15 Å). In figure 14 B the two strands separation is indicated with a red dashed line.

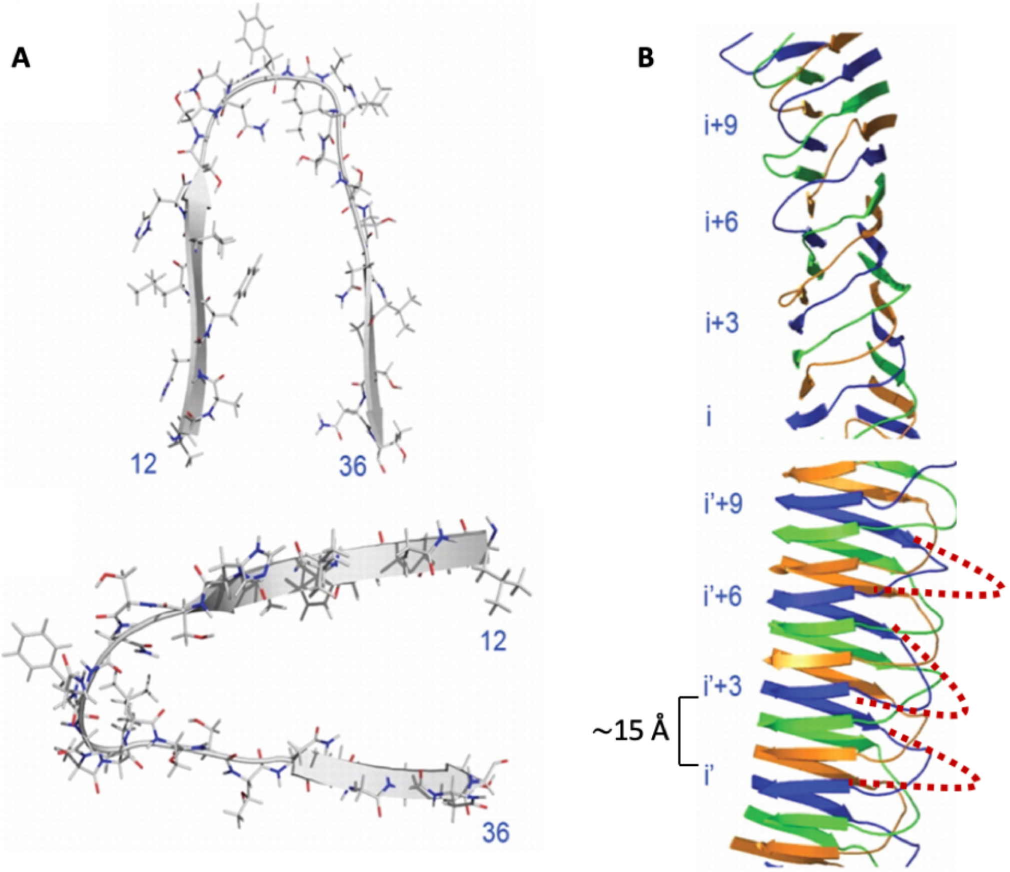

Figure 14. A. IAPP monomer according to EPR model, viewed along the fibril axis (top) and viewed along an axis orthogonal to the fibril axis (bottom), showing the stagger of the two beta-strands of the IAPP peptide. B. A section of the structural model showing the stagger of the IAPP peptides shown as blue, green, and orange ribbons displayed with the axes of beta-strands perpendicular and orthogonal to the fibril. Image adapted from (128), the ~15 Å distance between the three peptide layers and the red dotted lined indicating the strands stagger were added.

The last model is based on an amide proton solvent protection study, a method to study a supramolecular complex of amyloid fibrils. (134). In this case, a different type of chemical exchange process was employed to have information about amide protons involved in a secondary structure and their stability. After lyophilising a D_2O-dissolved protein, it is dissolved in DMSO, which has a double function: firstly, dissolving any amyloid structure in their monomeric forms, secondly, as an aprotic solvent, DMSO has no labile hydrogen atoms that potentially exchange with amide hydrogen of proteins (135). Consequently, a significant deceleration of the hydrogen/deuterium exchange reaction allows to monitor the exchange reaction in a larger window of time (134,136).

This model based on an amide proton solvent protection investigation shared partially similar beta-strand regions as the ssNMR model, in particular including His18 as the last residue in the first strand beta. His18 plays a central role, since its ionisation state is critical in determining the pH dependence of fibrillisation (137) and because replacement of His18 with positively charged arginine reduces amylin toxicity (138). In addition, with this method, residues Ile26 and Leu27 were described as more protected, so more conformationally constrained. By showing a higher protection than the loop residues, therefore, Ile26 and Leu27 were included in the second beta-strand in this method.

In conclusion, the presence of two beta-strands per monomer is overall accepted throughout all models (128,131,133,134), except for the serpentine one, suggesting three beta-strands (130). The exact length and position of the strands differs in the models described (**Fig. 12**). The described dissimilarities could be explained by polymorphism, due to different sample preparation protocols (139,140). Regarding the controversial amyloidogenic sequence $IAPP_{20-29}$, it is surprising that it is not a constant part of secondary structure, quite the opposite, it is mostly regarded as part of a random coil loop.

2. Aim of this work

My aims were to study the role of glycation, a post translational modification, PTM, consisting of the non-enzymatic addition of sugars to proteins, on the structure, aggregation pathway and toxicity of two peptides involved in T2D and AD: IAPP and Abeta, respectively. Therefore, my aim was to investigate the molecular mechanism leading to amylin and Abeta misfolding and subsequent aggregation and the role of glycation on these inexorable processes in proteinopathies.

These diseases, also known as protein misfolding diseases, refer to a class of diseases in which specific proteins fail to fold into their physiological configuration and lose their normal function. When this occurs, the protein undergoes a misfolding process and eventually converts into intractable aggregates, of which the most typical examples are amyloid fibrils. The diseases characterised by amyloid plaques formations are several and vary from neurodegenerative disorders, such as AD, to metabolic conditions, such as T2D. Increasing evidence suggests a link between T2D, mainly characterised by hyperglycaemia (high blood glucose) and AD, which causes a progressive loss of brain cells that leads to memory loss. These two diseases affect very different parts of our body but may have a common aetiological trigger. The molecular mechanism of these diseases' pathology is still area of contention.

The molecular mechanisms of amyloid formation of glycated aggregation-prone peptides remain unknown. I planned to clarify how glycation is involved in the self-assembling of Abeta and IAPP using biophysical and structural approaches. The chosen glycating agent was methylglyoxal (MGO), a three-carbon atom dicarbonyl metabolite obtained from glucose glycolysis, highly reactive towards free amino groups of proteins producing advanced glycation products (42,141).

I used several biochemical and biophysical techniques ranging from fluorescence and CD spectroscopy to AFM and NMR. Mass spectrometry was employed to map the glycation reaction sites of the peptides. By means of fluorescence-based assays, glycation and aggregation kinetics were followed at the same time. The occurrence of glycation was confirmed by the formation of the fluorescent argpyrimidine and aggregation was followed by ThT-binding assays, where the enhanced fluorescence corresponded to amyloid-like structure formation. Circular dichroism and nuclear magnetic resonance revealed the peptides secondary structure variation upon glycation. Finally, I evaluated the morphological effects of glycation on amyloid fibrils by atomic force microscopy.

An important output of this study was to find commonalities and differences between AD and T2D, two disease that have been treated very separately so far. The outcome of the work here presented could represent a little piece of a bigger puzzle which may help with the identification of a new target and novel approaches to these two diseases. By identifying the common cause of AD and T2D, the final aspiration is to improve the age of risk diagnoses, with subsequent effect upon patient quality of life and social and economic impact.

3. Techniques employed

3.1. Circular dichroism spectroscopy

Circular dichroism (CD) spectroscopy is a widely-used method to gain low-resolution structural information about proteins and peptides in solution (142). In particular, it is frequently used to determine protein and peptide conformations and conformational changes, and it has been employed to characterise the secondary structure of all peptides produced in this study.

Circularly-polarised light consists of an electric and a magnetic field, perpendicularly oscillating. The electric field does not change its strength but only its direction, in a rotary fashion, so that the tip of its vector describes a helix along the direction of propagation (**Fig. 15 A)**. Circular dichroism results from the interaction of a chiral chromophore with circularly polarised light and measures the difference between the absorption of left-handed circularly polarised light (Lcp) versus right-handed circularly polarised (Rcp) light. The absence of a difference yields an absence of CD signal, which is indicative of the absence of a regular structure; any difference, positive or negative, results in variation of the absorption of the light and a consequent positive or negative intensity signal in the CD spectrum.

When the left and right circularly polarised components are in-phase with equal amplitude and wavelength, the superimposition of their vectors results in a line. This is what happens before the beam passes through the sample in a CD spectrometer. When circularly polarised light hits an optically active compound in solution, for example a peptide with a definite structure, the beam is perturbed by an asymmetric sample, the two circularly polarised components (L and R) will be absorbed differently, and the projection of their vector will describe an ellipse, rather than a line. The rotation angle θ is defined as:

$$\theta = {}^{\pi C}(\varepsilon_L - \varepsilon_R) / \lambda$$

The projection of the field vector defining the ellipse can be found in figure 15 A.

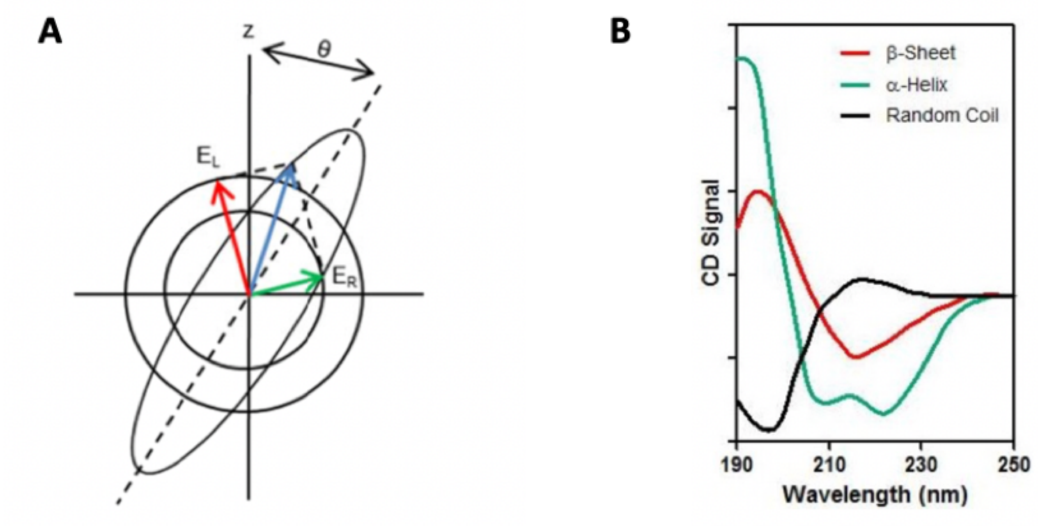

Figure 15. A. Ellipse described by the left and right polarised components when perturbed by an asymmetric chromophore. Red arrow (EL): field vector of left polarised light. Green arrow (ER): field vector of right polarized light. Blue arrow: projection of the superimposed vector, describing the ellipse. Θ is the degree of optical rotation. B. Characteristic CD spectra of alpha-helical (green), beta-sheet (red) and random coil (black) conformations.

Peptides and proteins are ideal molecules to be studied by circular dichroism, because they consist of chiral amino acids connected via peptide bonds, which serve as chromophores and interact with the beam of light. The peptide bond, or amide bond, most efficiently absorbs light at wavelengths shorter than 250 nm. To gain information about the secondary structure of a certain peptide, the result of CD spectroscopy, the CD spectrum, must be considered to be a series of bands corresponding to different electronic transition states, from the ground state to an electronically excited one. In peptides and proteins, the two characteristic transitions are the π-π* transition, occurring at 190 nm, and the weaker n-π* transition, at 210 nm. The singularity of the hydrogen-bond network, characteristic of each secondary structure, results in different CD spectra, as shown in **figure 15 B**.

In nature, proteins are generally composed of more than one type of secondary structure and the corresponding CD profile is a proportional combination of their contributions. The CD spectra of a certain peptide or protein can be deconvoluted as the sum of the α-helix, β-sheet and random coil contributions:

$$CD_{\text{protein}} = AX_{\alpha\text{-helix}} + BX_{\beta\text{-sheet}} + CX_{\text{random coil}}$$

where X represents the contribution of each secondary structure to the global spectrum, and A, B and C are the data points corresponding to the ideal spectra of the three conformations. Strong minima at 222 nm and at 208 nm, together with an intense maximum at around 192- 195 nm, are representative of an α-helix, since it correlates with the hydrogen-bonding environment of this conformation; the β-sheet conformation is represented by a single minimum between 210 nm and 220 nm, and a positive peak of similar intensity between 190 nm and 200 nm. Many denatured proteins and peptides, oligopeptides and polypeptides possess a CD spectrum typical of a random coil, with a single minimum near 195 nm and very weak positive, broad bands between 220 nm and 230 nm. Such a CD profile means that their building blocks are still bonded together but there is no well-defined hydrogen-bonding network between them. The interpretation of a CD spectrum is not always straight forward, although it is generally easier for short model peptides.

3.2. Thioflavin T-binding assay

Thioflavin T (ThT) is a dye extensively used to monitor amyloid formation over time in a fluorescence-dependent way. ThT was firstly described as a potent fluorescent marker of amyloid like-structures in 1959 by Vassar and Culling (32). In particular, it was pointed as far superior to other routine amyloid dyes such as Congo red or methyl violet (32). In the late 1980s the ThT fluorescence spectra and binding properties were characterised by LeVine and Naiki et al. (143-147). It was described that, upon binding to amyloid fibrils, or to structures containing cross-beta bonds, ThT shows a significant shift of its emission and excitation maxima (143,145).

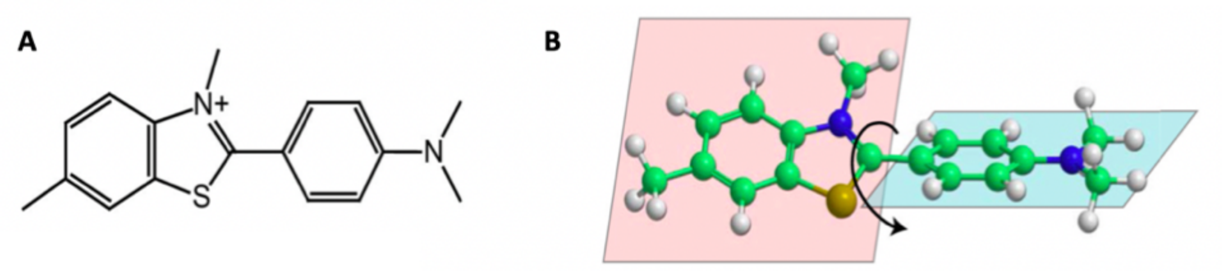

Figure 16. A. Chemical structure of ThT. B. The two planar segments of ThT whose mutual rotation defines chirality are also shown. Modified from (32).

ThT molecule consists of a benzylamine and a benzathiole ring connected through a carbon-carbon bond (**Fig. 16 A**). When free in solution, a low energy barrier allows for free rotation around this C-C bond (**Fig. 16 B**), feature which quenches the excited states of the molecule when hit by a photon beam. In these conditions, the maximum reported excitation and emission wavelength for ThT are 385 nm and 445 nm, respectively (**Fig. 17**) (143,146).

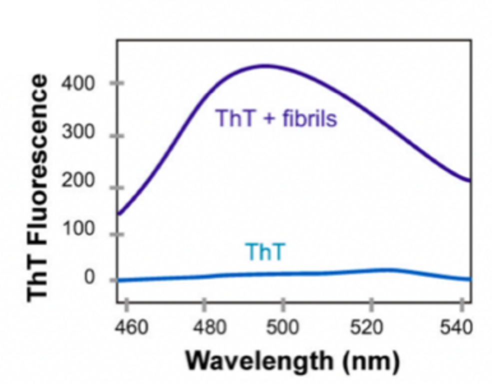

Figure 17. A. Characteristic increase in ThT upon binding to amyloid fibrils and low fluorescence emission for free ThT. Modified from (6).

When ThT binds to cross-beta type structures, such as in amyloid aggregates, the dye emits enhanced fluorescence and also a characteristic red shift of its emission spectrum is observed (148). As it is generally believed, the significant increase in ThT fluorescence is caused by the selective immobilisation of the molecule in a conformer which better maintains the excited state. (149). Upon binding to amyloid-like structures, the rotation around the carbon-carbon bond between the benzylamine and benzathiole rings of ThT becomes limited. In this conformation, the spectral characteristics of ThT change: its excitation maximum moves from 385 nm to 450 nm and its emission maximum from 445 nm to 485 nm (143,145).

The position in which the ThT becomes “blocked” seems to be in between the sheets of a cross-beta-rich structure and the more abundant the cross-beta structures, the higher the intensity of the ThT emission bond to them.

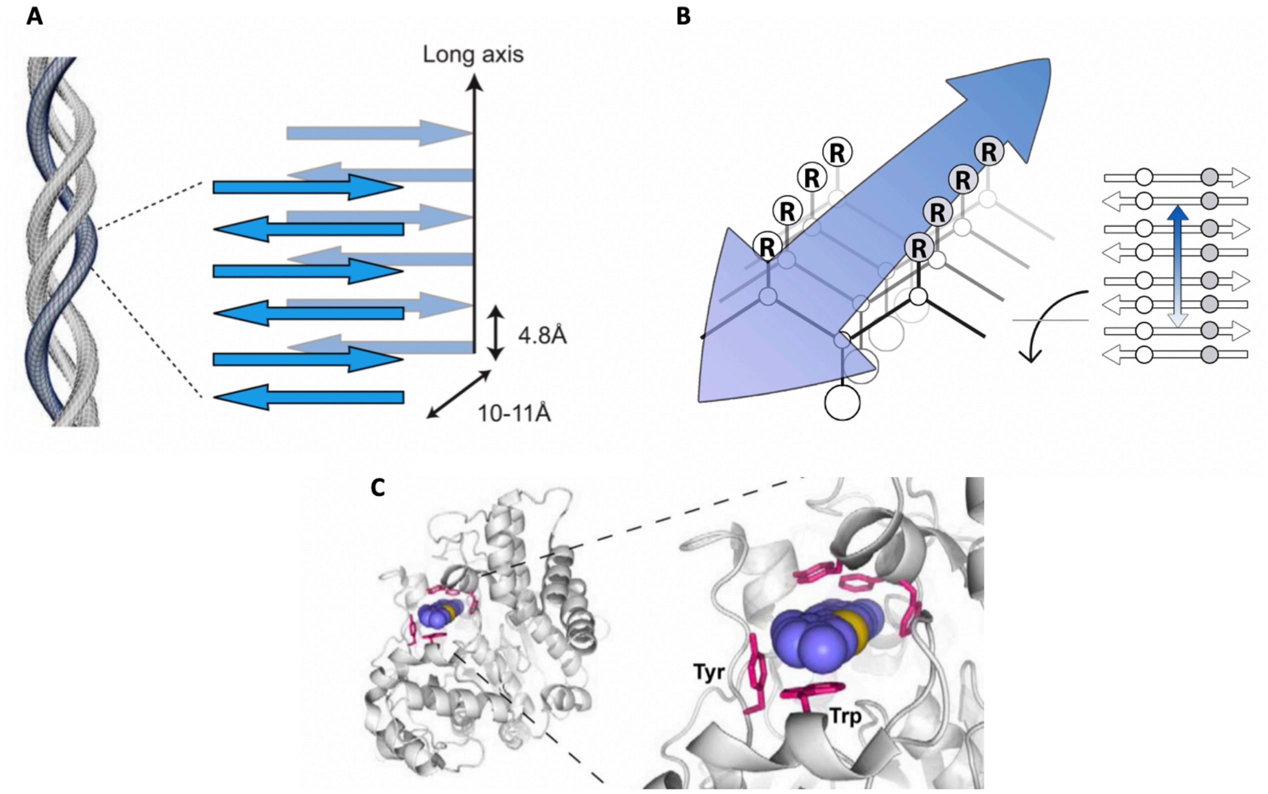

Figure 18. A. The common structure of fibrils and a structural rationale for fibril-ThT interactions. Cross-beta structure of amyloid fibrils (right), formed from layers of laminated beta sheets (6,150). B. "Channel" model of ThT binding to fibril-like beta sheets. ThT is described to bind along surface side-chain grooves running parallel to the long axis of the beta sheet. C. Crystal structure of ThT bound to acetylcholinesterase. (PDB 2J3Q). Modified from (151). Acetylcholinesterase is shown in cartoon representation in grey. All residues within 4 Å of ThT are shown as red sticks, except for Tyr121, which is omitted for clarity. The aromatic residues (Tyr and Trp) forming ThT-binding surfaces are labelled. The carbon, nitrogen and sulfur elements of ThT are in lavender, blue, and yellow, respectively.

A large number of structural models on the process by which ThT binds to amyloid fibrils have been suggested. The fact that ThT binds to fibrils originated by different proteins, regardless of their amino acid sequences, strongly supports the theory suggesting that ThT recognises a structural feature common among fibrils. The ThT-binding site could be the surface of the cross-beta architecture.

The cross-beta architecture is characterised by laminated beta sheets whose strands run perpendicular to the long-axis of the fibril (**Fig. 18**) (6,150). This beta-rich composition produces the characteristic strong reflections at about 4.7–4.8 Å and 10–11 Å observed in X-ray diffraction experiments of amyloid fibrils, which are interpreted as the strand spacing within and between beta-sheet layers, respectively (**Fig. 18**) (150,152).

The cross-beta framework of fibrils (**Fig. 18 A**) is characterised by a characteristic adjustment of side-chains called "cross-strand ladders", oriented between the beta-strand layers (**Fig. 18 B**) (153). In amyloid fibrils, the distribution in rows of the cross-strand side-chains occur irrespective to the peptide sequence and these side chains form extended channel-like motifs along solvent-exposed surfaces of fibrils. As a result, these channel-like pockets could be the binding site of linear dyes such as ThT. This hypothesis is described as the "channel model".

Another example is the "self-association model", which considers the self-association of ThT at the centre of its theory. The ability of ThT to self-associate into micelle was recorded in few occasions, but the critical micelle concentration (CMC) is still under debate (6,154-156). The estimated CMC by Khurana *et al.* is 4 µM (156), whereas subsequent reports identified it around 30 µM (154). As the ThT concentration commonly used for the binding assay is around 10-20 µM, under these conditions it should not be possible to incur into micelles formation.

To date, none of the possible models can adequately describe the chiral feature of ThT bound to amyloid fibrils (149,157) nor its propensity to bind parallel to the long axis of the fibrils (158). In addition, investigation on ThT binding cooperativity reported that independent ThT molecules often bind at a single type of site (146). Whereas the self-association model could give explanations about the promiscuous ability of ThT binding partners, it is nevertheless contradictory with several recent works describing specific molecular interactions of ThT with the surface of the cross-beta architecture of fibrils (6,159,160).

Despite its demonstrated utility as an amyloid stain, substancial concerns over potential cross-reactivity of ThT led to several important studies investigating its specificity. In particular, ThT's ability to bind hydrophobic pockets in globular proteins has been extensively characterised. The crystal structure of ThT bound to acetylcholinesterase demonstrated that the dye binded in a site formed primarily of α-helices, in striking contrast to cross-β fibrils (**Fig. 18 C**) (151). Interestingly, nearly all contacts with ThT were mediated by aromatic residues in the binding pocket, including extensive π-stacking with Tyr and Trp.

ThT has also been shown to bind to a hydrophobic pocket of human serum albumin with comparable affinity to many drug-like molecules (161). ThT's capacity to interact with hydrophobic pockets in non-fibrillar proteins may rise concerns about its binding selectivity. For this reason, several controls should be carried out to verify that ThT does not stain the starting materials when used as a fibrillisation reporter, especially in cases of fibrils formed from associations of globular proteins.

In conclusion, the molecular mechanism underlying the ability of ThT to recognise diverse types of amyloid fibrils and potential cross-reactivity of ThT with hydrophobic pockets in non-fibrillar proteins cannot propose ThT as the ideal tool to selectively staining and identifying amyloid fibrils.

Although ThT may not be the perfect tool to study amyloid formation, it has been one of the most widely used dyes for monitoring amyloid formation since the 1960s. Further research into the molecular mechanism of ThT interactions with fibrils are required to fully understand amyloid formation, kinetics, structure, and pathogenesis. Complementary techniques can be taken in account to identify and confirm cross beta binding such as X-ray diffraction.

3.3. Mass Spectrometry

Mass spectrometry (MS) is an analytical technique employed to identify the molecules by measuring their mass-to-charge ratio. MS works by ionisation of the analyte, which produces gas-phase charged species. In protein analysis, the two most common methods of ionisation are matrix-assisted laser desorption/ionisation (MALDI) and electrospray ionisation (ESI). For the analysis of large molecules such as proteins, peptides and DNA, mass spectrometry with MALDI is the standard method. Generally, the type of a mass spectrometer most widely used with MALDI is the TOF (time-of-flight mass spectrometer), measuring the time it takes for the molecules to travel a fixed distance.

MALDI is a technique that involves diluting the protein in an organic solvent solution, in most composed of a small organic acid absorbing in the UV region such as acetonitrile. Such prepared sample is then deposited on a stainless-steel matrix. By deposition on a MALDI sample plate and by subsequent drying, crystallization of the protein occurs on the matrix. This plate is then inserted into a mass spectrometer and a pulsed UV-emitting laser is directed to the sample. Ionisation occurs by photon bombardment with minimal fragmentation.

In contrast to MALDI, ESI produces ions by applying a strong electric field to a liquid to create an aerosol. This type of MS is particularly useful when analysing proteins and peptides, since it overcomes their propensity to fragment during ionization. Moreover, both MALDI and ESI are often coupled with liquid chromatography to separate the peptides in complex mixtures before ionisation.

3.4. Liquid chromatography–mass spectrometry

Liquid chromatography–mass spectrometry (LC-MS) is an analytical chemistry technique that combines the physical separation power of high-performance liquid chromatography (HPLC) with the mass analysis capabilities of mass spectrometry (**Fig. 19**). While liquid chromatography isolates the individual component from a mixture, mass spectrometry provides the structural identity of the sample. The combined technique derived from the combination of MS and HPLC is commonly known as LC-MS. The use of LC-MS reduces experimental error and improves accuracy.

The mobile phase in a liquid chromatography system is a pressurised liquid, while the MS analysers commonly operate under vacuum. As it is not possibile to directly pump the eluate coming from the column directly into the MS source, the LC-MS system requires an extra interface that efficiently transfers the separated components from the liquid chromatography column into the MS ion source. Overall, the interface is a mechanically simple part of the LC-MS system that has the role of desolvation, to remove the solvent from the eluate, and ionisation, to generate the gas phase analyte ions.

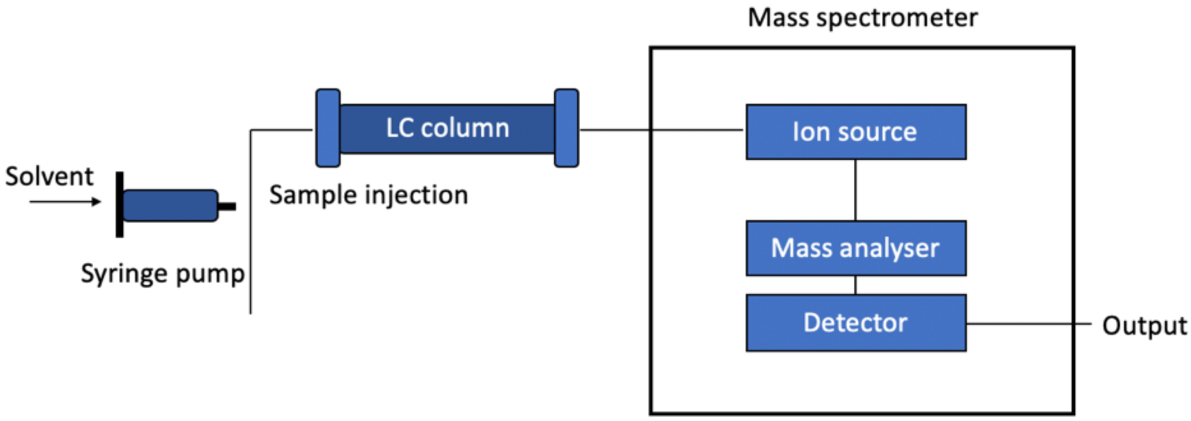

Figure 19. Schematic diagram of liquid chromatography–mass spectrometry. After elution through a HPLC, the mass spectrometer separates the ionised molecules that have been transferred to the gas phase. Ions are then separated according to their mass and charge (m/z) in the mass analyser.

3.5. Atomic Force Microscopy

Developed in 1986 by Binning, Gerber and Quate, as a collaboration between IBM and Stanford University, AFM reconstructs the three-dimensional morphology of a sample on a flat surface by monitoring distance-dependent interaction forces between a sharp probe and the sample (**Fig.20 A**) (162).

The probe used is a microfabricated sharp tip, typically less than 5 μm tall and often less than 10 nm in diameter at the apex. The tip is attached at the free end of a flexible cantilever that is usually 100–500 μm long. (**Fig.20 B**) The probes can be made of silicon or silicon nitride, and they can have pyramidal or conical shape (163).

AFM scanners are made from piezoelectric material, which expands and contracts proportionally to an applied voltage. The scanner is designed by integrating five independently operated piezoelectrodes, into a single tube, forming a scanner which can manipulate samples and probes with extreme precision in vertical (Z) and horizontal (X, Y) directions. In some models (e.g. MultiMode SPM) the scanner tube moves the sample relative to the stationary tip, which is the most common mode. In other models (e.g., STM, Dimension Series and BioScope SPM's) the stationary part is the sample, whereas the scanner moves the tip (163). The sample lies on a piezoelectric tube, made of piezoelectric ceramic, that elongates or contracts depending upon the polarity of the voltage applied (**Fig. 20 C**).

Forces between the tip and the sample surface cause the cantilever to bend and deflect. The cantilever deflections are measured by a photodiode detector and processed by a computer to generate a map of surface topography (163). There are different tip-sample interaction forces and they can be identified as repulsive and attractive interactions. In the absence of external magnetic and electric fields, short-range repulsive interactions are dominant. Pauli repulsion take the lead at a close tip-sample distance ranging from sub nanometre to a few nanometres, while attractive forces such as van der Waals interactions and capillary forces prevail at distances above few nanometres. In addition, in both regimes, viscoelastic and adhesive interactions can also be present (22,164).

In other words, the forces between the tip and sample are directly influenced by the separation distance. As the tip and the sample are gradually closer, their atoms start to weakly attract each other. These attraction forces increase until the atoms are as close that their electron clouds cause repulsion forces. This electrostatic repulsion progressively weakens the attractive force as the separation continues to decrease.

An AFM can operate in static (contact) or dynamic mode (tapping or non-contact mode) (**Fig. 20 D**). The static mode, also called contact mode, operates by scanning a tip attached to the end of a cantilever across the sample surface while monitoring the change in cantilever deflection with a split photodiode detector. The elastic deformation of the cantilever caused by the tip-sample repulsion can be directly measured. In particular, deflection of the cantilever is measured using an optical lever method, by means of a laser beam focusing on the back of the cantilever. Thus, data points are stored by a computer to form the topographic image of the sample surface.

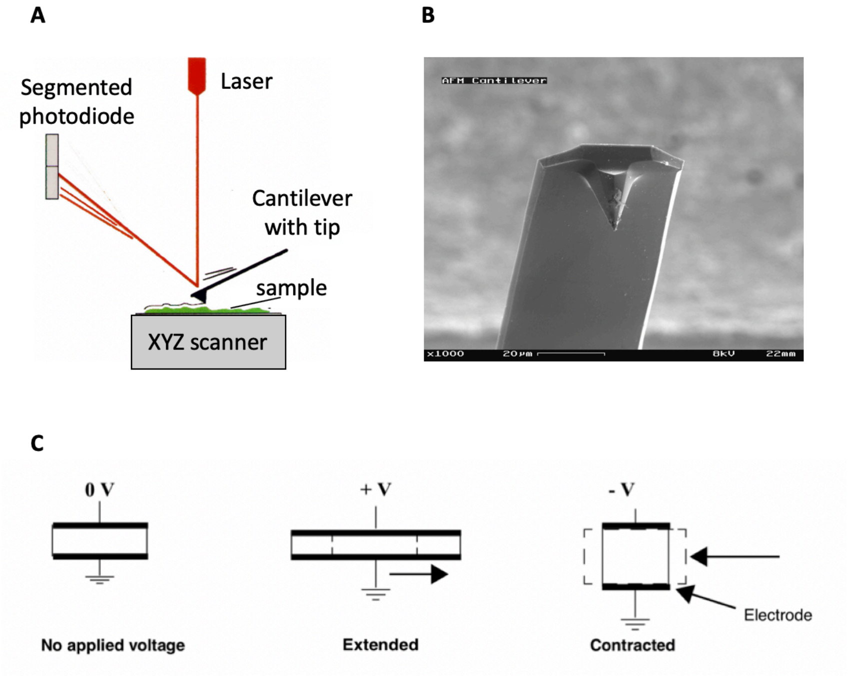

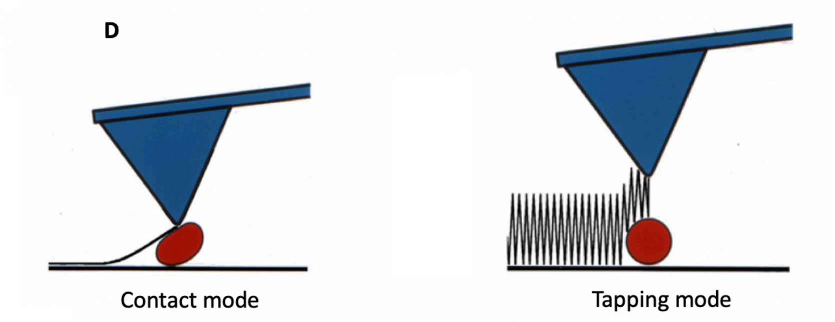

Figure 15. A. Simplified representation of an atomic force microscope. The atomic force microscope builds up the three-dimensional morphology of a sample on an atomically flat surface by raster-scanning a small tip over the sample surface. The tip is attached at the end of a cantilever, which creates a specific deflection. The characteristics of the deflection is dependent on the characteristic according to the features that the tip encounters on the sample surface and it is detected with an optical lever (red line): a laser beam reflecting off the end of the cantilever onto a segmented photodiode detector. B. Electron micrograph of a used AFM cantilever. Image width ~100 µm (165). C. The effect of applied voltage on piezoelectric materials, which can expand or contract in presence of a positive or negative magnetic field (161). D. AFM operation modes. Contact mode, when scanning the is constantly in contact with the sample surface. Tapping mode when the tip is intermittently brought in contact with the sample. Modified from (166).

These images of the sample are obtained by maintaining a constant deflection and hence force, of the cantilever during the scanning. The cantilever deflection x is proportional to the interaction force F, as described by the Hooke's law F = k·x, where k is the cantilever's spring constant. When the laser spot moves on the detector, the feed- back system reacts by extending or retracting the piezo actuator along the Z axis to compensate deviation of the cantilever deflection from the chosen set point.

Two main dynamic modes can be identified: tapping mode, in which the tip is intermittently brought in contact with the sample and non-contact mode, where there is weak tip-sample mechanical contact.

The tapping mode is most commonly used for biological samples (162) and it operates by scanning a tip attached to the end of an oscillating cantilever across the sample surface, so the tip lightly taps on the sample surface during scanning, touching the surface at the bottom of its swing. The cantilever is oscillated with a frequency much faster than the lateral scan and with an amplitude ranging typically from 20nm to 100nm.

The interaction forces between tip and sample produce nonlinear dynamics. The movement of the cantilever is caused by both the nonlinear tip-sample interaction force and the sinusoidal driving force (**Fig. 22**). The scanner position at each (x,y) data point to maintain a constant setpoint amplitude is processed by the computer to obtain the topographic image of the sample surface.

AFM operation in contact mode can damage or distort some soft biological samples. On the other hand, very soft and fragile samples can be imaged successfully in tapping mode by oscillating the tip over the sample, and by making only brief intermittent contacts. For this reason, tapping mode is the operation mode chosen in this thesis to identify and characterise the morphological different oligomeric populations of aggregation-prone proteins.

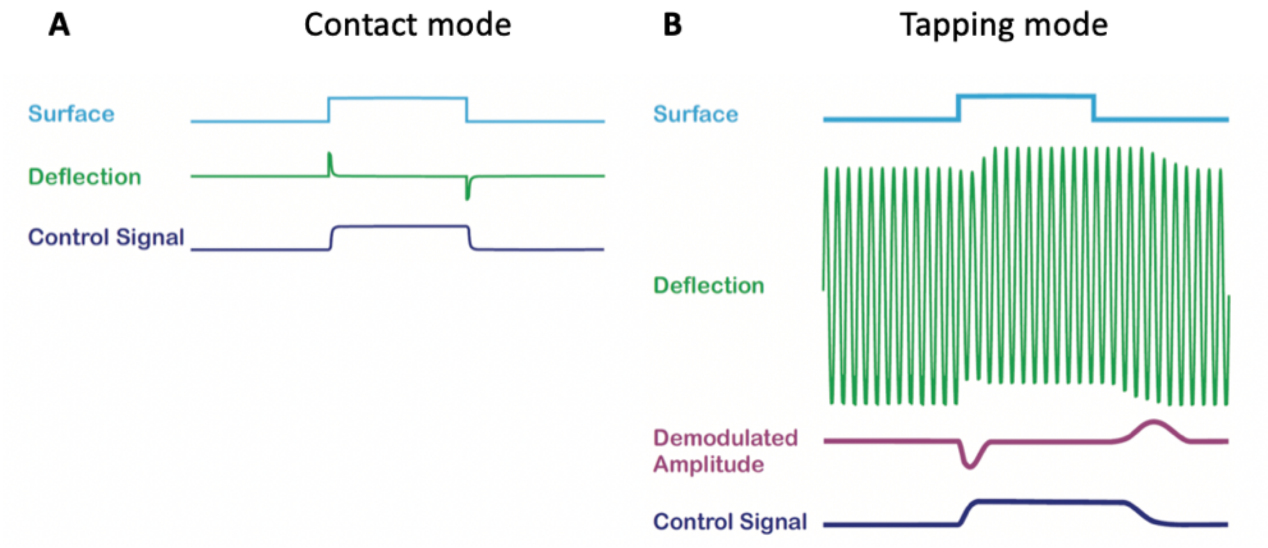

Figure 16. Feedback operation to measure sample topography. A. Deflection of the AFM tip in contact mode. Note that the optical lever gives a signal proportional to an error signal. The control signal being sent to the actuator is a good, albeit band-limited, representation of the surface. B. Deflection of the AFM tip in tapping mode. In tapping mode, the drop-in oscillation amplitude results in the feedback loop raising the position of the Z scanner, which restores the oscillation amplitude. A rise in oscillation amplitude results in the controller lowering the position of the Z scanner. The control signal can then be used as a representation of the surface. Image adopted from (167).

3.6. Nuclear Magnetic Resonance

Nuclear magnetic resonance (NMR) was first described and measured in molecular beams by Isidor Rabi who was awarded the Nobel Prize in physics for this work in 1944. Two years later, Felix Bloch and Edward Mills Purcell demonstrated that nuclear magnetic resonance could be detected also in condensed phases, i.e. liquids and solids, a discovery for which they shared the Nobel Prize in physics in 1952. In the last few decades NMR has been used routinely to investigate chemical compounds, proteins and complexes. The method relies on intrinsic spin properties of nuclei.

Discovery of nuclear magnetic resonance, in turn, originated nuclear magnetic resonance spectroscopy, the most powerful analytical spectroscopy for chemistry and biology so far. The core of this spectroscopy resides in the possibility of obtaining information on the chemical environment of specific nuclei from information about the nuclei.

Protons and neutrons have an intrinsic angular moment as if spinning on their axes. Angular moments can be associated to a magnetic moment. In many atoms the spins of nuclear particles are paired, with the consequence that the nucleus of the atom has no overall spin, but in some atoms, notably the obvious case of ^{1}H or ^{13}C, the nucleus has an overall spin.

According to the rules of quantum mechanics a nucleus of spin I has 2I+ 1 possible orientations. Thus, nuclei with spin 1/2 which are those most commonly used in NMR spectroscopy, e.g. ^{1}H, ^{13}C and ^{15}N, will have two possible orientations. When the nuclei are not immersed in an external magnetic field, the two orientations have equal energy. If a magnetic field is applied, the energy levels separate, with the one along the external field of lower energy.

The lower energy level will be populated with a tiny excess of nuclei than the higher level. Irradiation with electromagnetic radiation in the radio frequency range can equalise the populations giving rise to a resonance signal.

However, the actual magnetic field experienced by a nucleus is slightly different from the external magnetic field because the nucleus is shielded by local electron density originating from chemical bonds. This difference gives rise to chemical shifts that are typical of different chemical groups. Chemical shifts are generally expressed in units of parts per million (ppm) with respect to the frequency of a reference compound.

The chemical shift yields information about the structure of molecules. The classical example from the early days of NMR spectroscopy is the proton-NMR (^{1}H NMR) spectrum of ethanol. Instead of a single proton resonance it is possible to observe three distinct signals for the methyl, methine and hydroxy groups (**Fig. 22**).

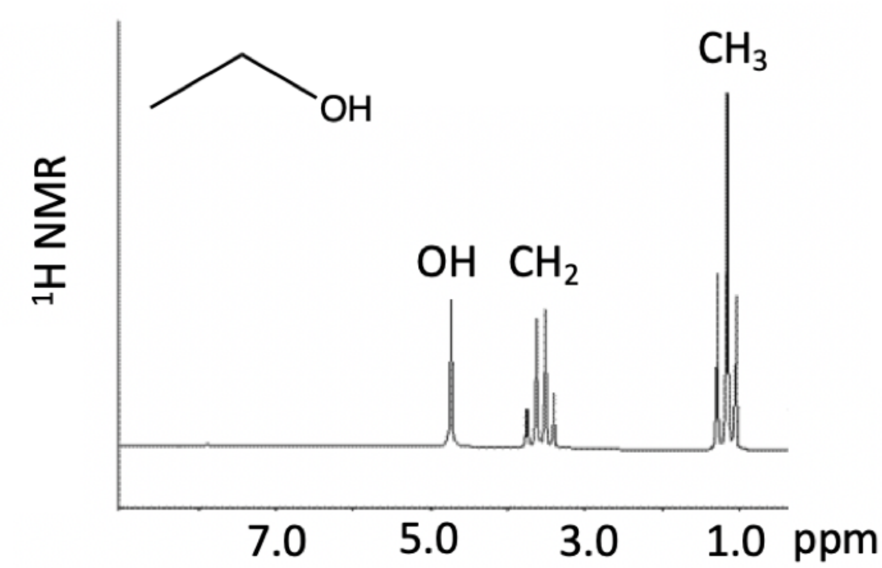

Figure 17. 1D ^{1}H NMR spectrum of ethanol with typical chemical shift differences among groups and J-coupling splittings. Ethanol chemical structure is displayed on the top left.

Additional information for structure determination arises from the so-called J-coupling between NMR nuclei. J-coupling arises from the interaction of spin states via chemical bonds and leads to the splitting of NMR signals. Coupling yields detailed information on the connectivity of atoms in a molecule.

A great improvement in NMR spectroscopy was the introduction of multi-dimensional techniques. The first such spectra were two-dimensional (2D NMR), a set of methods in which data are plotted in a space defined by two frequency axes. Among 2D NMR spectra, total correlation spectroscopy (TOCSY) and nuclear Overhauser effect spectroscopy (NOESY) are noteworthy. TOCSY gives information on connections via coupling and NOESY gives information on connections through space.

The TOCSY spectrum contains a diagonal and cross peak. Diagonal peaks have the same frequency coordinate on each axis and correspond to the peaks in a 1D-NMR spectrum whereas the cross peaks indicate couplings between pairs of nuclei, such as mutliplets, corresponding to correlations through bonds. An example of 2D TOCSY spectrum of 2,3- dihydrofuran is displayed in figure 23. The molecule 2,3- dihydrofuran shows resonances at d 2.6, d 4.2, d 4.9, d 6.2 ppm.

2D NMR spectroscopy provides much more information about molecular structure than 1D NMR and is particularly useful for molecules, such as proteins, that are too complicated to study with 1D NMR.

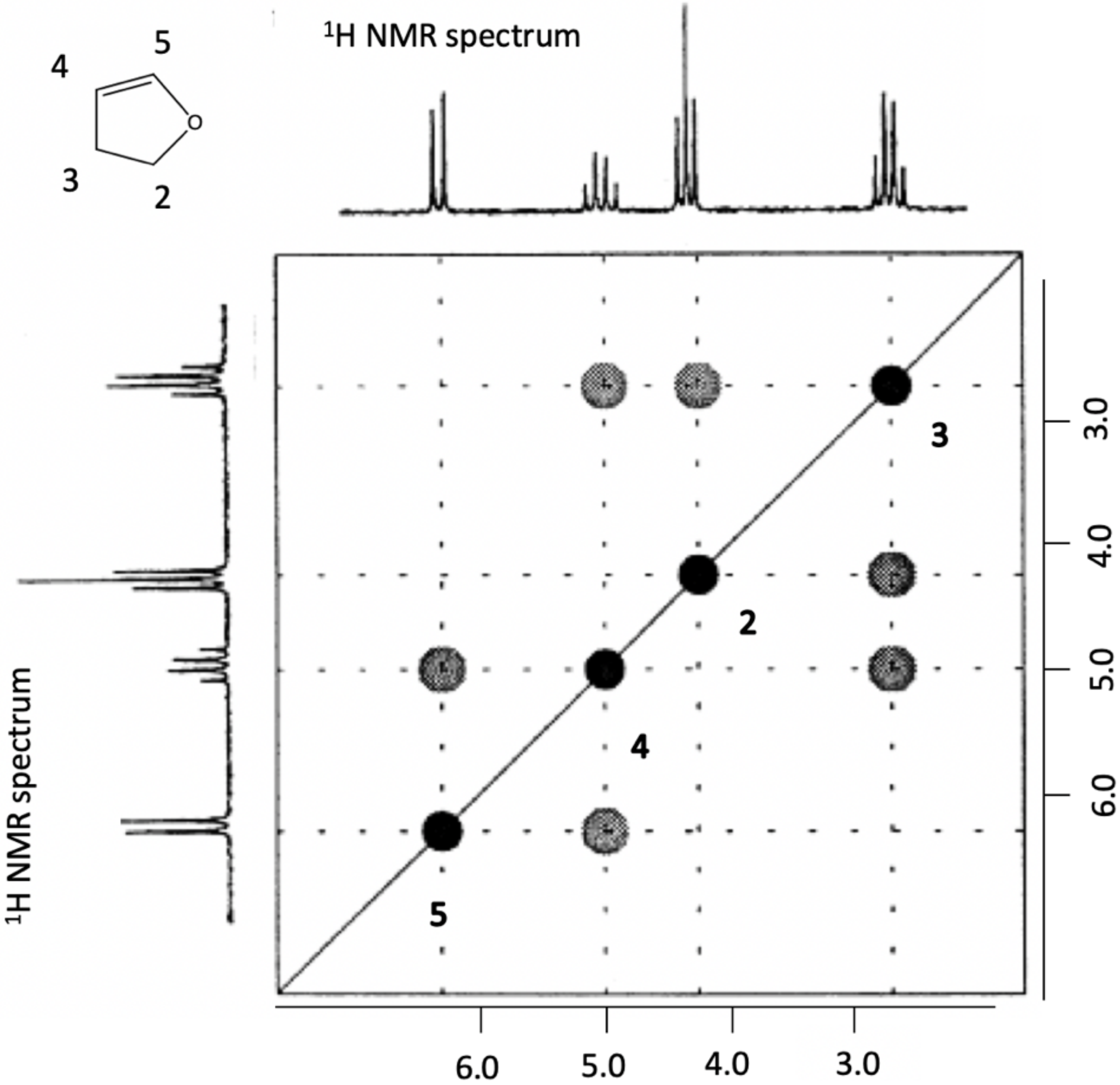

Figure 18. 2D TOCSY spectrum of 2,3- dihydrofuran, ^{1}H NMR spectrum is displayed on the top and left side of the 2D TOCSY spectrum. 2,3- dihydrofuran chemical structure is reported on the top left with numbers indicating the hydrogens reported on the 2D spectrum. Modified from (168).

3.7. Arginine as glycation site model

Glycation can occur on N-terminal amino acid groups, arginine, lysine and histidine residues, of proteins. Among the possible glycation products, the arginine-derived one (argpyrimidine) can be detected thanks to a fluorescent assay. For this reason, the amino acid arginine was used as a model to screen different glycation conditions in phosphate buffer at 37 °C. The fluorescent emission wavelength was screen from 360 nm to 600 nm maintaining excitation wavelength at 320 nm on a sample containing 500 µM arginine incubated with 100-fold ratio MGO in phosphate-buffered saline (PBS). Glycine and MGO were employed separately in the same conditions as negative control.

4. Material and Methods

4.1 Sample production

Abeta peptides (1-40 and 1-42) were purchased from rPeptide Inc (catalogue no. A1153-1 and A1163-1) as recombinant peptides. The peptides arrived lyophilised with 97% purity as determined by mass spectrometry and they were stored at -20°C until use.

Full-length IAPP peptide was obtained from Peptide 2.0 Inc with 98.43% purity and from Eurogentec with 95% purity. The peptide arrived lyophilised and was stored at -20°C until use. The sample contained the physiological modifications, such as the 2-7 disulfide bridge and C-terminal amidation as determined by mass spectrometry and reverse-phase HPLC.

The purchased peptides (1 mg) were always treated under strong acidic conditions with pure trifluoracetic acid (TFA), 1,1,1,3,3,3-hexafluoro-2-propanol (HFIP) or a combination of both to dissolve pre-existent fibrillar aggregates to reach the concentration of 1 mg/mL (87).

Abeta peptides were treated with a combination of these acids. Abeta variants were firstly incubated in TFA for one hour at room temperature and then ultrapure water was added to reach 10% (v/v) TFA concentration. After complete TFA removal by means of freeze-drying, Abeta peptides were dissolved in HFIP, which was removed by freeze-drying.

For IAPP, the treatment was carried out with one acid at a time. In particular, the choice of acid for the sample preparation was determined by the effect of the solvent on the peptide secondary structure (see in chapter "Results - IAPP aggregation studies"). The sample was mixed vigorously and visually inspected for efficient solubilisation. After one-hour incubation at room temperature in acid solution, the solution was diluted in ultrapure water and up to 10% (v/v) TFA and freeze-dried overnight in aliquots. This protocol allows dissolving possible aggregates and pre-formed aggregates and thus obtaining better reproducibility. The pre-treated protein was dissolved in PBS to a desired concentration. The glycated proteins were obtained by adding MGO in molar excess and the mixture was incubated at 37 °C.

4.2 Methylglyoxal preparation

Methylglyoxal (MGO) employed in glycation assay came either from a solution in ~40% water purchased from Sigma Aldrich (CAS number 78-98-8) stored at 4° C or from a solution prepared in house. High purity MGO was prepared from 2.27 mmol methylglyoxal 1,1-dimethyl acetal (also called pyruvaldehyde dimethylacetal) purchased from Sigma Aldrich (CAS number 6342-56-9) by acid hydrolysis using 5% H_2SO_4 in phosphate buffer, at 100°C for 25 min as reported (169). The acid hydrolysis method is quite reproducible. Purity and stability of the obtained MGO was verified by 1H NMR (Bruker advance 700 MHz).

Scheme 1. Acid hydrolysis of methylglyoxal 1,1-dimethyl acetal resulting in MGO. The reaction occurred in a solution of 5% H_2SO_4 in water at 100 °C and it was completed after 25 minutes

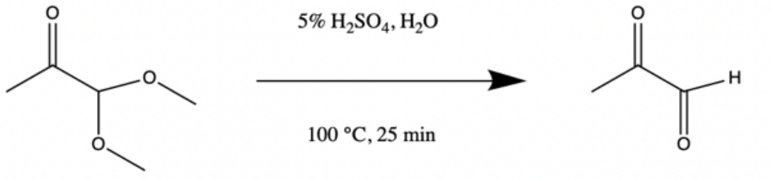

4.3 Fluorescence spectroscopy

Aggregation and glycation kinetics were followed by means of spectrofluorometric assays, using a FLUOstar OMEGA Lite instrument and a Jasco FP 6600 spectrofluorometer. Before each assay, the Abeta40, Abeta42 and IAPP peptides were prepared as previously described. To exclude any secondary effect of DMSO on the aggregation kinetics various concentrations of DMSO (1-10%) were screened and the concentration of 2% was chosen. Aggregation assays were performed in a Greiner UV-clear 96-well plate. Firstly, a 500 µM protein stock was prepared by adding pure DMSO to the lyophilised sample. Secondly, the protein was diluted from the DMSO stock to 10 µM in PBS pH 7.4, added with 20 µM ThT, in the presence and the absence of MGO (final concentration 1 mM), to obtain peptide:MGO ratios from 1:0 to 1:200. The temperature was set at 37 ˚C and the readings were performed every 15 minutes, setting the excitation wavelength at 440 nm and the emission wavelength at 485 nm. The plate was left quiescent between measurements and shaken for only 1 second before each reading. Glycation kinetics was followed using the same conditions as for the aggregation assays, but the reaction mixture did not contain ThT. The excitation wavelength was set to 320 nm and the emission wavelength to 405 nm. In both experiments, every condition was repeated at least 4 times and the results were normalised according to the corresponding blank and expressed as percentage.

4.4 Circular dichroism spectroscopy

Far-UV CD spectra were recorded in the range 200–260 nm on a Jasco J-1100 spectropolarimeter (Jasco, Essex, UK), equipped with a temperature control system, using a 1 mm quartz cuvette, using a peptide concentration of 10, 20 and 60 µM in 20 mM sodium phosphate, 15mM NaCl. Raw spectra were corrected for buffer contribution. The scanning speed was set to 200 nm/min, digital integration time to 1 sec, and the temperature to 37 °C for all experiments. To ensure reproducibility, all experiments were repeated at least three times on at least two different batches of peptides.

4.5 Identification of the reactive glycation sites by mass spectrometry

Mass spectra of both glycated and non-glycated Abeta42 were acquired by our collaborator Fabrizio Dal Piaz at the University of Salerno (Italy) using a MALDI-TOF Micro (Waters) instrument operating in reflectron mode. Mass calibration was carried out using a mixture of peptides obtained by proteolytic digestion of bovine serum albumin (BSA) with the bovine protease trypsin. The peptide underwent cysteines reduction and carbaminomethylation; after that it was digested overnight by trypsin at 37 °C while stirring. The digested fragments were analysed by nano-LC-MS using an Orbitrap XL instrument (Thermo Fisher Scientific) supplied with a nano-ESI source coupled with a nano-ACQUITY capillary UPLC (Waters). A capillary BEH C18 column (0.075 x 100 mm, 1.7 µm Waters) was used to separate the petide before ionisation. The solvent mixture employed as mobile phases was aqueous 0.1% formic acid (A) and acetonitrile containing 0.1% formic acid (B). Peptides elution occurred through a 45-min gradient from 5 to 50% B at a flow rate of a 300 nl/min. Mass spectra were collected over a 400 to 1800 m/z range.

4.6 Measurements of the fibre morphology

Atomic force microscopy (AFM) was carried out on samples pre-treated as for ThT-binding assay and dissolved in an appropriate volume of PBS to obtain a concentration of 100 µM. They were loaded onto freshly cleaved mica and incubated for 5 min at room temperature. The excess of liquid was dried off from the mica and rinsed with a gentle flux of filtered mq-H_2O. Samples were then incubated at 37 °C and images were acquired at different time points. Height peak force error images were obtained on a Bruker Multimode 8 microscope with a Nano scope V controller (Bruker UK Ltd., Santa Barbara, CA). Image data were acquired operating in peak force tapping mode using ScanAsyst Air cantilevers (115-µm nominal length, 25-µm nominal width, nominal spring constants of 0.4 newtons/m, and typical resonant frequencies of 70 kHz). The ScanAsyst probes have a 2-nm nominal tip radius of curvature. Image data were obtained at peak force frequency of 4 kHz and a line rate of 3 Hz at a resolution of 512 pixels/line. Different sample dilutions were applied according to image clarity requirements (1:10 and 1:100). After dilution, 100 µl of sample was loaded onto freshly cleaved mica and incubated for 5 min at room temperature. The excess of liquid was dried off from the mica and rinsed with a gentle flux of filtered mq-H_2O.

4.7 Nuclear magnetic resonance spectroscopy (NMR)

NMR spectra were recorded on a Bruker 700 MHz instrument at the Randall Division of Molecular and Cell Biophysics at King's College London. IAPP was diluted in either 10mM (pH 5.5) or 100mM (pH 7.4) sodium phosphate buffer, supplemented with 5% D2O, yielding a yielding a final protein concentration of 60 µM in each case. Experiments were conducted at 10°C and 37°C. The 1D spectrum was recorded and the 2D TOCSY (Total Correlation SpectroscopY) spectrum was obtained with 8 scans and spectral width of 11261 (x-axis) and 5630 (y-axis). To carry out the 1D, in each sample, 4,4-dimethyl-4-silapentane-1-sulfonic acid (DSS) was added as internal standard, exhibiting minor peaks at 2.91 ppm, 1.75 ppm, and 0.63 ppm at an intensity of 22% of the reference peak at 0 ppm in the proton spectrum.

4.8 IAPP production

The production of both rat and human isoforms was attempted. The rat isoform was initially used to test the expression and purification of IAPP, since this isoform is much less aggregation prone than the human one.

4.8.1 Transformation of IAPP fusion protein

IAPP coding region inserted into the pTXB1 plasmid from NEB was expressed in E. coli BL21 (DE3) cells. The plasmid also contains the gene that confers ampicillin resistance to the cells.
An aliquot of 15 µL of E. coli competent cells BL21 (DE3) was thawed at room temperature to carry out the heat-shock transformation. When the cells were evenly suspended, 100 ng DNA solution was added to the cells and gently mixed. After an incubation in an ice bath for 30 minutes, the cells were heat-shocked at 42°C for 90 sec and then transferred to an ice bath for 2 minutes. Then 500 µL of Luria-Bertani (LB) medium was added and the tube was placed in a 37 °C

incubator under shaking for 45 minutes. Finally, the cells were spun down at 1300 rpm for 2 minutes and 450 µL of supernatant was removed in order to facilitate the resuspension of the cells in the remaining LB medium. A desired portion of the mixture was plated onto a LB-agar plate supplemented with 50 µg/ml ampicillin. The plates were incubated at 37 ° C overnight and the day after were grown in LB supplemented with ampicillin until they reached an optical density at 600 nm (OD_{600}) of 0.6. Glycerol stocks were made by mixing 200 µL of cells with 200 µL of sterile glycerol and frozen at -80°C.

4.8.2 Expression of IAPP fusion protein

All purification steps were carried out at 4°C and protein samples were stored on ice whenever possible unless otherwise stated. Affinity-columns were purchased from GE Healthcare, column-based purifications were carried out on ÄKTApurifier systems from GE Healthcare.

The starter culture was directly inoculated from a glycerol stock using a sterile loop and grown overnight at 37°C under shaking. Overnight cultures were diluted 1:50 in LB medium supplemented with 100 µg/mL ampicillin and shaken at 37°C, 120 rpm for 3 hours or until an OD_{600} of 0.7 was reached. 1 mM isopropyl-beta-D-thiogalactopyranoside (IPTG) was added to induce over-expression and the cells were incubated overnight at 18°C under shaking.

The following day, the cells were centrifuged at 4000 rpm, 4 °C for 20 min and the cell pellet was resuspended in elution buffer (20 mM Hepes pH 8.0, 0.1 mM EDTA, 50 mM NaCl, 2M Urea). 25 mL of resuspension buffer were used per 1L cell pellet. The pellets were stored at -20°C.

4.8.3 Purification of IAPP

The protein purification process was adapted from Williamson et al (170) and Rodriguez, Camargo et al protocol (171).

Bacterial pellets suspended in elution buffer were lysed via pulsed sonication for 5 min on ice (50 sec duty cycle, output intensity 5) and the crude protein extract was cleared by centrifugation at 5000 rpm for 15 min at 4 °C. The lysate was centrifuged at 12000 rpm for 30 min at 4°C. No lysozyme was added in this step to prevent degradation of the chitin beads. The cell lysate was purified by affinity chromatography using a chitin-bead gravity flow resin purchased from NEB. The chitin column (30 mL of chitin beads bed volume) was equilibrated with three column volumes of elution buffer. The lysate was loaded onto the column and left incubating at 4°C overnight to allow for optimal binding of the CBD to the beads. Then the column was washed with 15 column volumes of elution buffer to remove unbound proteins. The intein cleavage reaction was initiated by addition of 60 mL of chitin buffer (elution buffer supplemented with 100 mM DTT and 2 M ammonium bicarbonate). Ammonium bicarbonate in the buffer is required to yield amidation of the C-terminus (111). After elution of approximately 20 mL, the column flow was stopped, and the content was left under continuous rotation overnight at 4 °C. The protein was subsequently eluted with one column volume of chitin buffer, followed by 20 – 30 mL wash with the same buffer in order to collect residual cleaved protein. All the fractions containing the fusion protein leader-hIAPP were collected and run on SDS-PAGE. In order to regenerate the chitin column, the beads were washed with three column volumes of 0.3 M NaOH and three column volumes of water. The column was then stored in elution buffer with 0.02% sodium azide. Size-exclusion chromatography was used to separate the construct leader-IAPP from the uncut protein and from the intein-CBD product. Soluble protein was loaded onto gel filtration column (HiLoad 16/60 Superdex 75 pg) in gel filtration buffer (20 mM KH2PO4, pH 6.8) and fractions were collected during elution. SDS PAGE and silver staining were used to select the fractions containing pure IAPP. Precast 12% Bis-Tris protein gels for SDS-PAGE (Cat. N. NP0343BOX), NuPAGE MES SDS running buffer (20X) and Pierce silver stain kit (Cat. N. 24612) were purchased from Thermo-Fisher. The final product was then pooled, concentrated and stored at -20°C.

5. Results - Abeta40 and Abeta42

In this project, I investigated the effect of glycation, and its relation to protein aggregation using Abeta40 and Abeta42, the two main species observed in AD patients and IAPP, a peptide intimately associated with hyperglycaemia and T2D.

Abeta peptides were always effectively disaggregated through a sequential treatment with the volatile solvents TFA and HFIP, as suggested by Zagorski et al and extensively reported in the literature (87,172,173). Zagorski et al. presented a sequential treatment with TFA and HFIP to completely disaggregate the synthetic Abeta variants (172). After acid removal by freeze-drying, the pre-treated protein was dissolved in PBS at pH 7.4 in the presence or absence of MGO.

5.1 Aggregation kinetics and glycation reaction optimisation

To understand the contingent effect of glycation on the folding and aggregation properties of Abeta peptides, it was necessary to identify the ideal experimental conditions to follow both the processes, occurring simultaneously, in an independent way. To allow for all possible glycation sites of Abeta (lysine, N-terminus, arginine, histidine) to be potentially available to react with MGO, the aggregation process needed to be sufficiently slow. For this reason, I screened different buffer systems (phosphate buffer concentration, salt concentration) and peptide concentrations (ranging from 5 to 50 μM) and I investigated their effect on glycation reaction speed and protein self-assembly. Optimal conditions were identified using PBS at pH 7.4 (174). The ideal peptide concentration for following aggregation kinetics and glycation reaction within acceptable time-frame was 10 μM.

While aggregation kinetics could be investigated confidently with ThT-binding assay, identifying the glycation products required the employment of analytical techniques. However, it has been reported that the arginine on position five of Abeta peptides readily reacts with MGO to produce the AGE product argpyrimidine, which is an AGE product with spectrofluorometric properties (175-177). The other potential products at the N-terminus or on Lys16, such as CEL and CML, do not have appreciable fluorescence emission (177). For this reason, I decided to study the spectral properties of arginine when incubated with MGO, to verify whether the glycation reaction could be followed by monitoring formation of the fluorescent argpyrimidine. After optimisation, the addition of a 100-fold excess of MGO was shown to be necessary to obtain appreciable glycation. The selected MGO concentration is far from physiological but was employed to accelerate an intrinsically very slow reaction and to follow any effects in an acceptable time interval (178). To investigate the formation of argpyrimidine, the excitation wavelength was set at 340 nm, according to literature, and the emission spectrum was acquired between 360 and 600 nm (179). No significant fluorescence was recorded at time 0 and for the first 2 hours. An increasingly stronger fluorescence signal was detected between 4 and 42 hours with a plateau at 24 hours. The maximum emission wavelength slightly shifted with time from 412 nm to 405 nm (**Fig. 24**). As a control, I also followed the emission of MGO by itself for the same time-frame. No significant fluorescence was observed (**Fig. 24 B**). In addition, to verify that the fluorescence emission spectra of the AGE formation at 405 nm was not affected by the emission spectra of ThT, I incubated 10μM Abeta40 and Abeta42 in the presence and in the absence of 1mM MGO (**Fig. 24 C, D**). ThT was not employed for this assay. The spectra showed none interference was detected.

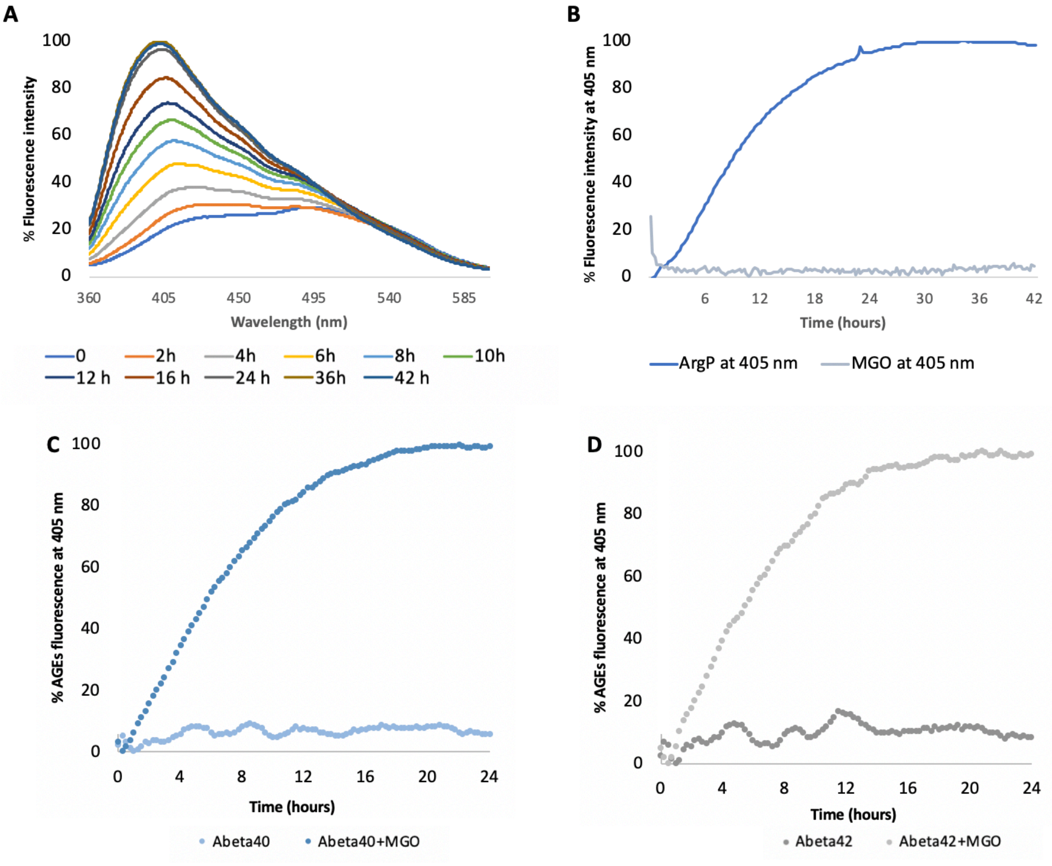

Figure 19. Following glycation of arginine by fluorescence spectroscopy. A. Fluorescence emission spectra of arginine. B. Kinetics of glycation at 405 nm of arginine with amino acid:MGO ratio=1:100 and of MGO. In the kinetics, the variation of the emission fluorescence at 405 nm is proportional to AGEs

formation as a function of time. C and D. Fluorescence intensity of ArgP at 405 nm formed in Abeta 40 and Abeta42 in the presence and in the absence of MGO. This assay was carried out in the absence of ThT. The fluorescence emission spectra of the AGE formation at 405 nm was not affected by ThT.

5.2 Study of the effect of glycation on Abeta40 and Abeta42 kinetics

After pre-treatment with TFA and HFIP, Abeta peptides were dissolved in PBS, divided into two aliquots and incubated with or without increasing amount of MGO at 37 °C. Kinetics of glycation and aggregation were investigated using a multi-well fluorescence plate reader, which allowed me to set multiple excitation and emission wavelengths at the same time. This was crucial to follow the two processes concomitantly on the same sample. I therefore set the excitation at 440 nm and the emission at 485 nm to follow the aggregation kinetics with ThT, and I recorded the argpyrimidine formation by choosing an excitation of 320 nm and an emission of 405 nm.

The fluorescence intensity of argpyrimidine formation on Abeta40 and Abeta42 at 405 nm steadily increased for around 24 hours, when the plateau was reached (**Fig. 25 A, B**), as suggested by the arginine model. For both peptides, the curve describing the glycation process is concave in shape and lacks a lag phase, indicating a reaction that takes place from time 0 and reached its 80% in the first 10 hours.

ThT-associated fluorescence was employed to follow the aggregation kinetics of the Abeta peptides and verify whether the presence of at least one glycated amino acid (Arg5) could alter the speed of the process. The enhanced fluorescence of ThT when bound to amyloid-like structures is commonly used to monitor amyloid formation over time (6).

As reported in the literature, Abeta40 displays slower aggregation kinetics compared to Abeta42 (180,181). Both peptides describe a sigmoidal curve but the lag phase of Abeta40 lasts for around 10 hours, while Abeta42 aggregates faster, with only few minutes of lag phase and with a plateau reached after 12 hours. Abeta40 needs ca. 18 hours to reach the plateau of its aggregation. Also worthy of notice, the glycation of Abeta40 mostly occurs during the lag phase of its aggregation, suggesting that the glycation sites may be better exposed at this stage.

At all tested peptide:MGO ratios of 1:50, 1:100 and 1:200 the kinetics obtained from the glycating peptides showed that glycation slows down the aggregation process of both Abeta40 and Abeta42 (**Fig. 25 C, D)**. The absence of a concentration-dependent effect could be explained by the saturation of glycation sites already at 1:50 ratio. For Abeta40, the presence of MGO further elongates the lag phase of a couple of hours, indicating that the glycation reaction may slow down the first nucleation process and that glycated species may be more conformationally constrained in their monomeric/oligomeric fold (182). Due to the very fast aggregation of Abeta42, a possible effect of glycation on the kinetics of aggregation is hard to estimate. However, glycation seems to limit the total amount or the growth of fibres of Abeta42 to 40% of its maximum, indicating a possible effect on the secondary nucleation (23).

These results corroborated the hypothesis that glycation affects the Abeta peptides aggregation pathway not by completely abolishing the process but by slowing down the formation of either oligomeric or fully-mature aggregates.

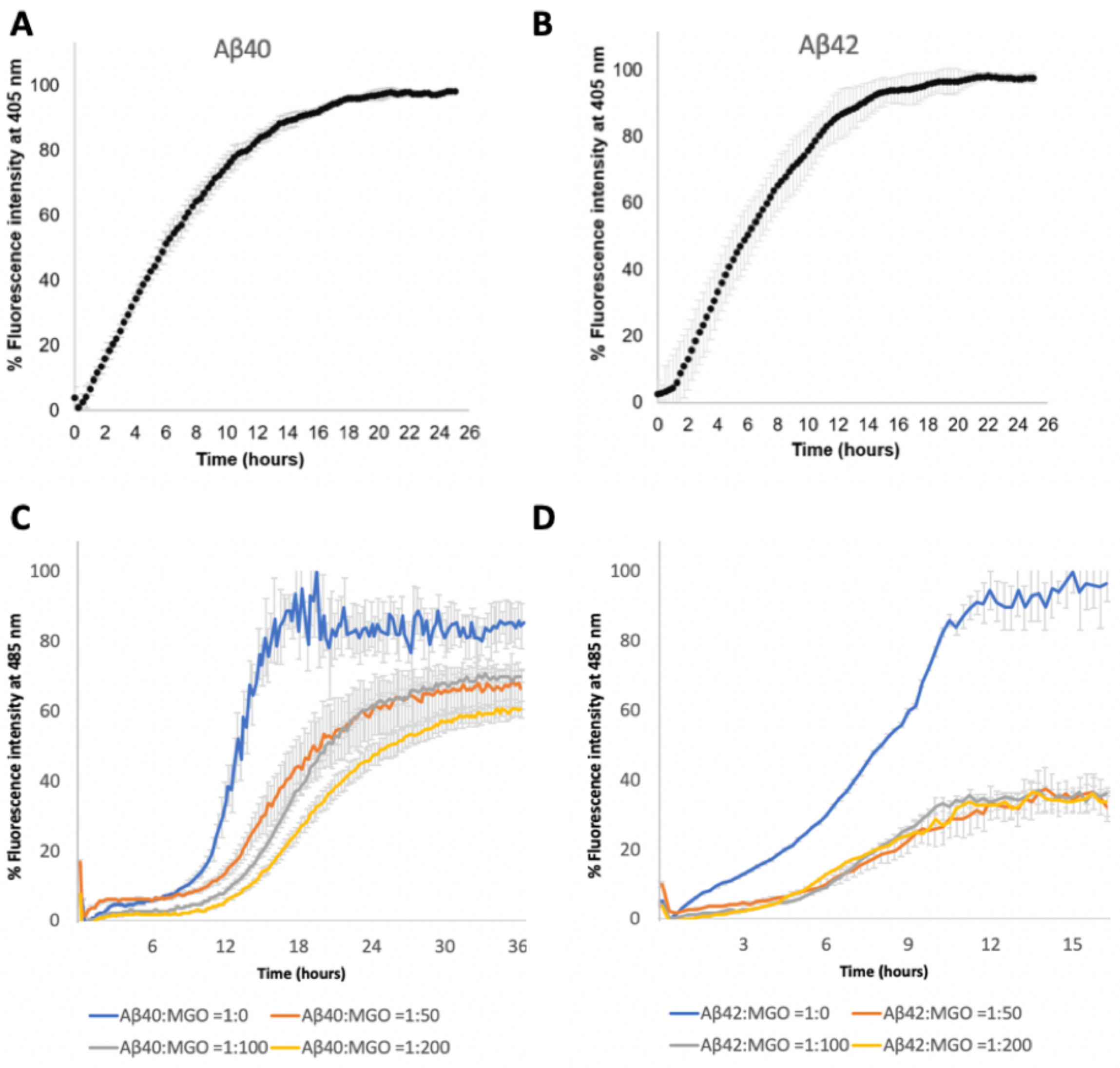

Figure 20. Kinetics of glycation and aggregation for Abeta40 and Abeta42 at 10 µM. A and B. Kinetics of glycation of Abeta with a peptide:MGO ratio of 1:100 for Abeta40 and Abeta42, respectively. The kinetics are represented proportionally to the variation of the emission fluorescence relative to formation of argpyrimidine as a function of time. The fluorescence values were averages of three readings, normalised according to the corresponding blank and expressed as percentage. C and D. Kinetics of fibre formation of Abeta by itself and with an increasing ratio of peptide:MGO ratio for Abeta40 and Abeta42 respectively. The fluorescence values are expressed as percentages and are shown as an average of the three readings.

5.3 Effect of glycation on Abeta secondary structure

The effect of glycation on the secondary structure of the Abeta variants was monitored at different time points by CD spectroscopy, a technique which can provide broad structural information on the secondary structural transitions of proteins. Following optimisation experiments, 50 µM

Abeta40 and Abeta42 were diluted in phosphate buffer (200 mM sodium phosphate) pH 7.4, with or without a 100-fold molar excess of MGO. CD spectra were acquired at 37°C at time zero and after six- and 12-hour incubation. The results of this investigation are reported in figure 26.

CD spectra at different time points showed different degrees of ellipticity, but all peptides showed an initial pure random coil for Abeta40 and a mixture of beta-sheet and random coil conformation for Abeta42 at time 0. Abeta42, though, exhibits a higher beta-sheet content than Abeta40 at t0, a behaviour in agreement with the higher tendency of the longer peptide to aggregate faster (180). Abeta 40 and Abeta42 displayed a similar pattern, transitioning from a more random coil conformation to a richer in amount of beta-sheet structure already after six-hour incubation.

Already after six hours, both Abeta variants displayed a CD profile typical of a purely beta-sheet peptide, with a negative band at 218 nm, but characterised by different degrees of ellipticity. The difference in terms of signal intensity could be explained by a higher degree of protein precipitation in Abeta42 sample, leading to a decrease of protein concentration in solution. In the presence of MGO, Abeta40 did not display an obvious conformational change: the CD spectrum obtained at t0 described a random coil conformation, where the minimum at 218 nm is almost absent. A slight curvature in the region between 215 nm and 220 nm can be observed after six hours, and this signal, probably reporting on an increment in beta content, is more pronounced after 12 hours incubation.

Glycated Abeta variants showed a conspicuous amount of white flocculus precipitate visible at the naked eye at the bottom of the cuvette, suggesting a loss of solubility of the glycates species compared to the non-glycated (data not shown). This could be due to the formation of heavier aggregates or to the presence of MGO in the solution (data not shown). Nevertheless, glycated Abeta40 never seems to fully lose its low-wavelength minimum associated with random coil. Abeta42, in the presence of MGO, showed a similar conformational transition to beta sheet as Abeta40, starting from a mixture of beta-sheet and random coil conformation. After six-hour incubation a very broad minimum in the beta-sheet region of 218 nm was the recognisable contribution of the transition from random coil to beta sheet. Full 12 hours had to pass before a complete transition towards beta sheet could be observed.

CD spectra collected in the presence of 100-fold MGO showed that the Abeta conformational transition from random coil towards beta sheet-rich structures is delayed in both variants. In

Abeta40 the conformational transition delay is more pronounced than Abeta42, but this could be due to the slower aggregation process that Abeta40 undergoes (180). The higher aggregation propensity of Abeta42 compared to Abeta40 was also confirmed by ThT-binding assay in figure 25.

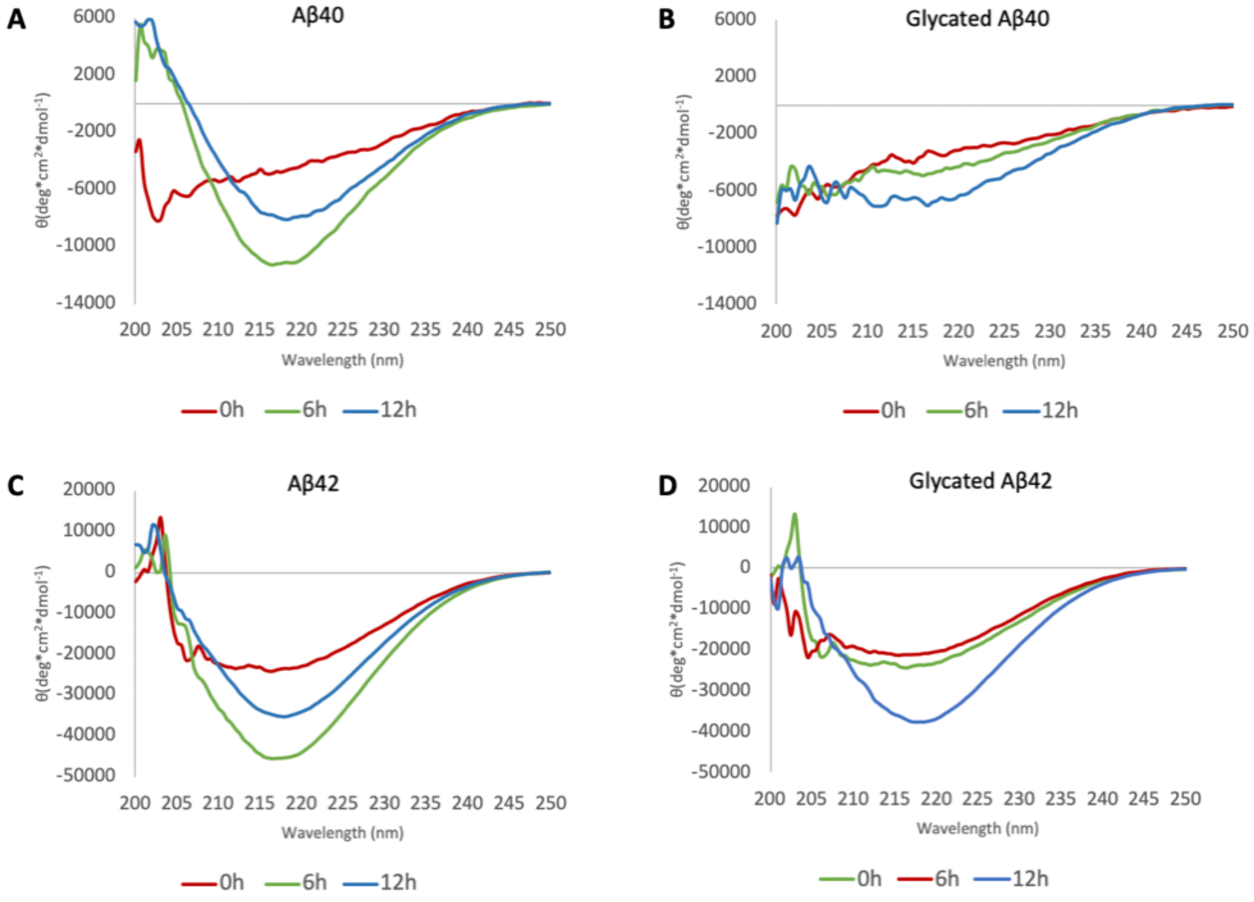

Figure 21. CD spectra of the Abeta peptides in the presence and in the absence of MGO collected at different incubation time at a peptide concentration of 50 µM. Time 0 is displayed in red, six-hour incubation at 37° C in green, 12-hour incubation at 37° C in blue. DMSO was not employed. A. Abeta40, in the absence of MGO, the transition from random coil to beta sheet of Abeta40 during the fibrillation process is displayed. B. Abeta40 with a 100-fold molar excess of MGO. Its native random coil conformation is preserved over time. C. Abeta42, in the absence of MGO, showed a transition from mixture of beta sheet and random coil to pure beta-sheet conformation. D. Abeta42 with a 100-fold molar excess of MGO, its transition from random coil to beta sheet during the fibrillation process is displayed. The transition time is longer in the presence of MGO. Data expressed in ellipticity.

5.4 Identification of Abeta peptides glycation sites by mass spectrometry

Spectrofluorometric techniques allowed me to confirm the occurrence of the glycation product argpyrimidine when Abeta40 and Abeta42 were incubated with excess of MGO. Nevertheless, as previously described, this is only one of the possible AGEs deriving from the glycation of these peptides. I therefore decided to identify all reaction products by MALDI/MS. MGO-glycation sites were identified on Abeta40 by Fica-Contreras et al. They demonstrated Lys16 was glycated four times faster than Arg5 (175). Since they identified the MGO glycation products on Abeta40 I focused primarily on comparing these published results with the ones I obtained for Abeta42.

After incubation of Abeta42 with MGO in phosphate buffer without additional salt (which would have interfered with the ionisation), three main species were observed, in addition to the unreacted peptide (**Table 2**). Note that the difference of one mass unit between the m/z values mentioned and the ones shown in figure 3 is due to the isotopic pattern: peaks related to ions with the same chemical formula can contain different isotopes and their particular pattern is associated with the relative abundance of the isotopes. The signal at m/z 4514.4 was associated to the unmodified peptide (**Fig. 27 A,** top), which has a theoretical molecular weight of 4514.1, and the signals at m/z 4586.5, 4594.5 and 4666.6 (**Fig. 27 A** bottom) confirm that glycation occurred. The ion at m/z 4586.5 was due to a mass increment of 72 Da; this ion could report on the formation of two possible species, arising from glycation at either the N-terminus amino group or at one of the two lysine side chains to form CEL (175,183). The formation of argpyrimidine from the glycation of Arg5 is demonstrated by the ion at m/z 4594.5 (mass increment of 81 Da). Furthermore, a minor species was detected (m/z 4664.6) whose mass exceeds that of free Abeta42 by 152 Da. This indicated the addition of MGO to both a lysine residue with the formation of CEL (mass increment of 72 Da) and to the arginine with the formation of argpyrimidine (mass increment of 81 Da). The additional peak detected in the non-glycated Abeta42 (m/z 4425.4) was tentatively assigned to the fragment 1–41, produced during the MS analysis by the laser-induced elimination of the C-terminal alanine residue.

To identify the exact glycation sites, it was necessary to subject glycated Abeta to trypsin digestion in order to generate smaller fragments, each including a single modifiable site (**Fig. 28**). Liquid chromatographic separation of the digestion products allowed to isolate the different species formed after glycation reaction, for subsequent MS analysis. Fragments obtained by enzymatic digestion were analysed by high-resolution LC-MS. Species of seven different molecular weights were detected (**Table 4**), four of which corresponding to portions of digested non-glycated Abeta42, demonstrating efficiency of digestion. The other three major ions were described with a molecular weight of 2033.903, 2714.259, and 3412.644. They corresponded to the glycated residues 1–16 with an argpyrimidine on position 5 (theoretical weight 2033.894, triply charged ion at m/z 678.968); to the fragment 6–28 with a CEL on either position 16 or 28 (theoretical weight 2714.314, triply charged ion at m/z 905.786); and to the fragment 1–28 with both modifications at Arg5 and Lys16 (theoretical weight 3412.634, quadruply charged ion at m/z 854.181) (**Fig. 27 B**). The presence of all four different species (unmodified peptide, double glycated peptide, glycated peptide on lysine and on arginine residue) suggests an equal reactivity of the two glycation sites demonstrates that there is no interference of the formation of one product on the other.

To identify which of the two lysine residues was indeed glycated, I considered that the protease trypsin would have not been able to cut right after the Lys28 if this residue was modified. I therefore deduced that Lys16 was hosting the glycation product. These results demonstrated that, in addition to the formation of the argpyrimidine that could be followed by fluorescence increment, also Lys16 was glycated by MGO under these experimental conditions.

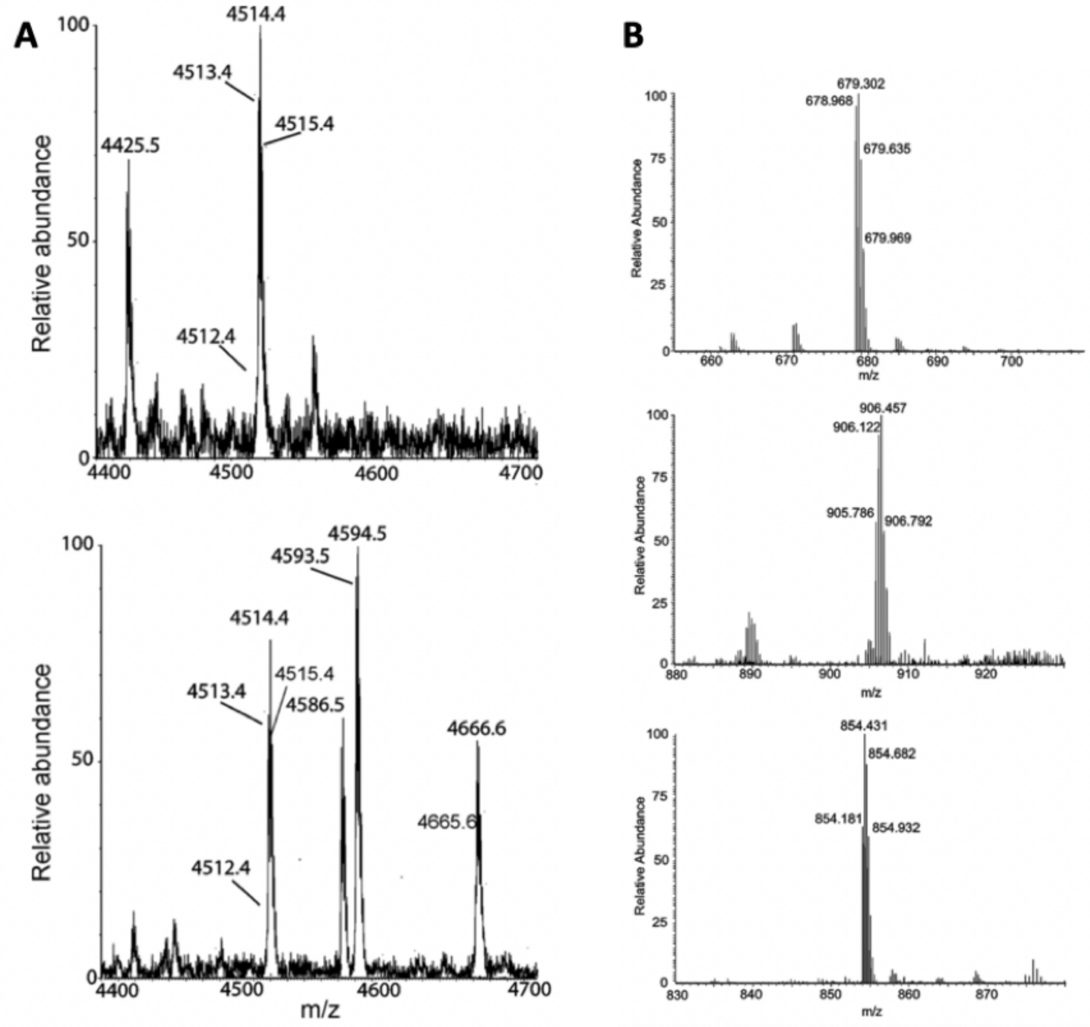

Figure 22. MALDI/MS analysis of glycated and non-glycated Abeta42. A. spectra of Abeta42 (top) and glycated Abeta42 (bottom). Different species observed in the spectra were identified on the basis of their molecular weight (Table 1). B. High-resolution ESI spectra of tryptic fragments of glycated Abeta42. Triply-charged ion at m/z 678.968 (top) was generated by the fragment 1–16 carrying one argpyrimidine residue (theoretical molecular weight 2033.894). Triply-charged ion at m/z 905.786 (middle) corresponds to the fragment 6 –28 with one N-(carboxyethyl)-lysine (N-CEL) (theoretical molecular weight 2714.314). Quadruply-charged ion at m/z 854.181 (bottom) corresponds to the fragment 1–28 carrying both modifications. The difference of one mass unit between the values cited here and the figure are due to the isotopic pattern.

Table 2. List of the main fragments of the trypsin-digested Abeta42 fragments identified by MALDI/MS analysis and their molecular mass. The difference of 1 mass unit between the values cited here and the figure is due to the isotopic pattern.

Ion (m/z)	Peptide	Experimental MW	Theoretical MW
4425.5	1-41 Laser- induced fragment	-	-
4512.4	1-42	4514.4	4511.3
4584.5	1-42 [N-CEL]	4583.5	4583.3
4592.5	1-42 [ArgP]	4591.5	4591.4
4664.6	1-42 [ArgP – N-CEL]	4663.6	4663.4

Table 3. High-resolution MS analysis of the digestion products obtained by trypsin-catalysed hydrolysis of glycated or non-glycated Abeta42.

Ion (m/z)	Peptide	Experimental MW	Theoretical MW	Corresponding peptide
637.298	1-5	636.291	636.287	Unmodified
668.810	6-16	1335.604	1335.596	Unmodified
663.348	17-28	1324.680	1324.666	Unmodified
635.386	29-42	1268.756	1268.753	Unmodified
679.302	1-16 [ArgP]	2039.906	2037.03	Glycated
905.786	6-28 [CEL]	2714.335	2714.314	Glycated
854.181	1-28 [ArgP+CEL]	3412.700	3412.675	Glycated

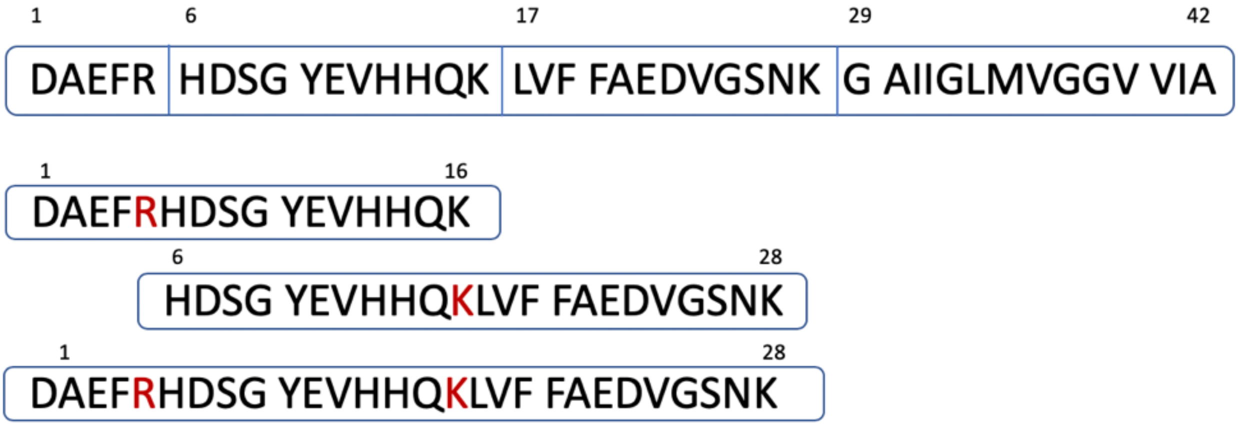

Figure 23. Abeta42 sequence segments produced for MS analysis. On the top the full-length sequence is displayed. The segments produced by trypsin digestion are 1-5, 6-16, 17-28, 29.42, 1-16, 6-28, 1-28. In red, amino acids identified as glycated.

5.5 Analysis of the aggregate morphology of Abeta

AFM was employed for the three-dimensional analysis of the Abeta40 and Abeta42 aggregates to study the effect of glycation on the morphology of the aggregates compared to the non-glycated forms. To obtain representative results, the assay was replicated three times each time acquiring up to ten images. The reported micrographs are representative of the species found.

Abeta40 and Abeta42 were treated as for the ThT-binding assays and incubated for 24 hours at 37 °C. The most abundant species identified for Abeta40 were amorphous oligomers of ca. 100 nm. A few twisted fibres of variable length were also detected. These fibres had a height of 5.4–8.2 nm and a diameter of 8–12 nm, depending on the helix pitch (**Fig. 29 A**, left panel). At the same time point and concentration, the glycated Abeta40 mostly formed multimers of similar shape and size of the ones formed by the non-glycated version, although they appear to be fewer. The longest of these oligomers were defined by a height of ca. 4.9 nm (**Fig. 29 A**, right). No fibre was identified.

After 3 days of incubation, when both aggregation kinetics and glycation reaction are expected to be completed, the length of the twisted fibres formed by Abeta40 increased considerably (up to 2.5 µm, taking into account fibre bending). The helix pitch was always constant and of 70 nm (**Fig. 29 B and G,** left) and the fibre diameter varied between 8.5 nm and 15.7 nm. At the same time point, glycated Abeta40 multimers developed into sporadic fibres with a similar morphology compared to Abeta40 but with a smaller helical pitch (35 nm) and height (6.2-8.5 nm) (**Fig. 29 B and G**, right), indicating a possible different sterical arrangement of the beta sheets.

At 7-day incubation time, the fibres of Abeta40 were found piled up together to give rope-like aggregates measuring 10–15 nm. Few single, long fibres still persisted but their number greatly decreased (**Fig. 29 C**, left). Glycated Abeta40 showed an increase in the number of fibres, but most of them were much shorter that the ones formed by Abeta40 and of constant diameter (11.8–13.2 nm). A few, longer fibres were found (**Fig. 29 C,** right).

In summary, glycation did not seem to substantially affect the morphology of the fibres formed by Abeta40. However, it seemed to reduce the amount of aggregates detected by AFM and the kinetics of their formation.

A similar pattern was identified for Abeta42. Despite Abeta42 samples might look overall less aggregated at all considered time points, this phenomenon could be due to its precipitation. At day-1 of incubation, Abeta42 aggregated as short and thick fibrils with a wide range of diameters and ca. 14.2 nm heights (**Fig. 29 D**, left). At the same time point, the glycated Abeta42 mostly formed oligomers and only few rare larger aggregates, characterised by a smaller size (4.9 nm height and 15.0-nm diameter), were identified (**Fig. 29 D**, right).

After 3 days at 37 °C, Abeta42 exhibited thick and twisted amyloid-like fibres of 0.8–1.6 µm in length, 9–15 nm in diameters, and 5.3–8.7 nm in height, depending on the helical pitch (**Fig. 29 E and I**, left). The helix pitch appeared to be constant but difficult to measure (65–120 nm), due to a significantly relaxed twist. At the same incubation time, the glycated counterpart formed fibrils of similar diameter (16 nm) but with a significantly reduced height (1.6 nm) and length (**Fig. 29 E and I**, right).

At 7-day incubation, both non-glycated and glycated Abeta42 formed the same kind of amyloids that they produced at day 3, indicating that the aggregation process was already fully completed. The fibres formed by Abeta42 were twisted, 70–125 nm long (5.2-nm height, 14.9-nm diameter) and 17.1 nm thick; the ones derived from glycated Abeta42 not only were much shorter (**Fig. 29 F**, left and right, respectively) but also less defined in shape, looking more amorphous. These results demonstrated that, in the case of Abete42, the structural impact of glycation on the morphology of the aggregates was much greater, influencing both shape and size of the aggregates.

Overall, the glycated variants showed thinner and shorter fibres compared to the non-glycated ones at the same time point for both Abeta40 and Abeta42. These results thus demonstrated that glycation heavily affected the aggregation process both by slowing it down and partially also by changing the morphology of the fibres.

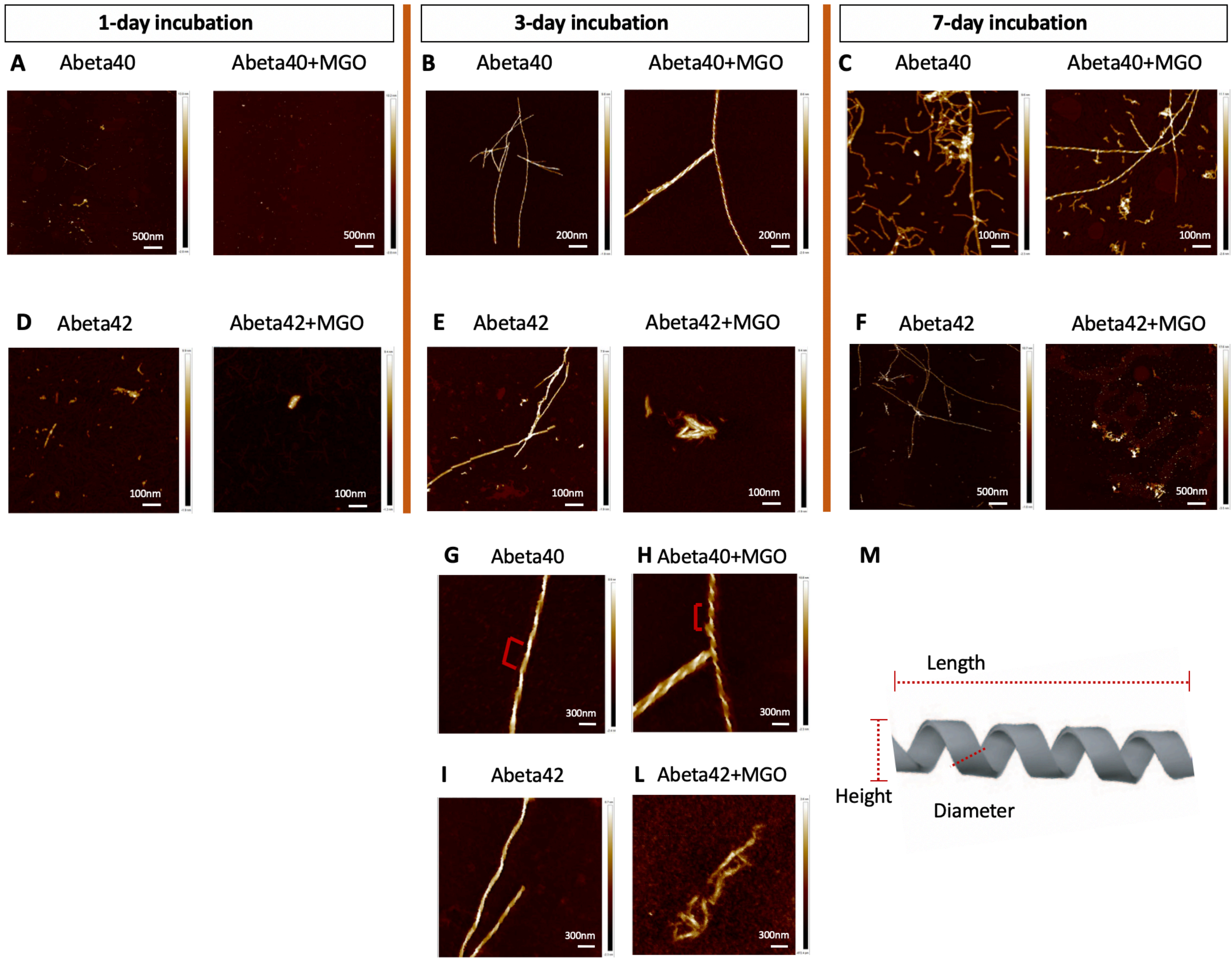

Figure 24. AFM micrographs of Abeta40 and Abeta42 aggregates in the presence and the absence of MGO. The images show that the glycation interferes with the aggregation process either by limiting the growth of the fibres or possibly slowing down the aggregation kinetics. A, B and C. Abeta40 and glycated Abeta40 images acquired with a magnification of 5, 2 and 1 µm at day 1, 3 and 7 respectively. D, E. F. Abeta42NG and glycated Abeta42 images acquired with a magnification of 1 and 5 µm at day 1, 3 and 7. G and H Abeta40 and glycated Abeta40 images acquired with a magnification of 3 µm at day 3, respectively. Helix pitch is indicated in red. I and L. Abeta42 and glycated Abeta42 images acquired with a magnification of 3 µm at day 3, respectively. M. Schematic representation of height, length and diameter on a helical structure.

Table 4. Measurements of Abeta40 and glycated Abeta40 fibres obtained by AFM. Height and diameter are shown at different incubation time (1, 3 and 7 days).

	Abeta40		**Glycated Abeta40**	
Incubation time	**Height**	**Diameter**	**Height**	**Diameter**
1 day	5.4 – 8.2 nm	8.0 – 12.0 nm	4.9 nm	N.d.
3 days	5.1 – 9.6 nm	8.5 – 15.7 nm	6.2 - 8.5 nm	8-16 nm
7 days	4.0 – 6.0 nm	10.0 - 15.0 nm	6.7 - 9.2 nm	11.8-13.2 nm

Table 5. Measurements of Abeta40 and glycated Abeta40 fibres obtained by AFM. Height and diameter are shown at different incubation time (1, 3 and 7 days).

	Abeta42		**Glycated Abeta42**	
Incubation time	**Height**	**Diameter**	**Height**	**Diameter**
1 day	14.2 nm	N.d.	4.9 nm	15.0 nm
3 day	5.3 - 8.7 nm	9-15 nm	1.6 nm	16.0 nm
7 day	5.2 nm	14.9 nm	17.1nm	-N.d.

6. Results – IAPP

At this point of my project, I studied the role of glycation, a pathological process highly relevant in diabetes patients, on the structure, aggregation pathway and toxicity of IAPP. Originally, I had planned to produce the IAPP peptide using a heterologous protein expression system in *Escherichia coli* (*E. coli*). I attempted protein expression and purification experiments with both rat and human IAPP orthologue forms. I initially tested the expression and purification of the rat orthologue since this was described in the literature as much less aggregation prone than the human one.

6.1 IAPP purification

Both rat and human IAPP were initially expressed as a fusion protein in the form leader-IAPP-intein-CBD (sequence in appendix 2), where CBD stays for chitin-binding domain (**Fig. 30**). The N-terminal leader sequence [MKIEEG(NAP)3E] contained codons that are highly expressed in *E.coli* (MKIEGG) and a bulky, hydrophobic group (NANP repeats) that were used to increase solubility and expression of the peptide. The intein and the chitin-binding domain (CBD) acted as affinity tags and generated C-terminal amidation. When a CBD-tagged protein is loaded into the chitin column, it is captured by the resin and separated from other impurities. The addition of a buffer containing ammonium (intein cleavage buffer) cleaves the tag and releases the pure protein.

Cottingham *et al*. demonstrated that ammonium bicarbonate in the intein cleavage buffer played the nucleophilic role by attacking the carbonilic group at the C-terminal (**Fig. 30 E**) (111). Ammonium bicarbonate is the key compound resulting in amide substitution at the cleavage point. The remarkable relevance of this method is obtaining the purified protein with the C-terminal amidation, which is necessary for protein function (109). The presence of an amide group instead of a free acid at the end of the C-terminus can induce significant differences in protein properties, including the mechanism of aggregation, cytotoxicity and the morphology of amyloid fibrils (108).

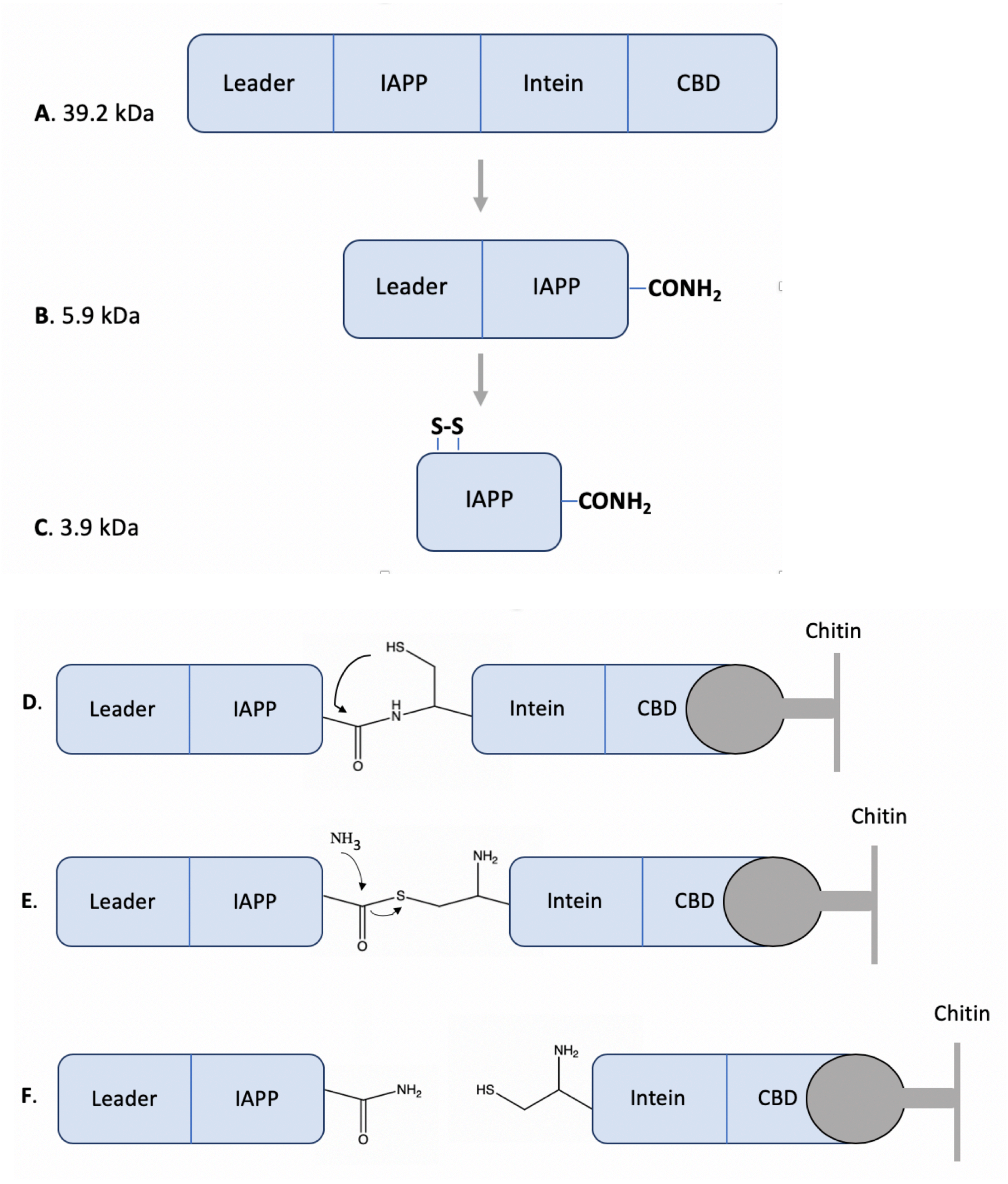

Figure 25. Scheme for expression and purification of IAPP. A. The IAPP construct was expressed in E. coli cells and loaded onto a chitin column. B. C-terminally amidated IAPP with attached N-terminal leader sequence was washed from the column after intein cleavage. C. Wild-type IAPP was generated after disulphide oxidation and V8 protease cleavage. D. Nitrogen-sulfur acyl-shift. E. Ammonium addition leading to ammonium mediated cleavage. F. C-terminal amidation reaction.

After intein cleavage, leader-IAPP-NH_2 was purified by gel-filtration chromatography, which separates the desired product from a mixture according to the size and removes excess of salt and DTT from the buffer. The removal of DTT is important to allow for the formation of the naturally occurring disulphide bond between the two cysteine residues of IAPP. The N-terminal leader sequence was removed using V8 protease. V8 protease typically cleaves polypeptide chains downstream glutamate residues (184). The only glutamate residue present in our construct of

IAPP is located in the last position of the leader sequence. Therefore, cleavage with V8 protease releases the leader sequence yielding native IAPP. This protocol was a valuable aspect of this method as enable to preserve the C-terminus amidation and also the disulphide bridge between Cys2 and Cys7, two features results of two post-translational modifications, both necessary for full biological activity (110).

6.1.1 rIAPP purification

Intein self-splicing was successful, leading to cleavage of ~70% of the fusion construct (SDS-PAGE **Fig. 31 A**). The protein obtained (leader-rIAPP-NH_2) was analysed by size-exclusion chromatography using a Superdex 75 column (120 mL bed volume) to assess whether it was monodispersed in solution. Leader-rIAPP-NH_2 eluted at 83 mL according to the chromatogram reported in **Fig. 31 B**. This elution volume was consistent with the expected molecular weight (5.9 kDa) of leader-rIAPP according to a calibration performed using protein standards. The separation was followed by measuring the absorbance at 280 nm and the fractions corresponding to rIAPP were combined and concentrated. Protein concentration was estimated using the Bradford assay. The final product of leader-rIAPP was highly pure, as assessed by SDS-PAGE. However, the purified protein appeared barely visible on SDS-PAGE suggesting very low yields. For this reason, the purity of the peptide was checked by silver staining (**Fig. 31 A**).

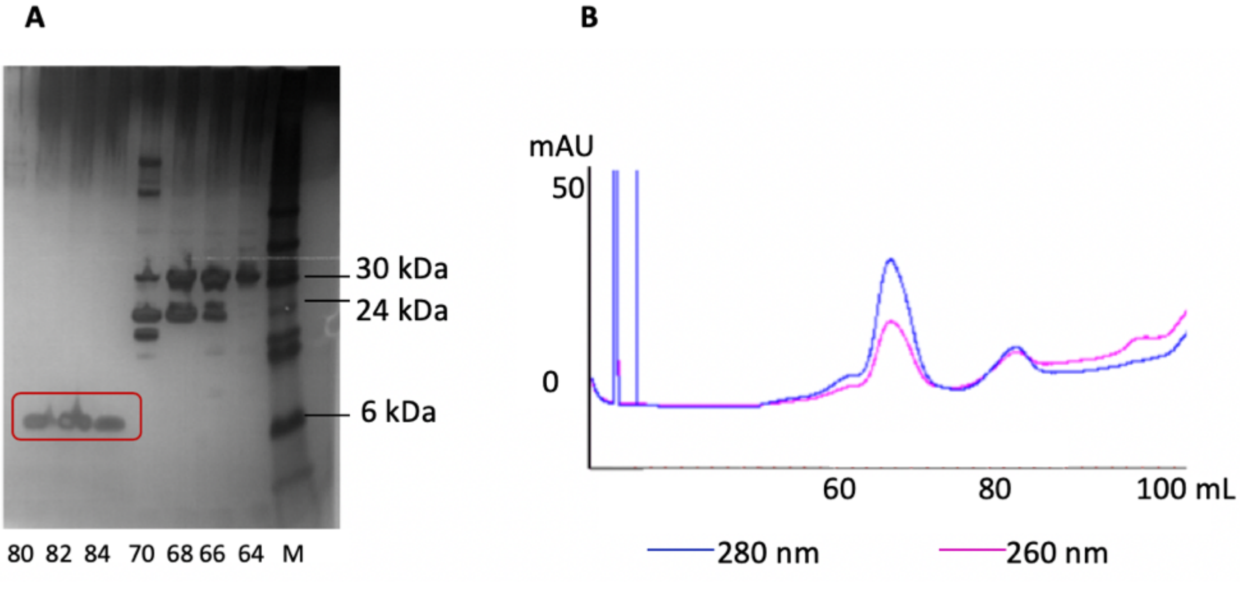

Figure 26. rIAPP purification. A. Peak fractions of gel-filtration (from 64 to 84 mL) were analysed by SDS-PAGE and silver staining. rIAPP bands are circled in red. B. rIAPP (HiLoad 16/60 Superdex 75); rIAPP eluted a single peak at 83 mL.

6.1.2 hIAPP purification

The human orthologue of IAPP was purified using a protocol similar to the one employed for rIAPP (intein cleavage followed by size-exclusion chromatography to obtain the construct leader-hIAPP-NH_2). The gel filtration was performed using a Superdex 75 column (120 ml bed volume). Leader-hIAPP-NH_2 eluted at 88 mL (**Fig. 32 B**). This elution volume is consistent with the expected molecular weight (5.9 kDa) of leader-hIAPP according to a calibration performed using protein standards. The purity of fractions selected from the gel filtration profile was verified by SDS-PAGE and silver staining (**Fig. 32 A**). Pure leader-hIAPP was found in fractions eluted at volumes comprised between 86 and 90 mL.

The yield obtained from both rat and human was very low, and the samples were not suitable for my analysis. For this reason, made strong by the experience gained with Abeta, I ordered the synthetic full-length IAPP peptide (1-37) from two different companies: Peptide2.0 and Eurogentec. The peptides arrived lyophilised and were stored at -20°C until use. All the peptides contained physiological modifications, such as the C-terminal amidation and the 2-7 disulfide bridge as determined by mass spectrometry and reverse-phase HPLC. The peptide coming from Peptide 2.0 Inc was obtained with 98.43% declared purity while that from Eurogentec with 95% declared purity.

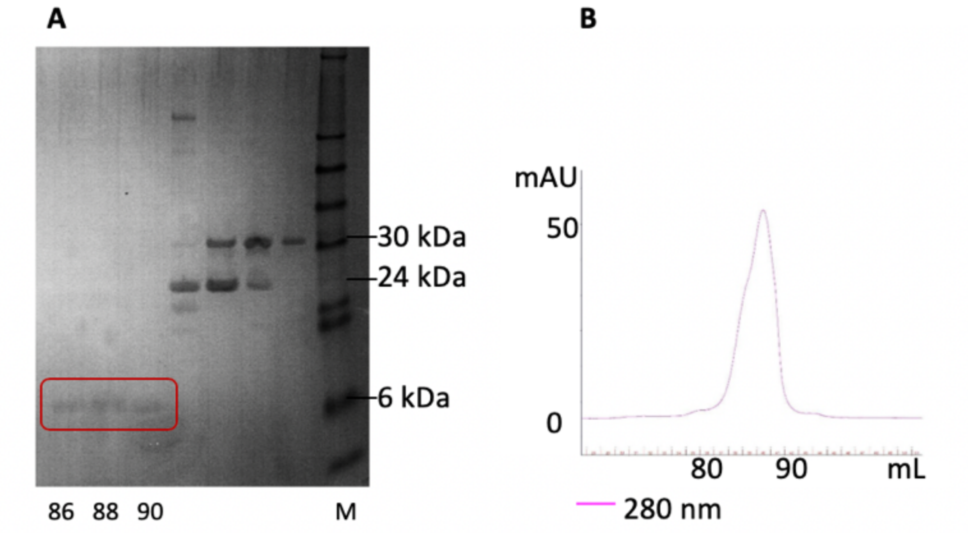

Figure 27. hIAPP purification. A. Peak fractions of gel-filtration (from 86 to 90 mL) were analysed by SDS-PAGE. hIAPP bands are circled in red. B. hIAPP (HiLoad 16/60 Superdex 75). hIAPP eluted at 88 ml.

6.2 Spectroscopic analysis of MGO

This project was time-wise initiated after completing the one on the Abeta peptides. In the literature, MGO is extensively used in enzymatic studies, and in most all the cases is obtained by steam distillation (185) of a commercial 40% solution in water. The low effective concentrations of MGO in water and the addition of acid compounds should prevent MGO polymerisation (169). When I started my project, I used commercial MGO, purchased from Sigma (cat. n M0252). I assumed that the compound would be pure and stable. I understood with time that this was not the case. I realised that MGO undergoes complex modifications with time especially if not in the presence of suitable quantities of reducing agent.

Since the MGO concentration as compared to the reducing agent and the peptide were very high, I realised that the glycating agent could undergo polymerisation and oxidation in aqueous conditions as previously described by Nemet et al (186). They showed how solvent, temperature, and the amount of available water strongly affected the equilibrium of the different forms of MGO and, therefore, it could radically alter its reactivity. In addition, the effective MGO content in solutions stored for even short time at the suggested storage temperature (4 °C) is questionable at best (169). For these reasons, I concluded that the commercial solution may not be an optimal product to carry out the glycation analysis.

To perform experiments on IAPP, I firstly attempted to carry out distillation of MGO thanks to the help of collaborators in University College of London. After some attempts to distil MGO, the procedure was unfortunately unproductive due to practical reasons. Secondly, another simple, convenient, and reproducible method to obtain pure MGO was adopted. The synthesis of high purity MGO was carried out from methylglyoxal 1,1-dimethyl acetal (hereafter named acetal) in acid conditions at high temperature in phosphate buffer following an the protocol described in material and methods (**Scheme 2**) (169). The acid hydrolysis method is more time consuming, but better reproducible and allows an increased and optimal purity compared to the commercial MGO. The obtained yield was virtually near 100% as established by ^{1}H NMR (**Fig. 33**).

Scheme 2. Acid hydrolysis of acetal resulting in one molecule of MGO and two of methanol.

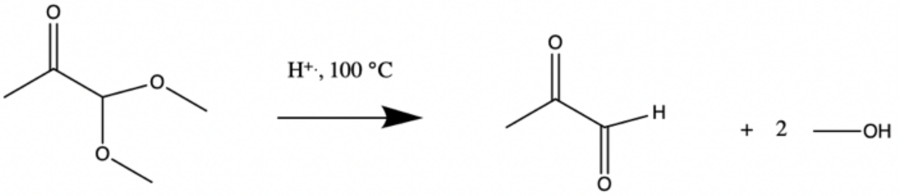

Scheme 3. Behaviour of MGO in acqueous condition. MGO undergoes a spontaneous reaction with water and less than 1% of the MGO has been demostrated to remain unreacted in aqueous solution (141). Two compounds are predominantly formed: methylglyoxal monohydrate and methylglyoxal dihydrate (186).

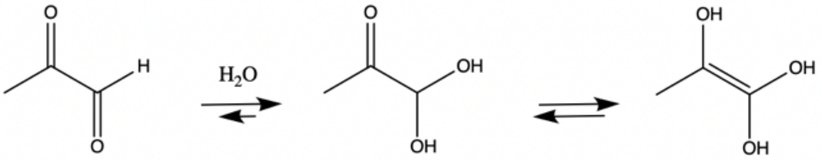

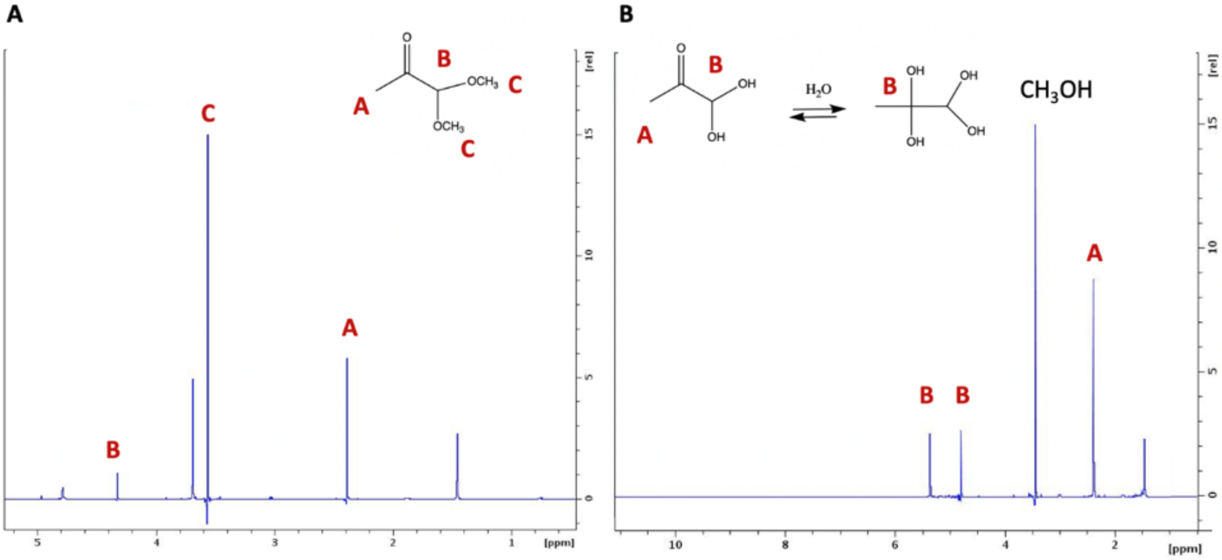

Figure 28. 700 MHz 1H NMR spectra of the reagent acetal and the product MGO with assignment and their chemical structure. A. Time zero of the reaction, δ: 2.18 (s, 3H, CH3), 3.4 (s, 3H, CH3), 4.44 (s, 1H CH). B. Reaction completed, δ: 2.38 (s, 3H, CH3), 5.4 (s,1H, CH), 4.82 (s,1H, CH).

Several resonances in the ^{1}H spectrum can be tentatively assigned by comparison with their predicted chemical shifts. Acetal, the reagent of the reaction (Scifinder CAS registry n 6342-56-9), is characterised by the presence of three main hydrogen types (**Fig. 33 A**): three hydrogens belonging to the methyl group in alpha to the carbonyl group, labelled as A in the figure, in the region of 2.18 ppm; a single hydrogen in alpha to the two oxygens, labelled as B, in the region of 4.44 ppm; two groups of hydrogens part of the methoxyl groups, labelled as C, in the region of 3.4 ppm. A potential impurity was detected at around 1.45 ppm.

At the end of the acid hydrolysis, the reaction product was analysed by means of ^{1}H NMR (**Fig. 33 B**). The reaction produced two molecules of methanol per one of MGO, as expected (**Scheme 1).** The resulting spectrum showed three signals attributable to MGO at 2.38 ppm, at 4.82 ppm and at 5.40 ppm. The first chemical shift was assigned to three hydrogens belonging to the methyl group, present both in the acetal and MGO and labelled as A (**Fig. 33).** The other two signals belong to the single hydrogen less shielded, called B in figure 33.

The presence of two signals for the single hydrogen B is due to a mixture of two MGO forms. MGO undergoes a spontaneous reaction with water and it has been estimated that MGO predominantly forms two compounds: mono- and dihydrate MGO (**Scheme 2**) (186-188). Since around 99% MGO reacts with water, the only hydrogen belonging to the unreacted aldehyde (**Scheme 3,** left) cannot be detected (141).

The signal of methanol was assigned as the resonance at 3.4 ppm as reported in predicted chemical shifts (Scifinder CAS registry n 67-56-1). The impurity found in the acetal (1.45 ppm) was not reactive. I could then conclude that the reaction was successfully completed from the three signals attributable to MGO exactly where predicted i.e. at 2.38 ppm, at 4.82 ppm and at 5.40 ppm. The satisfying outcome was also testified by the absence of any acetal associated signal. As a result, the in-house-synthesised MGO was employed for further glycation experiments on IAPP.

6.3 IAPP sample preparation

To study properly the peptide aggregation process, it was crucial to dissolve any possible pre-existing aggregates to detect the reaction starting from the monomeric form.

IAPP from Peptide2.0 (named IAPP1) was initially treated with HFIP, a strong acid alcohol, as often reported in the literature (189-191). After HFIP removal, the peptide, in the form of a thin film, was dissolved in buffer and analysed with CD to investigate the secondary structure. The treated peptide showed a clear alpha-helix conformation (**Fig. 34),** maybe caused by the interactions of the peptide with traces of the HFIP hydroxyl groups. Surprisingly, the protein produced by Eurogentec (named IAPP2) after the same treatment with HFIP showed a conformation intermediate between random coil and alpha-helix **(Fig. 34)**. The contrasting behaviour of IAPP1 and IAPP2 may derive from a different history determined by different production and/or purification methods.

I therefore judged the HFIP treatment as not successful, since neither samples were suitable for aggregation studies. At this stage, I decided to employ TFA, the strong acid I had previously used for the preparation of Abeta peptides in combination with HFIP. I therefore dissolved IAPP1 in TFA only, before removing it and preparing the solution in buffer. Under these conditions, IAPP1 finally showed an reproducible random coil conformation, reasonable starting point to study the aggregation process **(Fig. 34)**. From now on, IAPP1, the peptide produced by Peptide 2.0, was the only one employed for all experiments and will be from now on referred simply as IAPP. TFA (1 ml/mg peptide) was left for one hour at room temperature before being completely removed by freeze drying. The peptide film, firmly stack on the vial walls, was dissolved in the appropriate buffer by slowly and repeatedly pipetting. The reproducibility of the assay was hard to be obtained also due to the stickiness of the sample which was not easy to be fully resuspended in buffer.

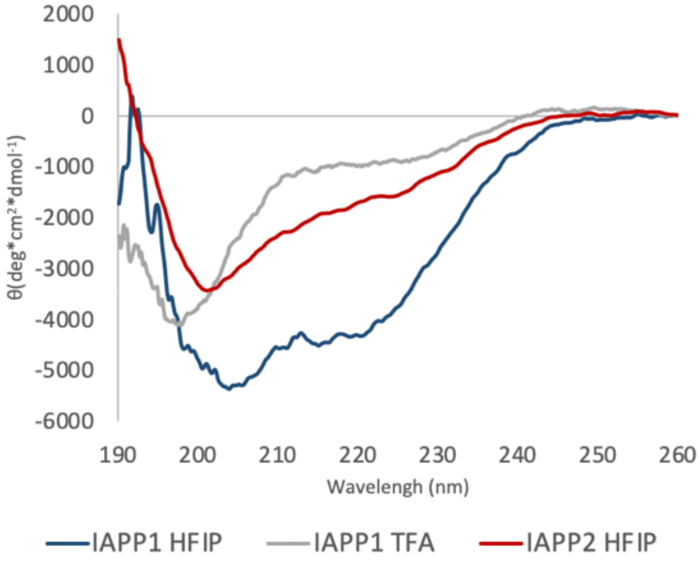

Figure 29. CD Spectra of IAPP from different sources. IAPP1 from Peptide2.0 pre-treated with HFIP (blue line) showed alpha helix conformation, but when treated with TFA (grey line) displayed a random coil conformation. IAPP2 produced by Eurogentec after treatment with HFIP was a mixture of random coil and alpha-helix conformation. Data are expressed in ellipticity. The spectra were recorded immediately after acid pre-treatment. Data are plotted as mean residue molar ellipticity.

6.4 IAPP aggregation studies

As reported for Abeta peptides, ThT-binding assay was employed to follow the aggregation kinetics of IAPP, in the absence or in the presence of increasing concentrations of MGO. The

TFA-dried peptide appeared as a thin film on the walls of the tube. The immediate addition of buffer to this tube may not guarantee its complete resuspension. Part of the protein could stay attached to the walls and the estimation of the protein concentration could be not reliable. To ensure full peptide resuspension I decided to add dimethyl sulfoxide (DMSO) to the peptide layer to obtain a 1 mM stock solution. DMSO is an organic aprotic solvent which could harvest successfully the protein stuck on the tube walls because of its hydrophobic features. In addition, it could help dissociate pre-formed aggregates and promoting its monomeric state. Total DMSO v/v used never exceeded 2%. The protein stock in DMSO was diluted into PBS to reach the desired concentrations and incubated at 37°C.

To identify the ideal peptide concentration which would give me an easy-to-follow aggregation kinetics curve, different concentrations ranging from 5 µM to 50 µM were screened. Optimal conditions were found using 10 µM IAPP. At this peptide concentration the aggregation curve was highly reproducible, the fluorescence was high enough to define a smooth curve but not as intense as to saturate the signal, and the kinetics was sufficiently slow to allow for a well-defined lag phase. The aggregation kinetics of IAPP by itself and in the presence of increasing molar excesses of MGO were studied. Peptide:MGO ratios included 1:0, 1:5, 1:10, 1:20, and 1:100 (**Fig. 35 B)**.

At this concentration, IAPP did not aggregate substantially for the first 10 hours of incubation. The growth phase was stretched for almost 48 hours and full plateau was reached at 72 hours. The addition of any amount of MGO seemed to have reduced the slope of the line described by the elongation phase. If the value 1 is assigned to the slope of the curve for protein:MGO=1:0, by adding 5-molar ratio excess of MGO the slope reduced its value to 0.58, although the total amount of aggregates was reduced of only 10%. Further addition of MGO to gain protein:MGO ratios of 1:10 and to 1:20 showed a proportional effect on the aggregation kinetics. In both cases, the MGO addition did not interfere significantly with the lag phase but substantially with the elongation rate, increasing the relaxation of the slope and confirming a concentration-dependent effect. With protein:MGO ratios 1:10 and 1:20 the slope was reduced to 0.38 and 0.26 and the amount of total aggregates to 70% and 50%, respectively. Finally, the addition of 100-fold molar exces MGO altered dramatically the aggregation process by decreasing the slope of the aggregation curve to a value of 0.32. Under these conditions, despite the plateau was reached after around 48 hours, almost one day earlier than the non-glycated IAPP, the maximum fluorescence intensity was around 70% lower than the non-glycated sample. This may be due to the excess of MGO acting as co-solvent.

To ensure that the kinetics and the quantitative effect of glycation on IAPP aggregation were solely due to MGO and not to DMSO, I defined the IAPP aggregation curve also in the absence of the latter.

The TFA pre-treated peptide film was diluted in PBS to reach a concentration of 60 µM and incubated at 37°C. The concentration was chosen taking into account all possible losses of protein stuck on the tube walls and also to reproduce the conditions used for other assays described below. The peptide solution was pipetted carefully to capture the maximum amount of protein from the tube walls. The kinetics of aggregation was described by a steep sigmoid, with a lag phase of two hours. Between five and six hours the ThT-associated fluorescence emission was at its 90%, reaching the full plateau after around 10 hours (**Fig. 35 A**).

Under these experimental conditions the aggregation of IAPP seemed faster but it was proportionate to the peptide concentration. The shape of the curve described remained the same as before.

Collectively, these results indicated that glycation of IAPP by MGO decreases the rate of fibrillisation in a molar ratio-dependent manner. MGO did not affect the kinetics of formation of a critical nucleus but generally decreases the rate of elongation. In addition, by increasing the amount of MGO added to the protein, the final amount of amyloid-like fibres decreases proportionally.

By comparing the experiments in the presence and in the absence of DMSO it was possible to confirm that glycation affected the aggregation process. By observing the data obtained with DMSO treatment, the effect of MGO on IAPP aggregation is remarkable and the decrease in rate is easily measurable in a molar ratio-dependent manner. On the other hand, it is valuable to follow the proteins' behaviour in the absence of DMSO, which is the same condition adopted in techniques such as NMR and CD.

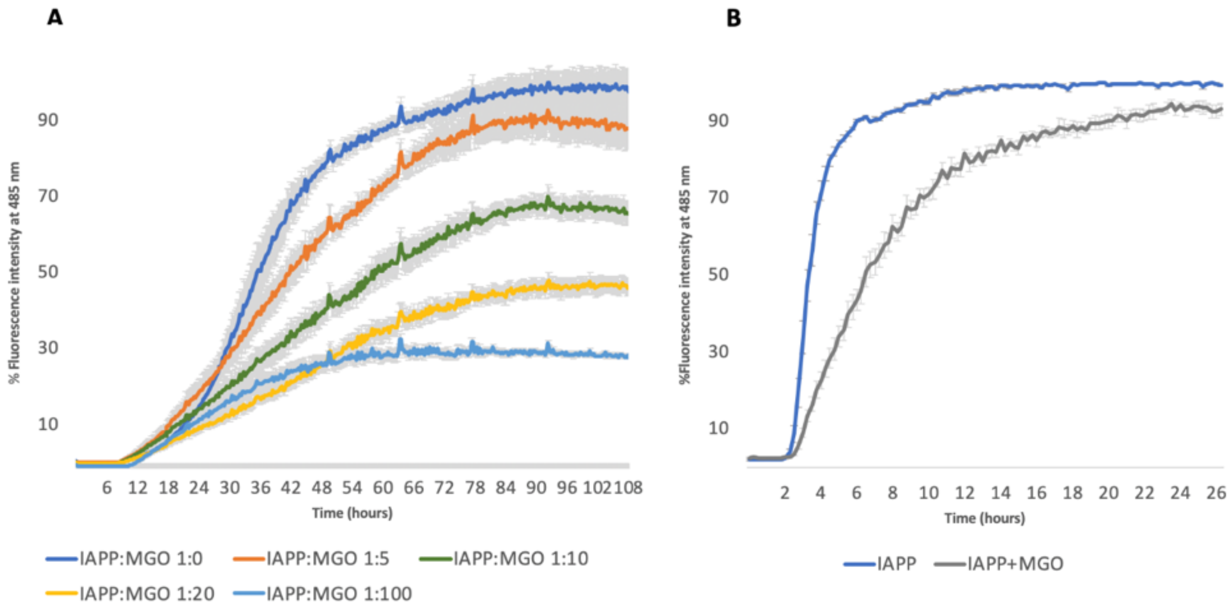

Figure 30. Kinetics of aggregation measured by the variation of the fluorescence signal of ThT. A. IAPP:MGO with 0-fold, 5-fold, 10-fold, 20-fold and 100-fold molar excesses of MGO to IAPP, using 10 µM IAPP concentration from a DMSO stock. Data represented as ThT fluorescence intensity at 485nm and expressed as percentages B. The same experiment shown with 60 µM IAPP concentration and also excess of MGO. DMSO was not employed.

Table 6. Values of the slopes of each ThT curve. Values obtained fitting elongation phase data. The peptide ratio 1:0 was assumed as 100%. The ratio has the function to clarify the text.

IAPP : MGO	Slope	Percentage %	Ratio
1:0	0.6779	100.0	1
1:5	0.3914	57.7	0.58
1:10	0.2573	37.9	0.38
1:20	0.1786	26.3	0.26
1:100	0.2154	31.7	0.32

6.5 Effect of glycation on secondary structure of IAPP

The effect of glycation on the secondary structure of the peptide was monitored by CD spectroscopy. Following optimisation experiments, 60 µM IAPP was diluted in phosphate buffer

(15mM sodium phosphate, 20mM NaCl), pH 7.4 at 37°C with or without a 20-fold molar excess of MGO.

Straight after dissolving IAPP in buffer in the presence and in the absence of MGO, conspicuous precipitation was visible in the cuvette. IAPP at time zero presented/indicated a strong band at ca. <200 nm, characteristic of a high content of random coil structure. A negative shoulder was also distinguishable around 220 nm, suggesting that a mixture of secondary structure characteristics may be present (**Fig. 36 A**). In the two following hours IAPP changed slightly the shape of the described curve. After six-hour incubation at 37°C the signature random coil minimum partially lost its intensity and slightly moved towards higher wavelength (205 nm), suggesting an increment in peptide folding. Instead, the minimum at ca. 220 nm became more pronounced, indicating an enrichment of alpha helix and beta-sheet content. CD spectra collected at several time points showed that fibril formation is accompanied by a conformational transition towards beta sheet-rich structures.

In the presence of MGO, the peptide at time 0 displayed the exact same secondary structure as non-glycated IAPP. With prolonged incubation at 37°C, the glycation reaction seemed to hinder the accumulation of beta-rich structures detectable by this technique (**Fig. 36 B**). The overall signal intensity decreased with time, probably due the precipitation of aggregated peptide.
After incubation at 37°C, the difference in spectra between non-glycated IAPP and glycating IAPP suggested that glycation by MGO interfered with the transition of the secondary structure towards beta sheet. The different degree of precipitation may also suggest a difference in the morphology of the formed aggregates.

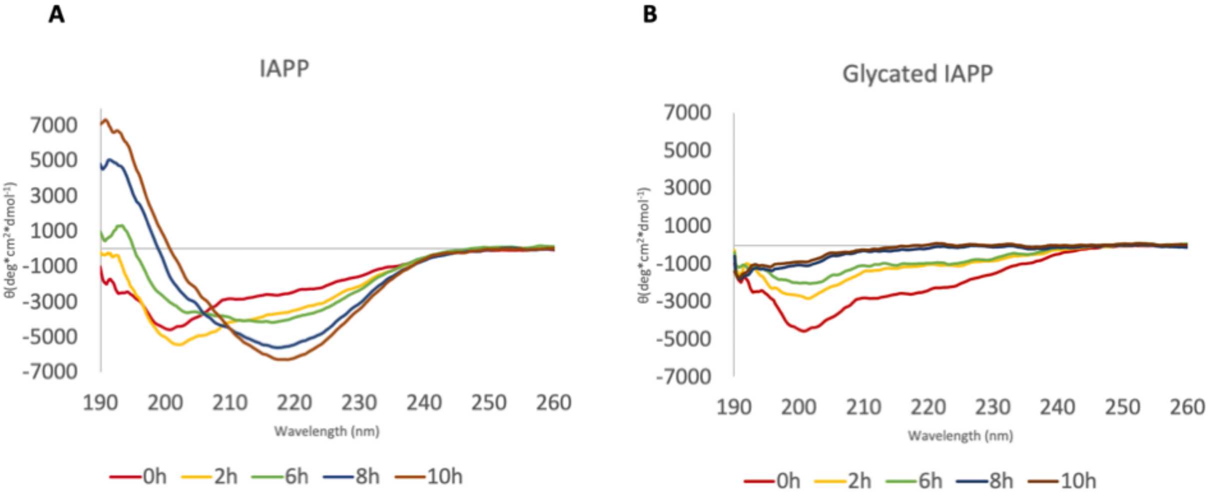

Figure 31. CD spectra of IAPP at 60 μM concentration, in the presence and in the absence of MGO collected at incubation times at 37°C. Time zero is displayed in red, two-hour incubation in yellow, six-hour incubation in green, eight-hour incubation in blue and 10-hour incubation in brown. DMSO was not employed. A. In the absence of MGO, the alpha- to beta- transition of IAPP during the fibrillation process is displayed. B. With a 20-fold molar excess of MGO, IAPP native random coil/alpha helix conformation is preserved over time. Data expressed in ellipticity.

6.6 Evaluation of the effect of glycation on IAPP folding

To sustain the thesis derived from the CD analysis, I employed also NMR, which is a method that can provide high-resolution information regarding the chemical shifts of amino acids at different time points. This technique may not be ideal for aggregating proteins and for my experimental conditions, but it could nevertheless be useful to interpret the results so far obtained.

I started by tentatively reproducing the 2D TOSCY spectrum found in literature for IAPP. The spectrum was therefore acquired at 10 °C, 10 mM sodium phosphate buffer at pH 5.5 (192). The lower pH should help to maintain the peptide stability and thus decrease the rate of aggregation, also increasing the chances of obtaining a clean spectrum. 2D NMR spectra obtained under these conditions revealed a reasonable dispersion of the chemical shifts, as shown in the fingerprint region of IAPP (**Fig. 37 A**, blue). Residue assignments were tentatively carried out and the spectrum was qualitatively recognisable with almost half of the 37 amino acids being assigned. The two residues more significant as possible glycation sites (Lys1, Arg11) did not appear in the spectrum. Moving towards conditions closer to what it has been used so far for the other experiments (37 °C at pH 5.5 and 37 °C at pH 7.4), the effect on the number of recognisable peaks was dramatic (**Fig. 37 B**, green). As well known, small unstructured peptides often have no detectable spectrum at neutral pH, which was also the case in this experiment. For this reason, I decided to screen 1D ^{1}H NMR spectra at 37°C and both pH 7.4 and 5.5, using always 60 µM IAPP in sodium phosphate. I decided to carry out the investigation also at a lower pH since this condition is physiologically relevant: IAPP is stored in the acidic environment of secretory granules of the beta cells (pH 5.5).

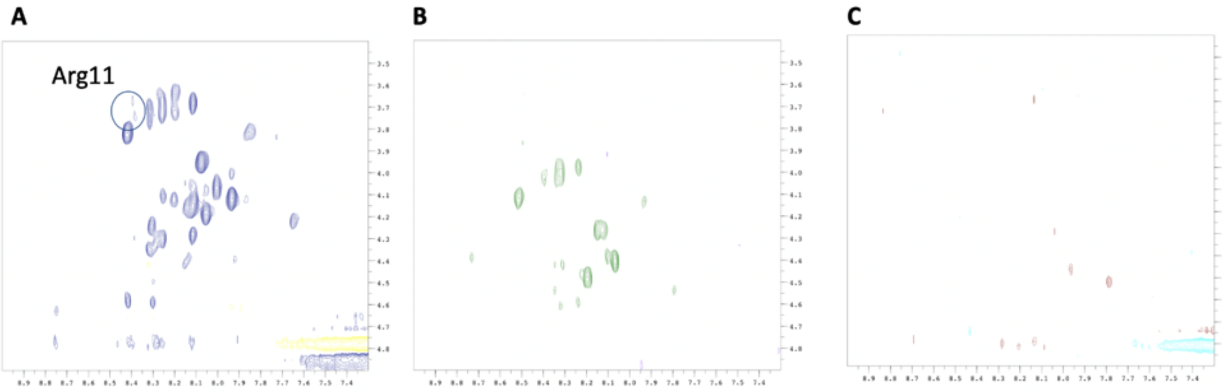

Figure 37. 2D TOCSY spectra of IAPP at 60 µM. A. IAPP at pH 5.5, 10 °C. The fingerprint of the peptide corresponds to literature (192). The position of Arg11 should appear as indicated. B. IAPP at pH 5.5, 37 °C. Temperature has a strong decreasing effect on the shifts and intensity of the spectrum. C. IAPP at pH 7.4, 37 °C. The additive effect of temperature and pH have a dramatic effect on the spectrum, making it very undetectable.

The effect of the pH at 37 °C was also studied obtaining 1D ^{1}H NMR spectra. (**Fig. 38**). The spectrum registered at pH 5.5 confirmed that IAPP was stable and soluble in this condition. This is supported by the fact that IAPP is stored in the acidic (pH 5.5) medium of the secretory granules in the beta-cells, where the protein does not aggregate. In stark contrast, at pH 7.4 IAPP resulted more aggregated and less folded, according to the 1D ^{1}H NMR spectrum (**Fig. 38**). This outcome is in line with the physiological behaviour of IAPP, which is prone to aggregate when released from the vesicles into the blood flow at pH 7.4 (193). Since it is likely that glycation occurs in the extracellular space in a neutral pH, I decided to carry on working at a pH 7.4 to investigate the effect of MGO on IAPP folding. Further 1D ^{1}H NMR studies were carried out in the presence and in the absence of MGO incubated at 37 °C. Spectra were acquired at time zero, after six and 24-hour incubation but the spectra were not suitable for comparison.

In conclusion, Lys1, Arg11, the two residues more likely to be glycation sites, did not appear in the 2D TOCSY spectra obtained at physiological conditions (37 °C, pH 7.4). In both NMR experiments 2D TOCSY and 1D ^{1}H, the neutral pH and the higher temperature dramatically increased the increase of aggregation preventing the possibility to investigate the effect of glycation in physiological conditions. Therefore, the obtained NMR data were inconclusive to describe any clear effect of glycation on IAPP folding.

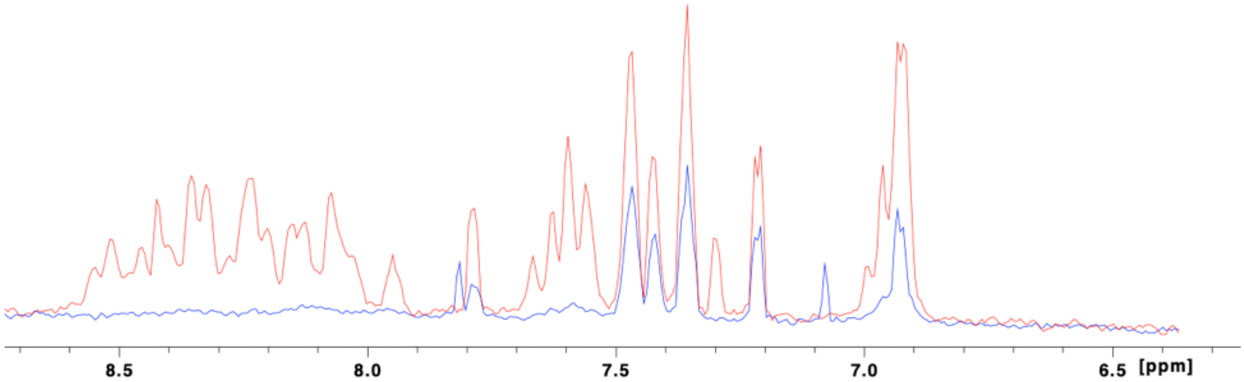

Figure 38. Zoom in the aromatic region (9-6 ppm) of 1D ^{1}H NMR spectra of IAPP at pH 5.5 (red) and at pH 7.4 (blue).

6.7 Identification of IAPP peptides glycation site by mass spectrometry

Protein glycation products can be described by mass spectrometry analysis (194). MGO-glycation reaction could mainly occur on specific functional groups: on the amine functions of lysine residues or of the N-terminal, or on the arginine guanidine group, or on the histidine imidazole side chain. However, adducts obtained with these two reactive sites were different, and should be distinguished on the basis of the observed mass increment. Indeed, modification involving a lysine mainly generated carboxyethyl-lysine (CEL, mass increment 72 Da) and carboxymethyl-lysine (CML, mass increment 58 Da), whereas if the reaction involves an arginine residue the reaction products were hydroimidazolone (mass increment 54 Da) and argpyrimidine (mass increment 80 Da) (48,49,195). In this work, the formation of two modified species was shown, after 48-hour incubation at 37 °C of IAPP with a 10-fold molar excess of MGO. Mass spectrometry analysis of these species revealed molecular weights of 3978,2 (quadruply charged ion at m/z 994,4756 **Fig. 39 C)** and 3964,2 (quadruply charged ion at m/z 990,9697 **Fig. 39 B**), respectively corresponding to a mass increment of 72,032 Da and 58,009 Da in respect of unmodified peptide, (theoretical weight 3906,3, quadruply charged ion at m/z 976.4675 **Fig. 39 A**), thus indicating that glycation reaction involved an amide function. IAPP structure is characterised by only two reactive amine groups: the protein N-terminal and the ε-amine group of Lys1. Since the two groups are located on the same amino acid, it was not possible to define which of the two was the actual modification site by mass spectrometry, even performing a MS/MS experiment. However, it was demonstrated that glycation occurred on the free amino acid group belonging to Lys1 or to N-terminus, leading to the formation of CEL and CML.

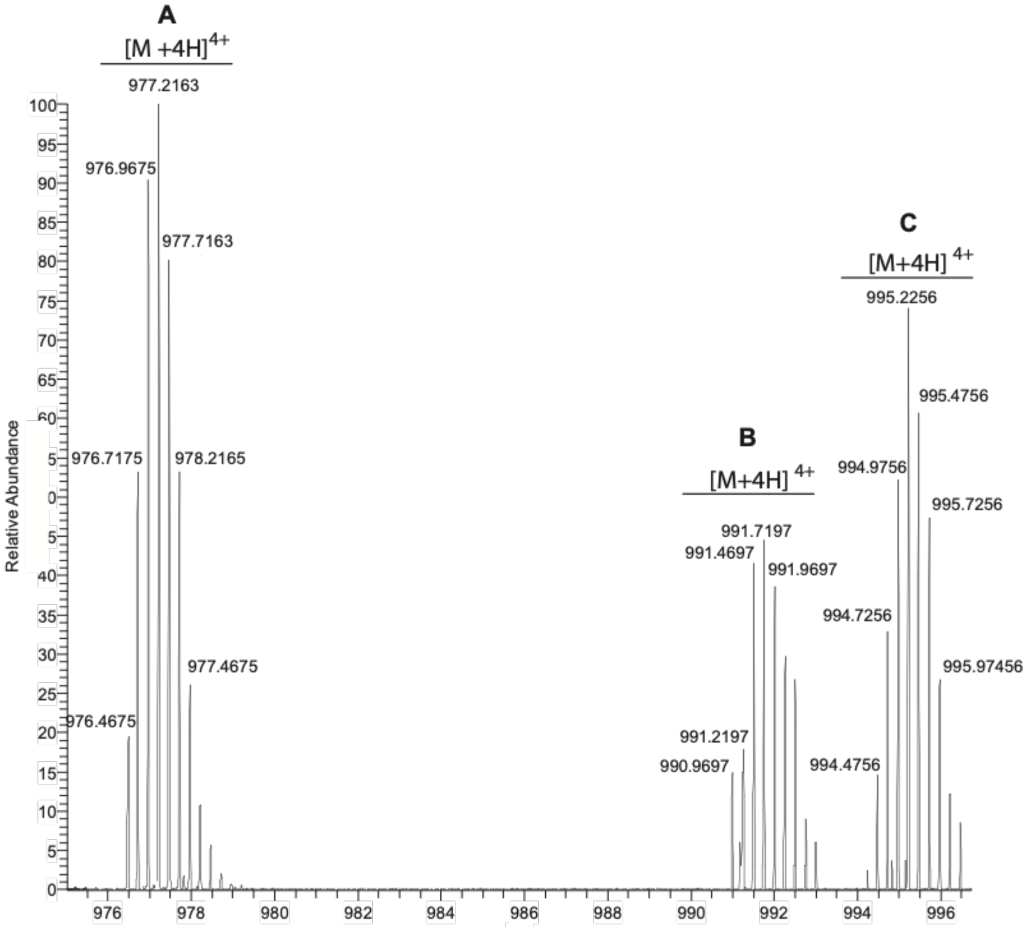

Figure 39. ESI-MS spectrum of IAPP species resulting from the 48-hour incubation of the peptide with a 10-fold molar excess of MGO at 37 °C. Three compounds were detected: unmodified IAPP (species A) whose [M+4H]4+ ion was detected at m/z 976.4675 , IAPP carrying one CML (species B, [M+4H]4+ at 990,9697) and IAPP carrying one CEL (specie C, [M+4H]4+ at 994,4756).

Table 7. IAPP products obtained from MS analysis after incubation in the presence and in the absence of MGO.

Ion (m/z)	Peptide	Theoretical MW
977.2163	IAPP (A)	3906.32
991.7197	IAPP [CML] (B)	3960
995.2256	IAPP [CEL] (C)	3978

6.8 Analysis of the aggregate morphology of IAPP

The previous experiments suggested that glycation interfered with aggregation pathway of IAPP in a molar ratio-dependent manner. The high-resolution technique AFM was used to obtain a three-dimensional image of the morphology of the species formed at different time points for IAPP with and without MGO. To obtain representative results, the assay was replicated three times.

IAPP and glycated IAPP at a concentration of 10 µM were analysed after three-day incubation at 37°C. The micrographs of IAPP showed a mostly homogenous population of pre-fibrillar oligomers (**Fig. 40**, top, far left). This species, probably constituted by oligomers at different growth stages, occupied the majority of the micrograph. In the micrograph, also sparse individual, slightly branched fibres occurred. Although the height of the fibres varied (4.5-7.5 nm), their diameter was consistently around 16.5nm, indicative of single fibres.

In stark contrast, the glycated IAPP micrographs acquired after three days incubation at 37°C showed a dense field of a networks of disk-like species (**Fig. 40**, top, middle left). The aggregates assembled in a heavy structure characterised by a wreath-like shape. The presence of these bulky aggregates could explain the reduction of the CD signal as the consequence of a prominent precipitation. Their height was constant (5 nm) and their appearance of flat, interconnected ring-like structures. Compared to IAPP, the glycated sample clearly showed a different network of aggregates and intermediates.

To allow the fibres and other species to fully develop, samples were studied also after 17 days of incubation 37°C. For IAPP, the longer incubation time increased the density of fibres compared to day 3 (**Fig. 40**, top, right middle). These aggregates appeared needle-like in appearance. They were less branched than the previous sample but also showed more self-association. The diameter was largely unchanged from day 3 incubation, but the height decreases to 4.5 nm, perhaps indicating fibril remodelling. The corresponding glycated sample showed an evolution from disk-like towards highly-interconnected fibrillar species. The shape of this species was similar to the one formed by IAPP after 3-day incubation (**Fig. 40**, top, far right), although the glycated versions were visibly more branching, and disorder compared. The height of these newly-formed fibres was ranging between 2 nm and 7 nm, a much broader population than the one found after 3-day incubation. This evolution possibly suggested that the disk-like structures may have been indeed precursors of the fibrils.

This behaviour supports the evidence that glycation could induce IAPP to adopt a different aggregation pathway, also interfering with the kinetics of its fibrillisation. Indeed, the final fibrils formed by glycated and non-glycated IAPP showed a similar morphology, despite the very different pathway.

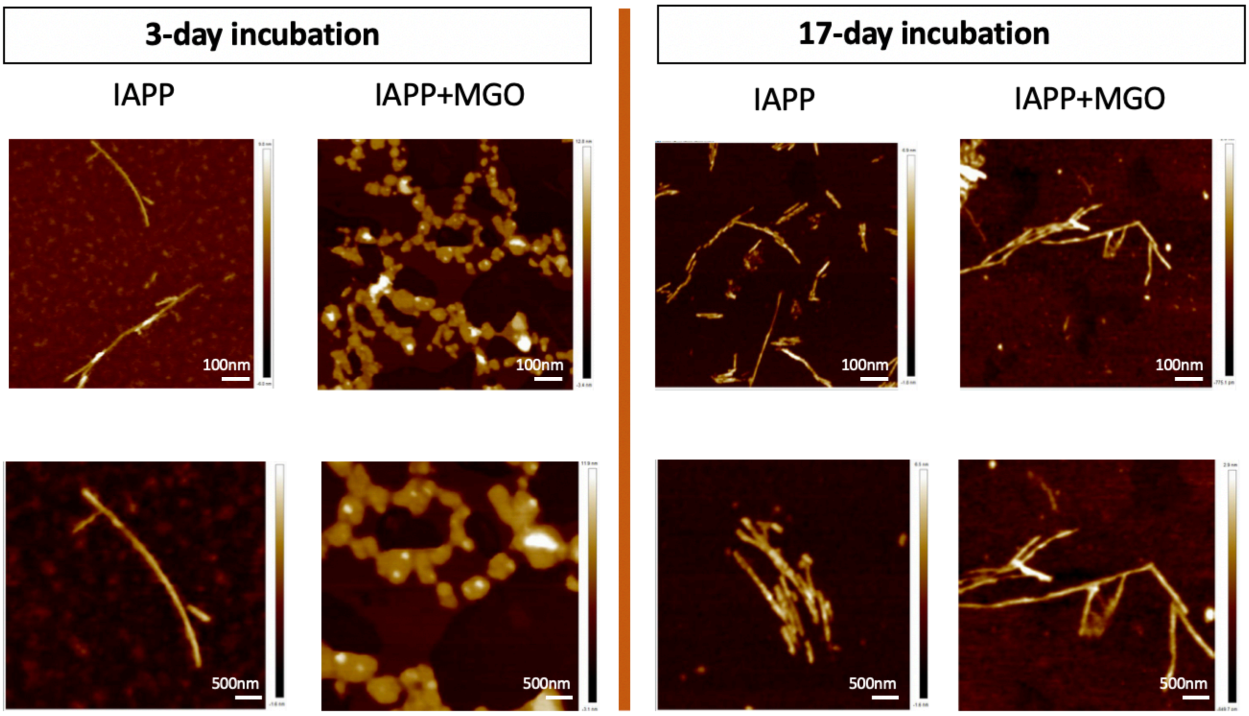

Figure 40. AFM micrographs of IAPP aggregates in the presence and the absence of excess MGO. The left and right panels correspond to 3-day and 17-day incubation, respectively. IAPP images are displayed with a 1 µm scale (top row) and with 0.5 µm scale (bottom row). The images show that glycation interfered

with the aggregation process either by changing the morphology of the fibres or possibly slowing down the aggregation kinetics.

Table 8. Measurements of IAPP fibres obtained by AFM. Height and diameter are shown at different incubation time (3 and 17 days).

	IAPP		**Glycated IAPP**	
Incubation time	**Height**	**Diameter**	**Height**	**Diameter**
3 days	4.5 nm – 7.6 nm	16.6 nm- 16.4 nm	5 nm	14.0 nm
17 days	4.3 nm	17.5 nm	5.5- 6.7 nm	19.6 nm

6. Discussion

6.1 Abeta

In this project, I investigated the effect of glycation, an enzyme-free addition of sugar to proteins, and its relation to protein aggregation using Abeta40 and Abeta42, the two main species observed in AD patients and IAPP, a peptide intimately associated with hyperglycaemia and T2D.

Abeta peptides are the main component of amyloid plaques, the extracellular deposits found in the brains of patients affected by AD (196). The role of the Abeta peptides in AD appears generally causative but many factors are still area of contention: the exact series of events involving Abeta amyloidogenesis, the molecular pathways that control pathological aggregation, and the precise toxic species of Abeta remain under investigation.

The most accepted theory is that the main toxic species are the oligomeric states or soluble aggregates rather than the mature fibres (197-199). Previous studies have demonstrated that Abeta peptides undergo glycation, a post- translational modification of increasing concern because of its association with toxic AGE species (200,201). The formation of AGEs, resulting from the reaction between reducing sugars and proteins, can alter the biological function of Abeta (46,202). Another considerable element that makes glycation a potential remarkable factor in AD is the observation that patients affected by diabetes, a disease directly linked to high sugar levels, have higher chance (5-fold more) to develop AD than other individuals (203). For this reason, it is extremely urgent to enquire whether and how glycation may interfere with the structure and aggregation properties of Abeta.

Employing a multidisciplinary approach, I demonstrated that glycation reduces the aggregation speed of both Abeta variants (Abeta40 and Abeta42) *in vitro.* Obtaining reproducible and reliable results was not straightforward. This was because the two processes under investigation, aggregation and glycation, are concomitant and partially competing. Aggregation and glycation strongly affect each other: glycation, as a post-translational modification, can influence the rate of aggregation process by altering the hydrophilic features of a protein (204). In addition, aggregation can hamper glycation by hiding the glycation sites and burying them in the core of the protein, rendering them unavailable. These two processes, glycation and aggregation, can nevertheless be followed independently by exploiting the different spectrofluorometric properties of their products.

Mass spectrometry was employed to identify the glycation sites by trypsin digestion (194). The combination of trypsin digestion and MS analysis identified Arg5 and Lys11 as glycation sites in Abeta peptides. The glycation reaction at Arg5 generated the fluorescent product ArgP, the formation of which was followed at a specific wavelength. When excited at 320 nm, ArgP emitted a fluorescent signal at 405 nm, while ThT, in the presence of amyloid-like structures, emitted at 485 nm (179) when excited at 440 nm. To investigate the effect of glycation, the glycating agent employed was methylglyoxal (MGO) a dicarbonyl compound produced during glucose metabolism. In this project, I showed that glycation of Arg5 was completed on both Abeta40 and on Abeta42. In particular, glycation of both Abeta variants occurred in a window of roughly 24 hours, the exact time by which Abeta40 reached the aggregation plateau. To be noticed is that, although Abeta42 was completely aggregated in just 12 hours, the glycation, unexpectedly, continued for further 12 hours. This interesting behaviour of Abeta42 could be explained in several ways. The first reason could be the fact that the arginine, a polar, charged residue, is still exposed to the solvent even after complete aggregation. The second reason could be the presence of a monomeric species that does not take part in the aggregation process and that is the substrate of the glycation reaction occurring in the final 12 hours of the kinetics.

As shown by ThT binding assays, the aggregation of both Abeta forms was affected by the concomitant glycation reaction that slowed down the process without completely hindering it. Although ThT binding assay cannot provide qualitative information, the amyloid-like structures formed by glycated samples appeared to be reduced compared to the native peptides. This result was confirmed by AFM micrographs displaying an apparent smaller amount of fibres and aggregates, characterised by a different morphology between glycated and non-glycated samples.

During the ThT binding assay, the addition of certain amount of MGO to Abeta40 seemed to reduce the slope of the sigmoid, corresponding to the elongation phase of the aggregation reaction. The addition of MGO also interfered with the lag phase by slowing down the kinetics. The most evident effect was detected in the elongation phase of the aggregation (**Fig**. 24). In the case of Abeta40, the effect on the elongation phase was proportional to the increasing amount of MGO, indicating a concentration-dependent effect of MGO on the aggregation of this variant of Abeta. This result was not reproducible with Abeta42 in the same conditions used for Abeta40. MGO had a substantial effect on Abeta42 lag phase but only slightly altered the elongation phase. The most prominent effect was noticed on the final amount of aggregates, which was significantly reduced compared to non-glycated samples.

In addition, the effect of glycation on the secondary structure of Abeta variants was investigated by means of circular dichroism (CD) spectroscopy. In the absence of MGO, I observed that Abeta42 transited from mixture of beta-sheet and random coil to pure beta-sheet structures and that this conformational change was delayed by the glycation reaction. In Abeta40 the transition is not visible, as the peptide remained in a random coil conformation. Also, the non-glycated Abeta40 showed a clear transition, starting from a mixture containing random coil conformation at time zero and transitioning to a beta-sheet conformation after six hours. In the presence of MGO, instead, Abeta40 maintained mostly a random coil conformation. (180). Its longer permanence in a random coil conformation during the glycation reaction would explain the effect of MGO in delaying the elongation phase during the aggregation assay.

Studies suggested that MGO-glycation of different proteins leads to the formation and stabilisation of small and soluble aggregated species that retain native-like structure (205-207). Here, I showed that MGO-glycation of Abeta40 has minimal effects on the secondary structure of the peptide i.e. the secondary structure of MGO-glycated Abeta40 did not change relative to native Abeta40. Possibly, glycation stabilised the unfolded state of the peptide even after 12 hours and with a high excess of MGO to Abeta40. Our data should be put in the frame of previous results on Abeta peptides using MGO or similar glycating agents.

Oliveira et al. supported this hypothesis demonstrating that glycation affected the conformational stability of proteins (207). This group studied the effect of MGO on cytochrome C, which is not involved in amyloidogenic diseases but was previously employed as a model to study protein aggregation (208). They proposed that glycation of aggregation-prone proteins could lead to a different aggregation pathway. They suggested that instead of undergoing to a canonical amyloidogenic pathway, glycated peptides adopt a native-like aggregation one. In support to this theory they demonstrated how this native-like aggregation pathway was thermodynamically and kinetically more favoured.

Another study about the effect of glycation on Abeta was carried out employing a different glycating agent: Vitek et al. tested the effect of glucose on Abeta40 and a shorter fragment (Abeta$_{1-28}$) (209). Their results showed an increased aggregation rate in the presence of AGE-modified proteins. In particular, pre-aggregated amyloid aggregates were added to the two Abeta variants as seeds. The discrepancy between their results and the ones presented in this work, however, could be explained by differences in methodology. They carried out the aggregation assays with a monomeric form of Abeta variants observing the formation of amyloid-like structures after four months. An AGE-modified peptide was added to compare the effect of glycation. This glycated peptide was already aggregated and was acting as a seed. Therefore, the enhanced aggregation could be explained by the presence of AGE nucleation seeds that are well known to be responsible for increased aggregation rates.

Also the work presented by Nomoto et al. (210) employed glucose as glycating agent. The glycation reaction resulting from glucose leads to pentosidine, a fluorescent glycation product very different from the one obtained from MGO, clearly highlighting how important the specific glycating agent is.

A different study focused on the combination of computational and experimental approaches, using glyoxylic acid and cyanogen bromide as glycating agents. (211). The computational analysis on Abeta42 focused on the effects of glycation on the free energy of the peptide. The glycated Abeta42 monomer was generated by modifying the lysine residues at positions 16 and 28 to N-(6)-carboxymethyllysine (CML), one of the possible AGEs. CML is an AGE chemically very different from CEL and ArgP products that was observed by MS in our study. Their data are thus hard to compare with ours.

Our data are instead in full agreement with a previous study using synthetic Abeta42. This peptide was glycated *in vitro* with the same glycation agent used in this work and was used to study the toxicity of glycated Abeta42 on primary hippocampal neurons (200). It was observed that glycation exacerbates neurotoxicity of Abeta with up-regulation of the AGE receptor and activation of glycogen synthase kinase-3. I suggest an explanation about that this behaviour by considering that, according to my results, the slower process of fibre formation could have the effect of stabilising the oligomeric state, generally believed to be the toxic species. If true, this hypothesis would urgently solicit the identification of new effective ways to prevent sugar accumulation in the blood and reduce the risk of Abeta glycation. It was therefore compelling to study the effect of glycation on other diabetes-related peptides, such as amylin and, in the future, maybe also alpha-synuclein, since this line of research may unveil further important details about the relationship between these two pathologies.

6.1 IAPP

A major accepted cause of type-2-diabetes, T2D, is the aggregation of IAPP, a peptide hormone co-produced and co-secreted along with insulin from the endocrine beta-cells of the pancreas (105). Misfolded IAPP is the primary constituent of amyloid deposits in the pancreatic islets. These toxic amyloid-like structures are very similar to the Abeta peptide deposits, often also heavily glycated, observed in the brains of patients affected by AD. IAPP can be a good model to investigate the effect of glycation on protein aggregation.

Increasing evidence suggested that the pre-fibrillar oligomers of IAPP were the primary toxic agents rather than the amyloid fibrils as in many other aggregation prone proteins (100,212). However, in contrast to other peptides such as insulin, immunoglobulin G, alpha synuclein and bovine serum albumin, little is known about the effect of glycation on the structural properties and aggregation kinetics of IAPP (179,206,213,214).

IAPP is an intrinsically disordered protein intimately associated with hyperglycaemia. Using a combination of spectroscopic and other biophysical techniques, the current work demonstrated that glycation affected the aggregation of IAPP by reducing aggregation rates. This effect was associated with an altered secondary structure transition and with a different morphology of the IAPP aggregates.

The glycation reaction is a slow reaction under physiological conditions that requires time to show its pathological effects (215). At the early stages of modification, lysine, arginine and histidine residues are the main available sites of MGO modification (216). However, IAPP structural models proposed in the past were unclear as to whether these amino acids were solvent exposed, when the protein was monomeric and in solution. (131,133). The exposure of specific residues could drastically interfere with the glycation reaction. In this study, I observed that MGO-glycation of IAPP resulted in the formation of CML and CEL, two of the most common AGEs found in the literature (48,49,195). The modification occurred on the amine function belonging to the N-terminal of the protein or the ε-amine group of Lys1. Since the two groups are located on the same amino acid, it was not possible to define which of the two was the actual modification site by mass spectrometry. On the other hand, no production of hydroimidazolone, argpyrimidine on Arg11 or MGO-derived products on His18 was detected. This was the first evidence showing that glycation occurs at the first IAPP residue, probably because it was the most accessible to MGO-modification.

Studies suggested that glycation would affect the structural properties and aggregation kinetics of proteins in different ways. For example, glycation would alter the rate of formation of amyloid fibrils for different proteins (217,218). Here, I demonstrated that MGO-glycation of IAPP slightly interfered with the lag phase but dramatically altered the rate of IAPP aggregation, by decreasing the slope of the aggregation curve. The decrease was from a value of 0.70 for non-glycated Abeta to a final 0.20 for glycated Abeta, as supported by the ThT-binding assays (**Fig. 24**). The proportional increase in elongation during the kinetics induced by increasing excess of MGO suggested that the relative concentration of MGO to IAPP played a crucial role. Therefore, MGO-glycation affected the kinetics of fibril formation in a concentration-dependent manner.

This work reported that the glycation reaction preserved IAPP native conformation, by blocking the alpha-helix-to-beta-sheet transition characteristic of amyloid fibril formation. This was in agreement with the reduction of fibril formation observed in ThT kinetic measurements. It also suggested a low tendency to conformational changes in glycated IAPP, responsible for blocking the seeding nuclei formation, resulting in a reduced fibril formation. The glycated IAPP CD spectra displayed a clear reduction in ellipticity signal intensity over incubation time. It could be argued that the reason for this signal reduction in the presence of MGO may be peptide precipitation, which would also explain the proportional reduction of ThT signal. This hypothesis is plausible but is not supported by AFM evidence. According to AFM micrographs, the amount of fibres of glycated IAPP were eventually less abundant than the non-glycated counterpart.

AFM was employed to investigate the morphology of IAPP in the presence and in the absence of MGO. Glycation did not affect remarkably the morphology of IAPP but would lead IAPP towards a different aggregation pathway: non-glycated IAPP displayed the formation of fibres over 17-day incubation following a canonical pathway that goes from the monomeric form to fibrillar aggregates. Glycated IAPP showed an evolution from disk-like towards highly-interconnected fibrillar species. Uniform disk-shaped particles were reported also by Zhu investigating the *in vitro* assembly of a recombinant amyloidogenic low chain variable domain (219). Their high disk-shaped aggregates converted into oligomers and protofibrils after five-day incubation at 37 °C. These data obtained by Zhu correlated with my results showing that disk-like aggregates would adopt a different aggregation pathway eventually leading to the formation of fibrillar aggregates.

My results showed a great difference in terms of aggregates' crowdedness between glycated and non-glycated samples. Although AFM is not a technique providing accurate quantitative information, it was clear that both glycated and non-glycated IAPP showed fibres with a similar morphology after 17-day incubation, but with a strong difference in terms of amount of fibres. The glycated sample showed a smaller number of fibrillar species, apparently caused by a slower aggregation process. This behaviour supported the evidence that glycation induced IAPP to adopt a different aggregation pathway, also interfering with the kinetics of its fibrillisation, by slowing it down.

These data partially fitted into a wide framework of studies on IAPP aggregation. It is undeniable that IAPP aggregation is very sensitive to residue change and post-translational modifications. Indeed, several studies showed that post translational modifications on specific amino acid side chains would significantly accelerate or decelerate IAPP aggregation (220,221). Recently, the effect of IAPP deamidation, a spontaneous non-enzymatic post translational modification resulting in the conversion of asparagine into a mixture of aspartic acid and isoaspartic acid, was investigated by two different groups. Dunkelberger et al. demonstrated that IAPP deamidation accelerated IAPP self-assembly, by altering the fibres structure (220). In particular, the amino acids responsible of this acceleration were identified as Asn14 and Asn21 but not Asn 22, Asn 31, and Asn 35 (221). Even a small portion of deamidated IAPP (N14D) could have a crucial role by inducing the aggregation of wild-type IAPP.

Glycation of IAPP was previously investigated using similar glycating agents. One of the first studies was carried out by Kapurniotu et al. reporting that glycated IAPP was more amyloidogenic. The different outcome could lay on several factors. Firstly, they employed D-glucose as the glycating agent, which was demonstrated to be up to 50,000 times less reactive than MGO (37-39). Secondly, the authors obtained a different AGE: they described the conversion of the Arg11 guanidine group to an imidazolone. This can be explained by the use a different glycating agent. Thirdly, the procedures followed were extremely different. The glucose-glycation product (AGE-IAPP) was left in incubation for four days and then added to native IAPP. The AGE-IAPP worked as a seed and the addition of native IAPP could strongly interfere with the enhanced aggregation process.

These results could possibly be related to the aggregation behaviour of amyloidogenic proteins upon glycation. In fact, both insulin and alpha-synuclein, which are involved in amyloid diseases, and also cytochrome C, a protein recently used as a model to study protein aggregation, showed less amyloid fibril formation after glycation (205-207).

Another study focused on the relationship between IAPP and sugars was carried out in 2000. This noteworthy study demonstrated that glucose has a strong effect on IAPP gene transcription (222).

This means that glucose, by controlling IAPP gene transcription, greatly influences the expression and the amounts of IAPP.

Overall, the effect of glucose and its metabolism products on IAPP in the glycation reaction is a currently in the spotlights. In this work I demonstrated that glycation slowed down IAPP aggregation and this could have serious consequences on IAPP toxicity. Haataja et al. demonstrated that IAPP oligomers were the most toxic form among the IAPP aggregates and induced membrane leakage and disruption (223). These oligomers were able to cross the plasma membrane and appeared to act similarly to prions (224,225). Since glycation slowed down the aggregation process, presumably the oligomeric form was maintained for longer time before eventually forming amyloid-like aggregates. This means that the glycated IAPP peptides can be more toxic as a consequence of their longer persistence as oligomeric species.

6.2 Abeta and IAPP

T2D and AD are characterised by insoluble protein aggregates with a fibrillar conformation, IAPP in T2D pancreatic islets, and Abeta in AD brain (226). IAPP aggregation is associated with pancreatic beta-cell loss, whereas Abeta formation is associated with neuronal cell loss. Beta-cell loss leads to diabetes, nerve cell loss to dementia. Therefore, T2D and AD have several features in common. Studies of the aetiology of these diseases is crucial to understand the mechanism undergoing. One of the trigger processes affecting these diseases is protein aggregation of Abeta for AD and IAPP for T2D. Although the aggregation of these amyloidogenic proteins has been previously studied *in vitro*, the possibility of a common triggering molecular mechanism is still area of contention.

Post translational modifications are known to affect protein structure and function (54,204). Some of these modifications may affect proteins stability and lead to their misfolding and accumulation. Reducing sugars play an important role in modifying proteins, forming AGEs. The post-translational modifications responsible for the non-enzymatic addition of sugars to proteins is glycation. Recently, much attention has been devoted to the role played by glycation in affecting amyloid aggregation and cellular toxicity. Amyloid deposits are often found rich in glycated proteins, suggesting a direct correlation between protein glycation and amyloidosis. Vitek et al. reported, for the first time in 1994, that plaque fractions of AD brains contained about three-fold more AGE adducts than preparations from healthy, age-matched controls (209). In the same year, this outcome was corroborated by a different group that identified AGEs as major components of amyloid plaques, by means of immunohistochemical studies on post-mortem tissues (227).

In summary, this work focused on the molecular effects induced by MGO-glycation in the amyloid aggregation of Abeta and IAPP. Overall, glycation decreased the elongation rate in both protein kinetics in a concentration-dependent manner. The slower kinetics were also supported by the CD data collected to study the peptide secondary structure demonstrating that glycation reduced the speed of conformational transitions towards beta sheets. The effect on Abeta40 was more visible than on Abeta42. For Abeta40 the transition from random coil to beta-sheet structure was firmly halted whereas for Abeta42 variant the transition from a mixture containing beta sheet and random coil to pure beta-sheet conformation was considerably delayed. A similar decelerating effect was described for IAPP whose secondary structure transition was from random coil/alpha helix to beta sheet conformation. The effects of glycation described in this work were highlighted by the difference of morphology of fibres from glycated and non-glycated samples. In AFM micrographs of both Abeta and IAPP, the glycated samples displayed a smaller amount of fibrillar aggregates as compared to the non-glycated peptides incubated under the same conditions at the same time points. The smaller amounts of aggregates detected by AFM was in accordance with the other data collected with ThT binding assay and by means of CD spectroscopy.

These data suggested that glycation played a crucial role in the aggregation process of peptides involved in AD and T2D and it could be the molecular mechanism linking the diseases. This should be put in frame with several works. Among these, Li et al. reported that MGO-glycated Abeta peptide exacerbated the neuronal toxicity by the upregulation of the receptor for AGEs (RAGE) and subsequent activation of death-signalling pathways. This was explained by the relationship between Abeta and RAGE. Abeta peptide was previously identified as a ligand of RAGE, and their interaction triggered the activation of different pathways of death-signalling (228).

Another study supporting the link between AD and T2D was presented by Cao et al. suggesting the potential role of dietary sugar in the pathogenesis of AD. An incorrect diet and high blood glucose play a crucial role in the epidemic of obesity, a major risk factor for T2D. They suggested that controlling the consumption of sugar-sweetened beverages could be an effective way to curtail the risk of developing AD. In this study, a transgenic mouse model of AD (APP/PSY) fed with 10% sucrose-sweetened water was compared with rodents under normal diet. The mice assuming sugar gained weight, developed hyperinsulinemia, hypercholesterolemia and glucose intolerance, typical T2D symptoms. Another surprising effect was the memory impairment and the 2-3-fold increase in Abeta amyloid-deposition in the brain (229). The exacerbation of cerebral amyloidosis in sucrose-treated mice is the evidence supporting that glycation can be the cause of the early AD onset on T2D patients.

The results obtained in this work stated that AD and T2D may share a common mechanistic cause. According to these outcomes, the correlation could lay on glycation. These findings highlighting a clear association between AD and T2D and may give insights to approach them differently. The link between these two diseases could open the way to treat them for which symptoms have been so far treated separately. This would make an impact in the healthcare system, and on the community.

In conclusion, T2D is one of the most common long-term health conditions, characterised by serious complications gradually developing as an intrusive and wearing presence in patients' everyday life. Patients affected by neurodegenerative disorders suffer from a significant physical and cognitive loss and require intensive, long-term healthcare, becoming dependent on family or caregivers. These diseases are a burden to their patients' lives. By moving towards the identification of new therapeutic strategy, I aim to contribute in the improvement of the health and well-being of these patients. My hope is that the vast community working on misfolding diseases, as well as pharmaceutical companies, may take inspiration from this outcome.

Appendix 1

ABETA 40 (230)

```
                10                   20                   30                   40
DAEFRHDSG YEVHHQKLVF FAEDVGSNKG AIIGLMVGGV V
```

Number of amino acids: 40

Molecular weight: 4329.86

Theoretical pI: 5.31

Amino acids	Number of amino acids	Composition percentage
Ala (A)	3	7.5%
Arg (R)	**1**	**2.5%**
Asn (N)	1	2.5%
Asp (D)	3	7.5%
Cys (C)	0	0.0%
Gln (Q)	1	2.5%
Glu (E)	3	7.5%
Gly (G)	6	15.0%
His (H)	3	7.5%
Ile (I)	2	5.0%

Leu (L)	2	5.0%
Lys (K)	2	**5.0%**
Met (M)	1	2.5%
Phe (F)	3	7.5%
Pro (P)	0	0.0%
Ser (S)	2	5.0%
Thr (T)	0	0.0%
Trp (W)	0	0.0%
Tyr (Y)	1	2.5%
Val (V)	6	15.0%

Total number of negatively charged residues (Asp + Glu): 6
Total number of positively charged residues (Arg + Lys): 3

Atomic composition:

Carbon	C	194
Hydrogen	H	295
Nitrogen	N	53
Oxygen	O	58
Sulfur	S	1

Formula: $C_{194} H_{295} N_{53} O_{58} S_1$
Total number of atoms: 601

Extinction coefficients:
This protein does not contain any Trp residues. Experience shows that this could result in more than 10% error in the computed extinction coefficient.

Extinction coefficients are in units of M-1 cm-1, at 280 nm measured in water.

Ext. coefficient 1490 - Abs 0.1% (=1 g/l) 0.344

ABETA 42 (230)

10 20 30 40

DAEFRHDSG YEVHHQKLVF FAEDVGSNKG AIIGLMVGGV VIA

Number of amino acids: 42

Molecular weight: 4514.10

Theoretical pI: 5.31

Amino acids	Number of amino acids	Composition percentage
Ala (A)	4	9.5%
Arg (R)	**1**	**2.4%**
Asn (N)	1	2.4%
Asp (D)	3	7.1%
Cys (C)	0	0.0%
Gln (Q)	1	2.4%
Glu (E)	3	7.1%
Gly (G)	6	14.3%
His (H)	3	7.1%
Ile (I)	3	7.1%
Leu (L)	2	4.8%

Lys (K)	2	**4.8%**
Met (M)	1	2.4%
Phe (F)	3	7.1%
Pro (P)	0	0.0%
Ser (S)	2	4.8%
Thr (T)	0	0.0%
Trp (W)	0	0.0%
Tyr (Y)	1	2.4%
Val (V)	6	14.3%

Total number of negatively charged residues (Asp + Glu): 6

Total number of positively charged residues (Arg + Lys): 3

Atomic composition:

Carbon	C	203
Hydrogen	H	311
Nitrogen	N	55
Oxygen	O	60
Sulfur	S	1

Formula: C203 H311 N55 O60 S1

Total number of atoms: 630

Extinction coefficients:

This protein does not contain any Trp residues. Experience shows that this could result in more than 10% error in the computed extinction coefficient.

Extinction coefficients are in units of M-1 cm-1, at 280 nm measured in water.

Ext. coefficient 1490 - Abs 0.1% (=1 g/l) 0.330

IAPP (230)

10 20 30

KCNTATCAT QRLANFLVHS SNNFGAILSS TNVGSNTY

Number of amino acids: 37

Molecular weight: 3906.32

Theoretical pI: 8.90

Amino acids	Number of amino acids	Composition percentage
Ala (A)	4	10.8%
Arg (R)	**1**	**2.7%**
Asn (N)	6	16.2%
Asp (D)	0	0.0%
Cys (C)	2	5.4%
Gln (Q)	1	2.7%
Glu (E)	0	0.0%
Gly (G)	2	5.4%
His (H)	1	2.7%
Ile (I)	1	2.7%
Leu (L)	3	8.1%

Lys (K)	1	**2.7%**
Met (M)	0	0.0%
Phe (F)	2	5.4%
Pro (P)	0	0.0%
Ser (S)	5	13.5%
Thr (T)	5	13.5%
Trp (W)	0	0.0%
Tyr (Y)	1	2.7%
Val (V)	2	5.4%

Total number of negatively charged residues (Asp + Glu): 0

Total number of positively charged residues (Arg + Lys): 2

Atomic composition:

Carbon	C	165
Hydrogen	H	262
Nitrogen	N	50
Oxygen	O	56
Sulfur	S	2

Formula: C165 H262 N50 O56 S2

Total number of atoms: 535

Extinction coefficients:

This protein does not contain any Trp residues. Experience shows that this could result in more than 10% error in the computed extinction coefficient.

Extinction coefficients are in units of M-1 cm-1, at 280 nm measured in water.

Ext. coefficient 1615

Abs 0.1% (=1 g/l) 0.413, assuming all pairs of Cys residues form cystines

Ext. coefficient 1490

Abs 0.1% (=1 g/l) 0.381, assuming all Cys residues are reduced

Appendix 2

Sequence of fusion protein in the form leader-IAPP-intein-CBD. It was subject of intein cleavage resulting in C-amidated leader-IAPP protein.

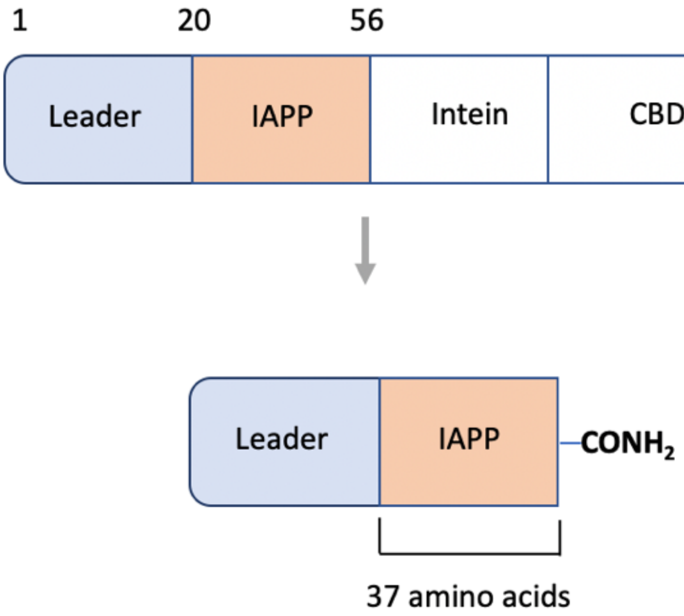

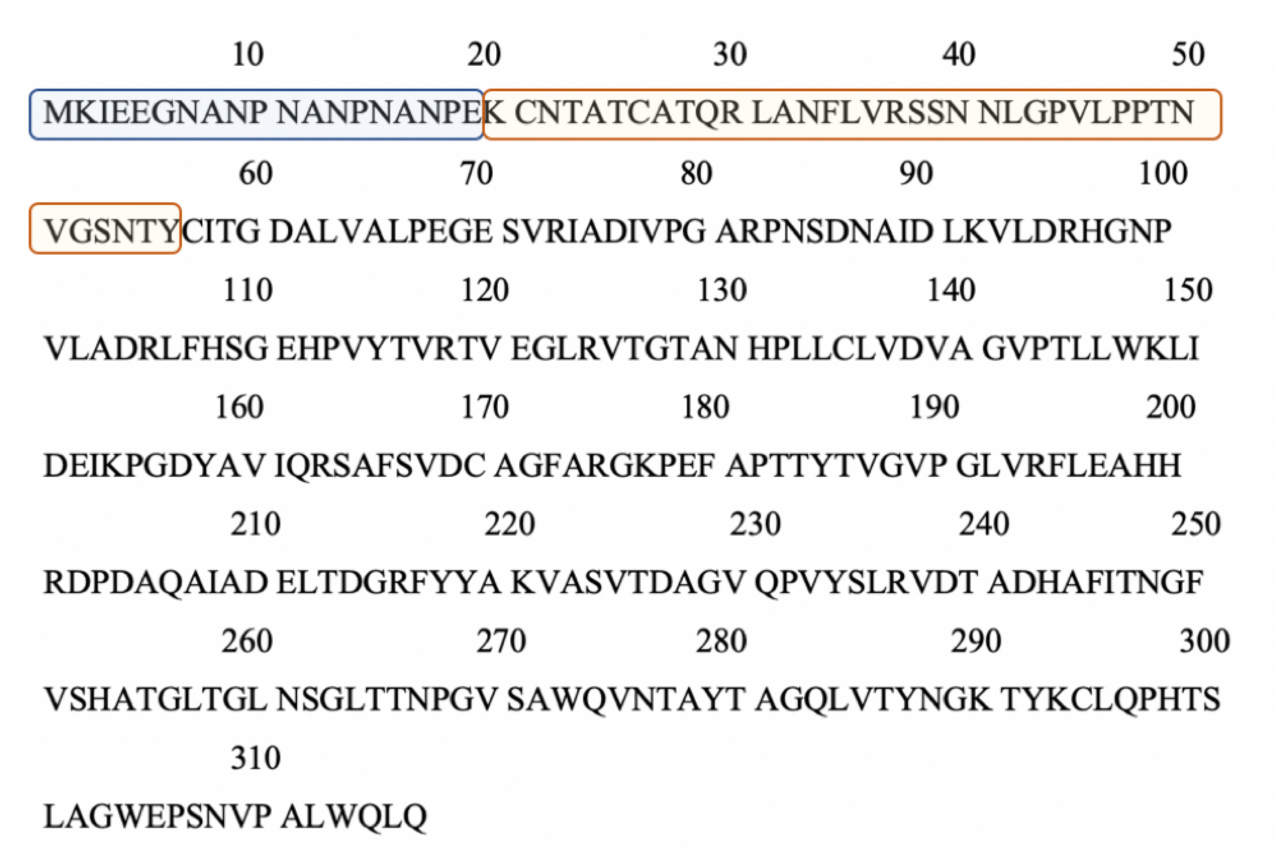
10 20 30 40 50

MKIEEGNANP NANPNANPEK CNTATCATQR LANFLVRSSN NLGPVLPPTN

60 70 80 90 100

VGSNTYCITG DALVALPEGE SVRIADIVPG ARPNSDNAID LKVLDRHGNP

110 120 130 140 150

VLADRLFHSG EHPVYTVRTV EGLRVTGTAN HPLLCLVDVA GVPTLLWKLI

160 170 180 190 200

DEIKPGDYAV IQRSAFSVDC AGFARGKPEF APTTYTVGVP GLVRFLEAHH

210 220 230 240 250

RDPDAQAIAD ELTDGRFYYA KVASVTDAGV QPVYSLRVDT ADHAFITNGF

260 270 280 290 300

VSHATGLTGL NSGLTTNPGV SAWQVNTAYT AGQLVTYNGK TYKCLQPHTS

310

LAGWEPSNVP ALWQLQ

8. References

1. Knowles, T. P., Vendruscolo, M., and Dobson, C. M. (2014) The amyloid state and its association with protein misfolding diseases. *Nat Rev Mol Cell Biol* **15**, 384-396
2. Chiti, F., and Dobson, C. M. (2006) Protein misfolding, functional amyloid, and human disease. *Annu Rev Biochem* **75**, 333-366
3. Eisenberg, D., and Jucker, M. (2012) The amyloid state of proteins in human diseases. *Cell* **148**, 1188-1203
4. Sunde, M., Serpell, L. C., Bartlam, M., Fraser, P. E., Pepys, M. B., and Blake, C. C. (1997) Common core structure of amyloid fibrils by synchrotron X-ray diffraction. *J Mol Biol* **273**, 729-739
5. Dobson, C. M. (2002) Getting out of shape. *Nature* **418**, 729-730
6. Biancalana, M., and Koide, S. (2010) Molecular mechanism of Thioflavin-T binding to amyloid fibrils. *Biochim Biophys Acta* **1804**, 1405-1412
7. Fernandez, M. S. (2014) Human IAPP amyloidogenic properties and pancreatic beta-cell death. *Cell Calcium* **56**, 416-427
8. Bucciantini, M., Giannoni, E., Chiti, F., Baroni, F., Formigli, L., Zurdo, J., Taddei, N., Ramponi, G., Dobson, C. M., and Stefani, M. (2002) Inherent toxicity of aggregates implies a common mechanism for protein misfolding diseases. *Nature* **416**, 507-511
9. Sawaya, M. R., Sambashivan, S., Nelson, R., Ivanova, M. I., Sievers, S. A., Apostol, M. I., Thompson, M. J., Balbirnie, M., Wiltzius, J. J., McFarlane, H. T., Madsen, A. O., Riekel, C., and Eisenberg, D. (2007) Atomic structures of amyloid cross-beta spines reveal varied steric zippers. *Nature* **447**, 453-457
10. Schmidt, M., Rohou, A., Lasker, K., Yadav, J. K., Schiene-Fischer, C., Fandrich, M., and Grigorieff, N. (2015) Peptide dimer structure in an Abeta(1-42) fibril visualized with cryo-EM. *Proc Natl Acad Sci U S A* **112**, 11858-11863
11. Tycko, R. (2006) Molecular structure of amyloid fibrils: insights from solid-state NMR. *Q Rev Biophys* **39**, 1-55
12. Der-Sarkissian, A., Jao, C. C., Chen, J., and Langen, R. (2003) Structural organization of alpha-synuclein fibrils studied by site-directed spin labeling. *J Biol Chem* **278**, 37530-37535
13. Jayasinghe, S. A., and Langen, R. (2004) Identifying structural features of fibrillar islet amyloid polypeptide using site-directed spin labeling. *J Biol Chem* **279**, 48420-48425
14. Sachse, C., Fandrich, M., and Grigorieff, N. (2008) Paired beta-sheet structure of an Abeta(1-40) amyloid fibril revealed by electron microscopy. *Proc Natl Acad Sci U S A* **105**, 7462-7466
15. Sumner Makin, O., and Serpell, L. C. (2004) Structural characterisation of islet amyloid polypeptide fibrils. *J Mol Biol* **335**, 1279-1288
16. Paravastu, A. K., Leapman, R. D., Yau, W. M., and Tycko, R. (2008) Molecular structural basis for polymorphism in Alzheimer's beta-amyloid fibrils. *Proc Natl Acad Sci U S A* **105**, 18349-18354
17. Zandomeneghi, G., Krebs, M. R., McCammon, M. G., and Fandrich, M. (2004) FTIR reveals structural differences between native beta-sheet proteins and amyloid fibrils. *Protein Sci* **13**, 3314-3321
18. Nilsson, M. R. (2004) Techniques to study amyloid fibril formation in vitro. *Methods* **34**, 151-160
19. Mathis, C. A., Mason, N. S., Lopresti, B. J., and Klunk, W. E. (2012) Development of positron emission tomography beta-amyloid plaque imaging agents. *Semin Nucl Med* **42**, 423-432

20. Soto, C. (2003) Unfolding the role of protein misfolding in neurodegenerative diseases. *Nat Rev Neurosci* **4**, 49-60
21. White, D. A., Buell, A. K., Knowles, T. P., Welland, M. E., and Dobson, C. M. (2010) Protein aggregation in crowded environments. *J Am Chem Soc* **132**, 5170-5175
22. Ruggeri, F. S., Habchi, J., Cerreta, A., and Dietler, G. (2016) AFM-Based Single Molecule Techniques: Unraveling the Amyloid Pathogenic Species. *Curr Pharm Des* **22**, 3950-3970
23. Cohen, S. I., Linse, S., Luheshi, L. M., Hellstrand, E., White, D. A., Rajah, L., Otzen, D. E., Vendruscolo, M., Dobson, C. M., and Knowles, T. P. (2013) Proliferation of amyloid-beta42 aggregates occurs through a secondary nucleation mechanism. *Proc Natl Acad Sci U S A* **110**, 9758-9763
24. Scheidt, T., Lapinska, U., Kumita, J. R., Whiten, D. R., Klenerman, D., Wilson, M. R., Cohen, S. I. A., Linse, S., Vendruscolo, M., Dobson, C. M., Knowles, T. P. J., and Arosio, P. (2019) Secondary nucleation and elongation occur at different sites on Alzheimer's amyloid-beta aggregates. *Sci Adv* **5**, eaau3112
25. Bonito-Oliva, A., Barbash, S., Sakmar, T. P., and Graham, W. V. (2017) Nucleobindin 1 binds to multiple types of pre-fibrillar amyloid and inhibits fibrillization. *Sci Rep* **7**, 42880
26. Meisl, G., Yang, X., Hellstrand, E., Frohm, B., Kirkegaard, J. B., Cohen, S. I., Dobson, C. M., Linse, S., and Knowles, T. P. (2014) Differences in nucleation behavior underlie the contrasting aggregation kinetics of the Abeta40 and Abeta42 peptides. *Proc Natl Acad Sci U S A* **111**, 9384-9389
27. Ruschak, A. M., and Miranker, A. D. (2007) Fiber-dependent amyloid formation as catalysis of an existing reaction pathway. *Proc Natl Acad Sci U S A* **104**, 12341-12346
28. Fodera, V., Librizzi, F., Groenning, M., van de Weert, M., and Leone, M. (2008) Secondary nucleation and accessible surface in insulin amyloid fibril formation. *J Phys Chem B* **112**, 3853-3858
29. Buell, A. K., Galvagnion, C., Gaspar, R., Sparr, E., Vendruscolo, M., Knowles, T. P., Linse, S., and Dobson, C. M. (2014) Solution conditions determine the relative importance of nucleation and growth processes in alpha-synuclein aggregation. *Proc Natl Acad Sci U S A* **111**, 7671-7676
30. Gaspar, R., Meisl, G., Buell, A. K., Young, L., Kaminski, C. F., Knowles, T. P. J., Sparr, E., and Linse, S. (2017) Secondary nucleation of monomers on fibril surface dominates alpha-synuclein aggregation and provides autocatalytic amyloid amplification. *Q Rev Biophys* **50**, e6
31. Garg, D. K., and Kundu, B. (2016) Clues for divergent, polymorphic amyloidogenesis through dissection of amyloid forming steps of bovine carbonic anhydrase and its critical amyloid forming stretch. *Biochim Biophys Acta* **1864**, 794-804
32. Vassar, P. S., and Culling, C. F. (1959) Fluorescent stains, with special reference to amyloid and connective tissues. *Arch Pathol* **68**, 487-498
33. Sambataro, F., and Pennuto, M. (2017) Post-translational Modifications and Protein Quality Control in Motor Neuron and Polyglutamine Diseases. *Front Mol Neurosci* **10**, 82
34. Ulrich, P., and Cerami, A. (2001) Protein glycation, diabetes, and aging. *Recent Prog Horm Res* **56**, 1-21
35. Hipkiss, A. R., Michaelis, J., and Syrris, P. (1995) Non-enzymatic glycosylation of the dipeptide L-carnosine, a potential anti-protein-cross-linking agent. *FEBS Lett* **371**, 81-85
36. Szwergold, B. S. (2005) Carnosine and anserine act as effective transglycating agents in decomposition of aldose-derived Schiff bases. *Biochem Biophys Res Commun* **336**, 36-41
37. Schalkwijk, C. G. (2015) Vascular AGE-ing by methylglyoxal: the past, the present and the future. *Diabetologia* **58**, 1715-1719

38. Rabbani, N., and Thornalley, P. J. (2008) Dicarbonyls linked to damage in the powerhouse: glycation of mitochondrial proteins and oxidative stress. *Biochem Soc Trans* **36**, 1045-1050
39. Annibal, A., Riemer, T., Jovanovic, O., Westphal, D., Griesser, E., Pohl, E. E., Schiller, J., Hoffmann, R., and Fedorova, M. (2016) Structural, biological and biophysical properties of glycated and glycoxidized phosphatidylethanolamines. *Free Radic Biol Med* **95**, 293-307
40. Gkogkolou, P., and Bohm, M. (2012) Advanced glycation end products: Key players in skin aging? *Dermatoendocrinol* **4**, 259-270
41. Chatham, J. C., Gilbert, H. F., and Radda, G. K. (1989) The metabolic consequences of hydroperoxide perfusion on the isolated rat heart. *Eur J Biochem* **184**, 657-662
42. Abordo, E. A., Minhas, H. S., and Thornalley, P. J. (1999) Accumulation of alpha-oxoaldehydes during oxidative stress: a role in cytotoxicity. *Biochem Pharmacol* **58**, 641-648
43. Danpure, C. J., and Rumsby, G. (2004) Molecular aetiology of primary hyperoxaluria and its implications for clinical management. *Expert Rev Mol Med* **6**, 1-16
44. Semba, R. D., Nicklett, E. J., and Ferrucci, L. (2010) Does accumulation of advanced glycation end products contribute to the aging phenotype? *J Gerontol A Biol Sci Med Sci* **65**, 963-975
45. Goldberg, T., Cai, W., Peppa, M., Dardaine, V., Baliga, B. S., Uribarri, J., and Vlassara, H. (2004) Advanced glycoxidation end products in commonly consumed foods. *J Am Diet Assoc* **104**, 1287-1291
46. Uribarri, J., Woodruff, S., Goodman, S., Cai, W., Chen, X., Pyzik, R., Yong, A., Striker, G. E., and Vlassara, H. (2010) Advanced glycation end products in foods and a practical guide to their reduction in the diet. *J Am Diet Assoc* **110**, 911-916 e912
47. Freund, M. A., Chen, B. C., and Decker, E. A. (2018) The Inhibition of Advanced Glycation End Products by Carnosine and Other Natural Dipeptides to Reduce Diabetic and Age-Related Complications. *Compr Rev Food Sci F* **17**, 1367-1378
48. Xue, J., Rai, V., Singer, D., Chabierski, S., Xie, J., Reverdatto, S., Burz, D. S., Schmidt, A. M., Hoffmann, R., and Shekhtman, A. (2011) Advanced glycation end product recognition by the receptor for AGEs. *Structure* **19**, 722-732
49. Fu, M. X., Requena, J. R., Jenkins, A. J., Lyons, T. J., Baynes, J. W., and Thorpe, S. R. (1996) The advanced glycation end product, Nepsilon-(carboxymethyl)lysine, is a product of both lipid peroxidation and glycoxidation reactions. *J Biol Chem* **271**, 9982-9986
50. Heier, M., Margeirsdottir, H. D., Torjesen, P. A., Seljeflot, I., Stensaeth, K. H., Gaarder, M., Brunborg, C., Hanssen, K. F., and Dahl-Jorgensen, K. (2015) The advanced glycation end product methylglyoxal-derived hydroimidazolone-1 and early signs of atherosclerosis in childhood diabetes. *Diab Vasc Dis Res* **12**, 139-145
51. Willemsen, S., Hartog, J. W., van Veldhuisen, D. J., van der Meer, P., Roze, J. F., Jaarsma, T., Schalkwijk, C., van der Horst, I. C., Hillege, H. L., and Voors, A. A. (2012) The role of advanced glycation end-products and their receptor on outcome in heart failure patients with preserved and reduced ejection fraction. *Am Heart J* **164**, 742-749 e743
52. Grillo, M. A., and Colombatto, S. (2008) Advanced glycation end-products (AGEs): involvement in aging and in neurodegenerative diseases. *Amino Acids* **35**, 29-36
53. Abedini, A., Derk, J., and Schmidt, A. M. (2018) The receptor for advanced glycation endproducts is a mediator of toxicity by IAPP and other proteotoxic aggregates: Establishing and exploiting common ground for novel amyloidosis therapies. *Protein Sci* **27**, 1166-1180
54. Del Monte, F., and Agnetti, G. (2014) Protein post-translational modifications and misfolding: new concepts in heart failure. *Proteomics Clin Appl* **8**, 534-542

55. Li, J., Liu, D., Sun, L., Lu, Y., and Zhang, Z. (2012) Advanced glycation end products and neurodegenerative diseases: mechanisms and perspective. *J Neurol Sci* **317**, 1-5
56. Castellani, R. J., Harris, P. L., Sayre, L. M., Fujii, J., Taniguchi, N., Vitek, M. P., Founds, H., Atwood, C. S., Perry, G., and Smith, M. A. (2001) Active glycation in neurofibrillary pathology of Alzheimer disease: N(epsilon)-(carboxymethyl) lysine and hexitol-lysine. *Free Radic Biol Med* **31**, 175-180
57. Southern, L., Williams, J., and Esiri, M. M. (2007) Immunohistochemical study of N-epsilon-carboxymethyl lysine (CML) in human brain: relation to vascular dementia. *BMC Neurol* **7**, 35
58. Valente, T., Gella, A., Fernandez-Busquets, X., Unzeta, M., and Durany, N. (2010) Immunohistochemical analysis of human brain suggests pathological synergism of Alzheimer's disease and diabetes mellitus. *Neurobiol Dis* **37**, 67-76
59. Zhang, Q., Monroe, M. E., Schepmoes, A. A., Clauss, T. R., Gritsenko, M. A., Meng, D., Petyuk, V. A., Smith, R. D., and Metz, T. O. (2011) Comprehensive identification of glycated peptides and their glycation motifs in plasma and erythrocytes of control and diabetic subjects. *J Proteome Res* **10**, 3076-3088
60. Ma, Z., Westermark, P., and Westermark, G. T. (2000) Amyloid in human islets of Langerhans: immunologic evidence that islet amyloid polypeptide is modified in amyloidogenesis. *Pancreas* **21**, 212-218
61. Lorenzo, A., Razzaboni, B., Weir, G. C., and Yankner, B. A. (1994) Pancreatic islet cell toxicity of amylin associated with type-2 diabetes mellitus. *Nature* **368**, 756-760
62. Vlassara, H., Brownlee, M., and Cerami, A. (1981) Nonenzymatic glycosylation of peripheral nerve protein in diabetes mellitus. *Proc Natl Acad Sci U S A* **78**, 5190-5192
63. Sasaki, N., Fukatsu, R., Tsuzuki, K., Hayashi, Y., Yoshida, T., Fujii, N., Koike, T., Wakayama, I., Yanagihara, R., Garruto, R., Amano, N., and Makita, Z. (1998) Advanced glycation end products in Alzheimer's disease and other neurodegenerative diseases. *Am J Pathol* **153**, 1149-1155
64. Haass, C., and Selkoe, D. J. (2007) Soluble protein oligomers in neurodegeneration: lessons from the Alzheimer's amyloid beta-peptide. *Nat Rev Mol Cell Biol* **8**, 101-112
65. LaFerla, F. M., Green, K. N., and Oddo, S. (2007) Intracellular amyloid-beta in Alzheimer's disease. *Nat Rev Neurosci* **8**, 499-509
66. Hardy, J., and Selkoe, D. J. (2002) The amyloid hypothesis of Alzheimer's disease: progress and problems on the road to therapeutics. *Science* **297**, 353-356
67. Aguzzi, A., and O'Connor, T. (2010) Protein aggregation diseases: pathogenicity and therapeutic perspectives. *Nat Rev Drug Discov* **9**, 237-248
68. Glenner, G. G., and Wong, C. W. (1984) Alzheimer's disease and Down's syndrome: sharing of a unique cerebrovascular amyloid fibril protein. *Biochem Biophys Res Commun* **122**, 1131-1135
69. Glenner, G. G., and Wong, C. W. (1984) Alzheimer's disease: initial report of the purification and characterization of a novel cerebrovascular amyloid protein. *Biochem Biophys Res Commun* **120**, 885-890
70. Shin, R. W., Iwaki, T., Kitamoto, T., and Tateishi, J. (1991) Hydrated autoclave pretreatment enhances tau immunoreactivity in formalin-fixed normal and Alzheimer's disease brain tissues. *Lab Invest* **64**, 693-702
71. Priller, C., Bauer, T., Mitteregger, G., Krebs, B., Kretzschmar, H. A., and Herms, J. (2006) Synapse formation and function is modulated by the amyloid precursor protein. *J Neurosci* **26**, 7212-7221

72. Turner, P. R., O'Connor, K., Tate, W. P., and Abraham, W. C. (2003) Roles of amyloid precursor protein and its fragments in regulating neural activity, plasticity and memory. *Prog Neurobiol* **70**, 1-32

73. Duce, J. A., Tsatsanis, A., Cater, M. A., James, S. A., Robb, E., Wikhe, K., Leong, S. L., Perez, K., Johanssen, T., Greenough, M. A., Cho, H. H., Galatis, D., Moir, R. D., Masters, C. L., McLean, C., Tanzi, R. E., Cappai, R., Barnham, K. J., Ciccotosto, G. D., Rogers, J. T., and Bush, A. I. (2010) Iron-export ferroxidase activity of beta-amyloid precursor protein is inhibited by zinc in Alzheimer's disease. *Cell* **142**, 857-867

74. Bertram, L., Lill, C. M., and Tanzi, R. E. (2010) The genetics of Alzheimer disease: back to the future. *Neuron* **68**, 270-281

75. Abelein, A., Abrahams, J. P., Danielsson, J., Graslund, A., Jarvet, J., Luo, J., Tiiman, A., and Warmlander, S. K. (2014) The hairpin conformation of the amyloid beta peptide is an important structural motif along the aggregation pathway. *J Biol Inorg Chem* **19**, 623-634

76. Barrett, P. J., Song, Y., Van Horn, W. D., Hustedt, E. J., Schafer, J. M., Hadziselimovic, A., Beel, A. J., and Sanders, C. R. (2012) The amyloid precursor protein has a flexible transmembrane domain and binds cholesterol. *Science* **336**, 1168-1171

77. Chen, G. F., Xu, T. H., Yan, Y., Zhou, Y. R., Jiang, Y., Melcher, K., and Xu, H. E. (2017) Amyloid beta: structure, biology and structure-based therapeutic development. *Acta Pharmacol Sin* **38**, 1205-1235

78. Talafous, J., Marcinowski, K. J., Klopman, G., and Zagorski, M. G. (1994) Solution structure of residues 1-28 of the amyloid beta-peptide. *Biochemistry* **33**, 7788-7796

79. Jarvet, J., Danielsson, J., Damberg, P., Oleszczuk, M., and Graslund, A. (2007) Positioning of the Alzheimer Abeta(1-40) peptide in SDS micelles using NMR and paramagnetic probes. *J Biomol NMR* **39**, 63-72

80. Shao, H., Jao, S., Ma, K., and Zagorski, M. G. (1999) Solution structures of micelle-bound amyloid beta-(1-40) and beta-(1-42) peptides of Alzheimer's disease. *J Mol Biol* **285**, 755-773

81. Dyson, H. J., and Wright, P. E. (2005) Intrinsically unstructured proteins and their functions. *Nat Rev Mol Cell Biol* **6**, 197-208

82. Jensen, M. R., Zweckstetter, M., Huang, J. R., and Blackledge, M. (2014) Exploring free-energy landscapes of intrinsically disordered proteins at atomic resolution using NMR spectroscopy. *Chem Rev* **114**, 6632-6660

83. Riek, R., Guntert, P., Dobeli, H., Wipf, B., and Wuthrich, K. (2001) NMR studies in aqueous solution fail to identify significant conformational differences between the monomeric forms of two Alzheimer peptides with widely different plaque-competence, A beta(1-40)(ox) and A beta(1-42)(ox). *Eur J Biochem* **268**, 5930-5936

84. Danielsson, J., Jarvet, J., Damberg, P., and Graslund, A. (2005) The Alzheimer beta-peptide shows temperature-dependent transitions between left-handed 3-helix, beta-strand and random coil secondary structures. *FEBS J* **272**, 3938-3949

85. Coles, M., Bicknell, W., Watson, A. A., Fairlie, D. P., and Craik, D. J. (1998) Solution structure of amyloid beta-peptide(1-40) in a water-micelle environment. Is the membrane-spanning domain where we think it is? *Biochemistry* **37**, 11064-11077

86. Zhang, S., Iwata, K., Lachenmann, M. J., Peng, J. W., Li, S., Stimson, E. R., Lu, Y., Felix, A. M., Maggio, J. E., and Lee, J. P. (2000) The Alzheimer's peptide a beta adopts a collapsed coil structure in water. *J Struct Biol* **130**, 130-141

87. Crescenzi, O., Tomaselli, S., Guerrini, R., Salvadori, S., D'Ursi, A. M., Temussi, P. A., and Picone, D. (2002) Solution structure of the Alzheimer amyloid beta-peptide (1-42) in an

apolar microenvironment. Similarity with a virus fusion domain. *Eur J Biochem* **269**, 5642-5648

88. D'Ursi, A. M., Armenante, M. R., Guerrini, R., Salvadori, S., Sorrentino, G., and Picone, D. (2004) Solution structure of amyloid beta-peptide (25-35) in different media. *J Med Chem* **47**, 4231-4238
89. Sgourakis, N. G., Yan, Y., McCallum, S. A., Wang, C., and Garcia, A. E. (2007) The Alzheimer's peptides Abeta40 and 42 adopt distinct conformations in water: a combined MD / NMR study. *J Mol Biol* **368**, 1448-1457
90. Vivekanandan, S., Brender, J. R., Lee, S. Y., and Ramamoorthy, A. (2011) A partially folded structure of amyloid-beta(1-40) in an aqueous environment. *Biochem Biophys Res Commun* **411**, 312-316
91. Mirza, Z., Pillai, V. G., and Kamal, M. A. (2014) Protein interactions between the C-terminus of Abeta-peptide and phospholipase A2--a structure biology based approach to identify novel Alzheimer's therapeutics. *CNS Neurol Disord Drug Targets* **13**, 1224-1231
92. Balbach, J. J., Petkova, A. T., Oyler, N. A., Antzutkin, O. N., Gordon, D. J., Meredith, S. C., and Tycko, R. (2002) Supramolecular structure in full-length Alzheimer's beta-amyloid fibrils: evidence for a parallel beta-sheet organization from solid-state nuclear magnetic resonance. *Biophys J* **83**, 1205-1216
93. Antzutkin, O. N., Leapman, R. D., Balbach, J. J., and Tycko, R. (2002) Supramolecular structural constraints on Alzheimer's beta-amyloid fibrils from electron microscopy and solid-state nuclear magnetic resonance. *Biochemistry* **41**, 15436-15450
94. Antzutkin, O. N., Balbach, J. J., Leapman, R. D., Rizzo, N. W., Reed, J., and Tycko, R. (2000) Multiple quantum solid-state NMR indicates a parallel, not antiparallel, organization of beta-sheets in Alzheimer's beta-amyloid fibrils. *Proc Natl Acad Sci U S A* **97**, 13045-13050
95. Luhrs, T., Ritter, C., Adrian, M., Riek-Loher, D., Bohrmann, B., Dobeli, H., Schubert, D., and Riek, R. (2005) 3D structure of Alzheimer's amyloid-beta(1-42) fibrils. *Proc Natl Acad Sci U S A* **102**, 17342-17347
96. Petkova, A. T., Yau, W. M., and Tycko, R. (2006) Experimental constraints on quaternary structure in Alzheimer's beta-amyloid fibrils. *Biochemistry* **45**, 498-512
97. Qiang, W., Yau, W. M., Luo, Y., Mattson, M. P., and Tycko, R. (2012) Antiparallel beta-sheet architecture in Iowa-mutant beta-amyloid fibrils. *Proc Natl Acad Sci U S A* **109**, 4443-4448
98. Colletier, J. P., Laganowsky, A., Landau, M., Zhao, M., Soriaga, A. B., Goldschmidt, L., Flot, D., Cascio, D., Sawaya, M. R., and Eisenberg, D. (2011) Molecular basis for amyloid-beta polymorphism. *Proc Natl Acad Sci U S A* **108**, 16938-16943
99. Ahmed, M., Davis, J., Aucoin, D., Sato, T., Ahuja, S., Aimoto, S., Elliott, J. I., Van Nostrand, W. E., and Smith, S. O. (2010) Structural conversion of neurotoxic amyloid-beta(1-42) oligomers to fibrils. *Nat Struct Mol Biol* **17**, 561-567
100. Abedini, A., Cao, P., Plesner, A., Zhang, J., He, M., Derk, J., Patil, S. A., Rosario, R., Lonier, J., Song, F., Koh, H., Li, H., Raleigh, D. P., and Schmidt, A. M. (2018) RAGE binds preamyloid IAPP intermediates and mediates pancreatic beta cell proteotoxicity. *J Clin Invest* **128**, 682-698
101. Qiang, W., Yau, W. M., and Tycko, R. (2011) Structural evolution of Iowa mutant beta-amyloid fibrils from polymorphic to homogeneous states under repeated seeded growth. *J Am Chem Soc* **133**, 4018-4029
102. Paravastu, A. K., Qahwash, I., Leapman, R. D., Meredith, S. C., and Tycko, R. (2009) Seeded growth of beta-amyloid fibrils from Alzheimer's brain-derived fibrils produces a distinct fibril structure. *Proc Natl Acad Sci U S A* **106**, 7443-7448

103. Bertini, I., Gonnelli, L., Luchinat, C., Mao, J., and Nesi, A. (2011) A new structural model of Abeta40 fibrils. *J Am Chem Soc* **133**, 16013-16022
104. Kahn, S. E., Cooper, M. E., and Del Prato, S. (2014) Pathophysiology and treatment of type 2 diabetes: perspectives on the past, present, and future. *Lancet* **383**, 1068-1083
105. Lukinius, A., Wilander, E., Westermark, G. T., Engstrom, U., and Westermark, P. (1989) Co-localization of islet amyloid polypeptide and insulin in the B cell secretory granules of the human pancreatic islets. *Diabetologia* **32**, 240-244
106. Kahn, S. E., Andrikopoulos, S., and Verchere, C. B. (1999) Islet amyloid: a long-recognized but underappreciated pathological feature of type 2 diabetes. *Diabetes* **48**, 241-253
107. Cooper, G. J., Willis, A. C., Clark, A., Turner, R. C., Sim, R. B., and Reid, K. B. (1987) Purification and characterization of a peptide from amyloid-rich pancreases of type 2 diabetic patients. *Proc Natl Acad Sci U S A* **84**, 8628-8632
108. Chen, M. S., Zhao, D. S., Yu, Y. P., Li, W. W., Chen, Y. X., Zhao, Y. F., and Li, Y. M. (2013) Characterizing the assembly behaviors of human amylin: a perspective derived from C-terminal variants. *Chem Commun (Camb)* **49**, 1799-1801
109. Muff, R., Born, W., Lutz, T. A., and Fischer, J. A. (2004) Biological importance of the peptides of the calcitonin family as revealed by disruption and transfer of corresponding genes. *Peptides* **25**, 2027-2038
110. Roberts, A. N., Leighton, B., Todd, J. A., Cockburn, D., Schofield, P. N., Sutton, R., Holt, S., Boyd, Y., Day, A. J., Foot, E. A., and et al. (1989) Molecular and functional characterization of amylin, a peptide associated with type 2 diabetes mellitus. *Proc Natl Acad Sci U S A* **86**, 9662-9666
111. Cottingham, I. R., Millar, A., Emslie, E., Colman, A., Schnieke, A. E., and McKee, C. (2001) A method for the amidation of recombinant peptides expressed as intein fusion proteins in Escherichia coli. *Nat Biotechnol* **19**, 974-977
112. Patil, S. M., Xu, S., Sheftic, S. R., and Alexandrescu, A. T. (2009) Dynamic alpha-helix structure of micelle-bound human amylin. *J Biol Chem* **284**, 11982-11991
113. Lutz, T. A. (2012) Control of energy homeostasis by amylin. *Cell Mol Life Sci* **69**, 1947-1965
114. Knight, J. D., Williamson, J. A., and Miranker, A. D. (2008) Interaction of membrane-bound islet amyloid polypeptide with soluble and crystalline insulin. *Protein Sci* **17**, 1850-1856
115. Jha, S., Snell, J. M., Sheftic, S. R., Patil, S. M., Daniels, S. B., Kolling, F. W., and Alexandrescu, A. T. (2014) pH dependence of amylin fibrillization. *Biochemistry* **53**, 300-310
116. Padrick, S. B., and Miranker, A. D. (2001) Islet amyloid polypeptide: identification of long-range contacts and local order on the fibrillogenesis pathway. *J Mol Biol* **308**, 783-794
117. Jaikaran, E. T., and Clark, A. (2001) Islet amyloid and type 2 diabetes: from molecular misfolding to islet pathophysiology. *Biochim Biophys Acta* **1537**, 179-203
118. Green, J., Goldsbury, C., Mini, T., Sunderji, S., Frey, P., Kistler, J., Cooper, G., and Aebi, U. (2003) Full-length rat amylin forms fibrils following substitution of single residues from human amylin. *J Mol Biol* **326**, 1147-1156
119. Goldsbury, C., Goldie, K., Pellaud, J., Seelig, J., Frey, P., Muller, S. A., Kistler, J., Cooper, G. J., and Aebi, U. (2000) Amyloid fibril formation from full-length and fragments of amylin. *J Struct Biol* **130**, 352-362
120. Abedini, A., and Raleigh, D. P. (2006) Destabilization of human IAPP amyloid fibrils by proline mutations outside of the putative amyloidogenic domain: is there a critical amyloidogenic domain in human IAPP? *J Mol Biol* **355**, 274-281
121. Koo, B. W., Hebda, J. A., and Miranker, A. D. (2008) Amide inequivalence in the fibrillar assembly of islet amyloid polypeptide. *Protein Eng Des Sel* **21**, 147-154

122. Zhou, S., Wang, Q., Ren, M., Zhang, A., Liu, H., and Yao, X. (2017) Molecular dynamics simulation on the inhibition mechanism of peptide-based inhibitor of islet amyloid polypeptide (IAPP) to islet amyloid polypeptide (IAPP22-28) oligomers. *Chem Biol Drug Des* **90**, 31-39
123. Khemtemourian, L., Guillemain, G., Foufelle, F., and Killian, J. A. (2017) Residue specific effects of human islet polypeptide amyloid on self-assembly and on cell toxicity. *Biochimie* **142**, 22-30
124. Moriarty, D. F., and Raleigh, D. P. (1999) Effects of sequential proline substitutions on amyloid formation by human amylin20-29. *Biochemistry* **38**, 1811-1818
125. Nilsson, M. R., and Raleigh, D. P. (1999) Analysis of amylin cleavage products provides new insights into the amyloidogenic region of human amylin. *J Mol Biol* **294**, 1375-1385
126. Jaikaran, E. T., Higham, C. E., Serpell, L. C., Zurdo, J., Gross, M., Clark, A., and Fraser, P. E. (2001) Identification of a novel human islet amyloid polypeptide beta-sheet domain and factors influencing fibrillogenesis. *J Mol Biol* **308**, 515-525
127. Cope, S. M., Shinde, S., Best, R. B., Ghirlanda, G., and Vaiana, S. M. (2013) Cyclic N-terminal loop of amylin forms non amyloid fibers. *Biophys J* **105**, 1661-1669
128. Bedrood, S., Li, Y., Isas, J. M., Hegde, B. G., Baxa, U., Haworth, I. S., and Langen, R. (2012) Fibril structure of human islet amyloid polypeptide. *J Biol Chem* **287**, 5235-5241
129. Goldsbury, C. S., Cooper, G. J., Goldie, K. N., Muller, S. A., Saafi, E. L., Gruijters, W. T., Misur, M. P., Engel, A., Aebi, U., and Kistler, J. (1997) Polymorphic fibrillar assembly of human amylin. *J Struct Biol* **119**, 17-27
130. Kajava, A. V., Aebi, U., and Steven, A. C. (2005) The parallel superpleated beta-structure as a model for amyloid fibrils of human amylin. *J Mol Biol* **348**, 247-252
131. Luca, S., Yau, W. M., Leapman, R., and Tycko, R. (2007) Peptide conformation and supramolecular organization in amylin fibrils: constraints from solid-state NMR. *Biochemistry* **46**, 13505-13522
132. O'Doherty, C. B., and Byrne, A. C. (2008) *Protein misfolding*, Nova Science Publishers, New York
133. Wiltzius, J. J., Sievers, S. A., Sawaya, M. R., Cascio, D., Popov, D., Riekel, C., and Eisenberg, D. (2008) Atomic structure of the cross-beta spine of islet amyloid polypeptide (amylin). *Protein Sci* **17**, 1467-1474
134. Alexandrescu, A. T. (2013) Amide proton solvent protection in amylin fibrils probed by quenched hydrogen exchange NMR. *PLoS One* **8**, e56467
135. Hirota-Nakaoka, N., Hasegawa, K., Naiki, H., and Goto, Y. (2003) Dissolution of beta2-microglobulin amyloid fibrils by dimethylsulfoxide. *J Biochem* **134**, 159-164
136. Hoshino, M., Katou, H., Yamaguchi, K., and Goto, Y. (2007) Dimethylsulfoxide-quenched hydrogen/deuterium exchange method to study amyloid fibril structure. *Biochim Biophys Acta* **1768**, 1886-1899
137. Abedini, A., and Raleigh, D. P. (2005) The role of His-18 in amyloid formation by human islet amyloid polypeptide. *Biochemistry* **44**, 16284-16291
138. Brender, J. R., Hartman, K., Reid, K. R., Kennedy, R. T., and Ramamoorthy, A. (2008) A single mutation in the nonamyloidogenic region of islet amyloid polypeptide greatly reduces toxicity. *Biochemistry* **47**, 12680-12688
139. Hard, T. (2014) Amyloid Fibrils: Formation, Polymorphism, and Inhibition. *J Phys Chem Lett* **5**, 607-614
140. Tycko, R. (2014) Physical and structural basis for polymorphism in amyloid fibrils. *Protein Sci* **23**, 1528-1539

141. Lo, T. W., Westwood, M. E., McLellan, A. C., Selwood, T., and Thornalley, P. J. (1994) Binding and modification of proteins by methylglyoxal under physiological conditions. A kinetic and mechanistic study with N alpha-acetylarginine, N alpha-acetylcysteine, and N alpha-acetyllysine, and bovine serum albumin. *J Biol Chem* **269**, 32299-32305
142. Vlassara, H. (1996) Protein glycation in the kidney: role in diabetes and aging. *Kidney Int* **49**, 1795-1804
143. Naiki, H., Higuchi, K., Hosokawa, M., and Takeda, T. (1989) Fluorometric determination of amyloid fibrils in vitro using the fluorescent dye, thioflavin T1. *Anal Biochem* **177**, 244-249
144. Naiki, H., Higuchi, K., Matsushima, K., Shimada, A., Chen, W. H., Hosokawa, M., and Takeda, T. (1990) Fluorometric examination of tissue amyloid fibrils in murine senile amyloidosis: use of the fluorescent indicator, thioflavine T. *Lab Invest* **62**, 768-773
145. Naiki, H., Higuchi, K., Nakakuki, K., and Takeda, T. (1991) Kinetic analysis of amyloid fibril polymerization in vitro. *Lab Invest* **65**, 104-110
146. LeVine, H., 3rd. (1993) Thioflavine T interaction with synthetic Alzheimer's disease beta-amyloid peptides: detection of amyloid aggregation in solution. *Protein Sci* **2**, 404-410
147. LeVine, H., 3rd. (1997) Stopped-flow kinetics reveal multiple phases of thioflavin T binding to Alzheimer beta (1-40) amyloid fibrils. *Arch Biochem Biophys* **342**, 306-316
148. Groenning, M. (2010) Binding mode of Thioflavin T and other molecular probes in the context of amyloid fibrils-current status. *J Chem Biol* **3**, 1-18
149. Dzwolak, W., and Pecul, M. (2005) Chiral bias of amyloid fibrils revealed by the twisted conformation of Thioflavin T: an induced circular dichroism/DFT study. *FEBS Lett* **579**, 6601-6603
150. Nelson, R., and Eisenberg, D. (2006) Recent atomic models of amyloid fibril structure. *Curr Opin Struct Biol* **16**, 260-265
151. Harel, M., Sonoda, L. K., Silman, I., Sussman, J. L., and Rosenberry, T. L. (2008) Crystal structure of thioflavin T bound to the peripheral site of Torpedo californica acetylcholinesterase reveals how thioflavin T acts as a sensitive fluorescent reporter of ligand binding to the acylation site. *J Am Chem Soc* **130**, 7856-7861
152. Makin, O. S., and Serpell, L. C. (2005) Structures for amyloid fibrils. *FEBS J* **272**, 5950-5961
153. Biancalana, M., Makabe, K., Koide, A., and Koide, S. (2008) Aromatic cross-strand ladders control the structure and stability of beta-rich peptide self-assembly mimics. *J Mol Biol* **383**, 205-213
154. Sabate, R., Lascu, I., and Saupe, S. J. (2008) On the binding of Thioflavin-T to HET-s amyloid fibrils assembled at pH 2. *J Struct Biol* **162**, 387-396
155. Xue, C., Lin, T. Y., Chang, D., and Guo, Z. (2017) Thioflavin T as an amyloid dye: fibril quantification, optimal concentration and effect on aggregation. *R Soc Open Sci* **4**, 160696
156. Khurana, R., Coleman, C., Ionescu-Zanetti, C., Carter, S. A., Krishna, V., Grover, R. K., Roy, R., and Singh, S. (2005) Mechanism of thioflavin T binding to amyloid fibrils. *J Struct Biol* **151**, 229-238
157. Loksztejn, A., and Dzwolak, W. (2008) Chiral bifurcation in aggregating insulin: an induced circular dichroism study. *J Mol Biol* **379**, 9-16
158. Krebs, M. R., Bromley, E. H., and Donald, A. M. (2005) The binding of thioflavin-T to amyloid fibrils: localisation and implications. *J Struct Biol* **149**, 30-37
159. Wu, C., Biancalana, M., Koide, S., and Shea, J. E. (2009) Binding modes of thioflavin-T to the single-layer beta-sheet of the peptide self-assembly mimics. *J Mol Biol* **394**, 627-633
160. Groenning, M., Olsen, L., van de Weert, M., Flink, J. M., Frokjaer, S., and Jorgensen, F. S. (2007) Study on the binding of Thioflavin T to beta-sheet-rich and non-beta-sheet cavities. *J Struct Biol* **158**, 358-369

161. Sen, P., Fatima, S., Ahmad, B., and Khan, R. H. (2009) Interactions of thioflavin T with serum albumins: spectroscopic analyses. *Spectrochim Acta A Mol Biomol Spectrosc* **74**, 94-99
162. Ruggeri, F. S., Sneideris, T., Vendruscolo, M., and Knowles, T. P. J. (2019) Atomic force microscopy for single molecule characterisation of protein aggregation. *Arch Biochem Biophys* **664**, 134-148
163. Bruker. (2003) SPM Training Notebook.
164. Glatzel, T., Holscher, H., Schimmel, T., Baykara, M. Z., Schwarz, U. D., and Garcia, R. (2012) Advanced atomic force microscopy techniques. *Beilstein J Nanotechnol* **3**, 893-894
165. Image from Wikipedia Common, C. G., CC-BY-SA-3.0.
166. Oroudjev, E., Soares, J., Arcdiacono, S., Thompson, J. B., Fossey, S. A., and Hansma, H. G. (2002) Segmented nanofibers of spider dragline silk: atomic force microscopy and single-molecule force spectroscopy. *Proc Natl Acad Sci U S A* **99 Suppl 2**, 6460-6465
167. D. Abramovitch, S. A., L. Pao, and G. Schitter. (2007) A tutorial on the mechanisms, dynamics, and control of atomic force microscopes. *American Control Conference*, 3488–3502
168. Joshi, M. (2009) IUPAB sponsored Workshop on NMR & its. Applications in Biological Systems.
169. Kellum, M. W., Oray, B., and Norton, S. J. (1978) A convenient quantitative synthesis of methylglyoxal for glyoxalase I assays. *Anal Biochem* **85**, 586-590
170. Williamson, J. A., and Miranker, A. D. (2007) Direct detection of transient alpha-helical states in islet amyloid polypeptide. *Protein Sci* **16**, 110-117
171. Rodriguez Camargo, D. C., Tripsianes, K., Kapp, T. G., Mendes, J., Schubert, J., Cordes, B., and Reif, B. (2015) Cloning, expression and purification of the human Islet Amyloid Polypeptide (hIAPP) from Escherichia coli. *Protein Expr Purif* **106**, 49-56
172. Zagorski, M. G., Yang, J., Shao, H., Ma, K., Zeng, H., and Hong, A. (1999) Methodological and chemical factors affecting amyloid beta peptide amyloidogenicity. *Methods Enzymol* **309**, 189-204
173. Chen, S., and Wetzel, R. (2001) Solubilization and disaggregation of polyglutamine peptides. *Protein Sci* **10**, 887-891
174. Emendato, A., Spadaccini, R., De Santis, A., Guerrini, R., D'Errico, G., and Picone, D. (2016) Preferential interaction of the Alzheimer peptide Abeta-(1-42) with Omega-3-containing lipid bilayers: structure and interaction studies. *FEBS Lett* **590**, 582-591
175. Fica-Contreras, S. M., Shuster, S. O., Durfee, N. D., Bowe, G. J. K., Henning, N. J., Hill, S. A., Vrla, G. D., Stillman, D. R., Suralik, K. M., Sandwick, R. K., and Choi, S. (2017) Glycation of Lys-16 and Arg-5 in amyloid-beta and the presence of Cu(2+) play a major role in the oxidative stress mechanism of Alzheimer's disease. *J Biol Inorg Chem* **22**, 1211-1222
176. Beisswenger, P. J., Howell, S., Mackenzie, T., Corstjens, H., Muizzuddin, N., and Matsui, M. S. (2012) Two fluorescent wavelengths, 440(ex)/520(em) nm and 370(ex)/440(em) nm, reflect advanced glycation and oxidation end products in human skin without diabetes. *Diabetes Technol Ther* **14**, 285-292
177. Oliveira MIA, M. d. S. E., de Oliveira Pedrosa F, Roginski Réa R, da Silva Couto Alves A, Picheth G; Gomes de Moraes Rego F. (2013) RAGE receptor and its soluble isoforms in diabetes mellitus complications. *J Bras Patol Med Lab* **49**, 97-108
178. Thornalley, P. J. (2005) Dicarbonyl intermediates in the maillard reaction. *Ann N Y Acad Sci* **1043**, 111-117
179. Pampati, P. K., Suravajjala, S., and Dain, J. A. (2011) Monitoring nonenzymatic glycation of human immunoglobulin G by methylglyoxal and glyoxal: A spectroscopic study. *Anal Biochem* **408**, 59-63

180. Jarrett, J. T., Berger, E. P., and Lansbury, P. T., Jr. (1993) The carboxy terminus of the beta amyloid protein is critical for the seeding of amyloid formation: implications for the pathogenesis of Alzheimer's disease. *Biochemistry* **32**, 4693-4697
181. Burdick, D., Soreghan, B., Kwon, M., Kosmoski, J., Knauer, M., Henschen, A., Yates, J., Cotman, C., and Glabe, C. (1992) Assembly and aggregation properties of synthetic Alzheimer's A4/beta amyloid peptide analogs. *J Biol Chem* **267**, 546-554
182. Linse, S. (2017) Monomer-dependent secondary nucleation in amyloid formation. *Biophys Rev* **9**, 329-338
183. Lapolla, A., Fedele, D., Seraglia, R., and Traldi, P. (2006) The role of mass spectrometry in the study of non-enzymatic protein glycation in diabetes: an update. *Mass Spectrom Rev* **25**, 775-797
184. Prasad, L., Leduc, Y., Hayakawa, K., and Delbaere, L. T. (2004) The structure of a universally employed enzyme: V8 protease from Staphylococcus aureus. *Acta Crystallogr D Biol Crystallogr* **60**, 256-259
185. Uotila, L., and Koivusalo, M. (1975) Purification and properties of glyoxalase I from sheep liver. *Eur J Biochem* **52**, 493-503
186. Nemet, I., Vikic-Topic, D., and Varga-Defterdarovic, L. (2004) Spectroscopic studies of methylglyoxal in water and dimethylsulfoxide. *Bioorg Chem* **32**, 560-570
187. Behbahani, M. (2014) Anti-HIV-1 activity of eight monofloral Iranian honey types. *PLoS One* **9**, e108195
188. Donarski, J. A., Roberts, D. P. T., and Charlton, A. J. (2010) Quantitative NMR spectroscopy for the rapid measurement of methylglyoxal in manuka honey. *Anal Methods-Uk* **2**, 1479-1483
189. Abedini, A., Plesner, A., Cao, P., Ridgway, Z., Zhang, J., Tu, L. H., Middleton, C. T., Chao, B., Sartori, D. J., Meng, F., Wang, H., Wong, A. G., Zanni, M. T., Verchere, C. B., Raleigh, D. P., and Schmidt, A. M. (2016) Time-resolved studies define the nature of toxic IAPP intermediates, providing insight for anti-amyloidosis therapeutics. *Elife* **5**
190. Paul, A., Kalita, S., Kalita, S., Sukumar, P., and Mandal, B. (2017) Disaggregation of Amylin Aggregate by Novel Conformationally Restricted Aminobenzoic Acid containing alpha/beta and alpha/gamma Hybrid Peptidomimetics. *Sci Rep* **7**, 40095
191. Higham, C. E., Jaikaran, E. T., Fraser, P. E., Gross, M., and Clark, A. (2000) Preparation of synthetic human islet amyloid polypeptide (IAPP) in a stable conformation to enable study of conversion to amyloid-like fibrils. *FEBS Lett* **470**, 55-60
192. Mishra, R., Geyer, M., and Winter, R. (2009) NMR spectroscopic investigation of early events in IAPP amyloid fibril formation. *Chembiochem* **10**, 1769-1772
193. Bjellqvist, B., Hughes, G. J., Pasquali, C., Paquet, N., Ravier, F., Sanchez, J. C., Frutiger, S., and Hochstrasser, D. (1993) The focusing positions of polypeptides in immobilized pH gradients can be predicted from their amino acid sequences. *Electrophoresis* **14**, 1023-1031
194. Emendato, A., Milordini, G., Zacco, E., Sicorello, A., Dal Piaz, F., Guerrini, R., Thorogate, R., Picone, D., and Pastore, A. (2018) Glycation affects fibril formation of Abeta peptides. *J Biol Chem* **293**, 13100-13111
195. Frye, E. B., Degenhardt, T. P., Thorpe, S. R., and Baynes, J. W. (1998) Role of the Maillard reaction in aging of tissue proteins. Advanced glycation end product-dependent increase in imidazolium cross-links in human lens proteins. *J Biol Chem* **273**, 18714-18719
196. Sadigh-Eteghad, S., Sabermarouf, B., Majdi, A., Talebi, M., Farhoudi, M., and Mahmoudi, J. (2015) Amyloid-beta: a crucial factor in Alzheimer's disease. *Med Princ Pract* **24**, 1-10
197. Gandy, S., Simon, A. J., Steele, J. W., Lublin, A. L., Lah, J. J., Walker, L. C., Levey, A. I., Krafft, G. A., Levy, E., Checler, F., Glabe, C., Bilker, W. B., Abel, T., Schmeidler, J., and Ehrlich, M. E.

(2010) Days to criterion as an indicator of toxicity associated with human Alzheimer amyloid-beta oligomers. *Ann Neurol* **68**, 220-230

198. Glabe, C. G. (2006) Common mechanisms of amyloid oligomer pathogenesis in degenerative disease. *Neurobiol Aging* **27**, 570-575

199. Paranjape, G. S., Gouwens, L. K., Osborn, D. C., and Nichols, M. R. (2012) Isolated amyloid-beta(1-42) protofibrils, but not isolated fibrils, are robust stimulators of microglia. *ACS Chem Neurosci* **3**, 302-311

200. Li, X. H., Du, L. L., Cheng, X. S., Jiang, X., Zhang, Y., Lv, B. L., Liu, R., Wang, J. Z., and Zhou, X. W. (2013) Glycation exacerbates the neuronal toxicity of beta-amyloid. *Cell Death Dis* **4**, e673

201. Kuhla, B., Loske, C., Garcia De Arriba, S., Schinzel, R., Huber, J., and Munch, G. (2004) Differential effects of "Advanced glycation endproducts" and beta-amyloid peptide on glucose utilization and ATP levels in the neuronal cell line SH-SY5Y. *J Neural Transm (Vienna)* **111**, 427-439

202. Uribarri, J., Cai, W., Peppa, M., Goodman, S., Ferrucci, L., Striker, G., and Vlassara, H. (2007) Circulating glycotoxins and dietary advanced glycation endproducts: two links to inflammatory response, oxidative stress, and aging. *J Gerontol A Biol Sci Med Sci* **62**, 427-433

203. Haan, M. N. (2006) Therapy Insight: type 2 diabetes mellitus and the risk of late-onset Alzheimer's disease. *Nat Clin Pract Neurol* **2**, 159-166

204. Dear, D. V., Young, D. S., Kazlauskaite, J., Meersman, F., Oxley, D., Webster, J., Pinheiro, T. J., Gill, A. C., Bronstein, I., and Lowe, C. R. (2007) Effects of post-translational modifications on prion protein aggregation and the propagation of scrapie-like characteristics in vitro. *Biochim Biophys Acta* **1774**, 792-802

205. Lee, D., Park, C. W., Paik, S. R., and Choi, K. Y. (2009) The modification of alpha-synuclein by dicarbonyl compounds inhibits its fibril-forming process. *Biochim Biophys Acta* **1794**, 421-430

206. Oliveira, L. M., Lages, A., Gomes, R. A., Neves, H., Familia, C., Coelho, A. V., and Quintas, A. (2011) Insulin glycation by methylglyoxal results in native-like aggregation and inhibition of fibril formation. *BMC Biochem* **12**, 41

207. Oliveira, L. M., Gomes, R. A., Yang, D., Dennison, S. R., Familia, C., Lages, A., Coelho, A. V., Murphy, R. M., Phoenix, D. A., and Quintas, A. (2013) Insights into the molecular mechanism of protein native-like aggregation upon glycation. *Biochim Biophys Acta* **1834**, 1010-1022

208. Singh, S. M., Hutchings, R. L., and Mallela, K. M. (2011) Mechanisms of m-cresol-induced protein aggregation studied using a model protein cytochrome c. *J Pharm Sci* **100**, 1679-1689

209. Vitek, M. P., Bhattacharya, K., Glendening, J. M., Stopa, E., Vlassara, H., Bucala, R., Manogue, K., and Cerami, A. (1994) Advanced glycation end products contribute to amyloidosis in Alzheimer disease. *Proc Natl Acad Sci U S A* **91**, 4766-4770

210. Nomoto, K. (2013) Identification of Advanced Glycation Endproducts derived fluorescence spectrum in vitro and human skin. *Anti-Aging Med* **10**, 92-100

211. Jana, A. K., Batkulwar, K. B., Kulkarni, M. J., and Sengupta, N. (2016) Glycation induces conformational changes in the amyloid-beta peptide and enhances its aggregation propensity: molecular insights. *Phys Chem Chem Phys* **18**, 31446-31458

212. Meier, J. J., Kayed, R., Lin, C. Y., Gurlo, T., Haataja, L., Jayasinghe, S., Langen, R., Glabe, C. G., and Butler, P. C. (2006) Inhibition of human IAPP fibril formation does not prevent beta-

cell death: evidence for distinct actions of oligomers and fibrils of human IAPP. *Am J Physiol Endocrinol Metab* **291**, E1317-1324

213. Vicente Miranda, H., Szego, E. M., Oliveira, L. M. A., Breda, C., Darendelioglu, E., de Oliveira, R. M., Ferreira, D. G., Gomes, M. A., Rott, R., Oliveira, M., Munari, F., Enguita, F. J., Simoes, T., Rodrigues, E. F., Heinrich, M., Martins, I. C., Zamolo, I., Riess, O., Cordeiro, C., Ponces-Freire, A., Lashuel, H. A., Santos, N. C., Lopes, L. V., Xiang, W., Jovin, T. M., Penque, D., Engelender, S., Zweckstetter, M., Klucken, J., Giorgini, F., Quintas, A., and Outeiro, T. F. (2017) Glycation potentiates alpha-synuclein-associated neurodegeneration in synucleinopathies. *Brain* **140**, 1399-1419
214. Wei, Y., Chen, L., Chen, J., Ge, L., and He, R. Q. (2009) Rapid glycation with D-ribose induces globular amyloid-like aggregations of BSA with high cytotoxicity to SH-SY5Y cells. *BMC Cell Biol* **10**, 10
215. Brownlee, M. (1992) Glycation products and the pathogenesis of diabetic complications. *Diabetes Care* **15**, 1835-1843
216. Munch, G., Schicktanz, D., Behme, A., Gerlach, M., Riederer, P., Palm, D., and Schinzel, R. (1999) Amino acid specificity of glycation and protein-AGE crosslinking reactivities determined with a dipeptide SPOT library. *Nat Biotechnol* **17**, 1006-1010
217. Hashimoto, N., Naiki, H., and Gejyo, F. (1999) Modification of beta 2-microglobulin with D-glucose or 3-deoxyglucosone inhibits A beta 2M amyloid fibril extension in vitro. *Amyloid* **6**, 256-264
218. Alavi, P., Yousefi, R., Amirghofran, S., Karbalaei-Heidari, H. R., and Moosavi-Movahedi, A. A. (2013) Structural analysis and aggregation propensity of reduced and nonreduced glycated insulin adducts. *Appl Biochem Biotechnol* **170**, 623-638
219. Zhu, M., Souillac, P. O., Ionescu-Zanetti, C., Carter, S. A., and Fink, A. L. (2002) Surface-catalyzed amyloid fibril formation. *J Biol Chem* **277**, 50914-50922
220. Dunkelberger, E. B., Buchanan, L. E., Marek, P., Cao, P., Raleigh, D. P., and Zanni, M. T. (2012) Deamidation accelerates amyloid formation and alters amylin fiber structure. *J Am Chem Soc* **134**, 12658-12667
221. Nguyen, P. T., Zottig, X., Sebastiao, M., and Bourgault, S. (2017) Role of Site-Specific Asparagine Deamidation in Islet Amyloid Polypeptide Amyloidogenesis: Key Contributions of Residues 14 and 21. *Biochemistry* **56**, 3808-3817
222. Macfarlane, W. M., Campbell, S. C., Elrick, L. J., Oates, V., Bermano, G., Lindley, K. J., Aynsley-Green, A., Dunne, M. J., James, R. F., and Docherty, K. (2000) Glucose regulates islet amyloid polypeptide gene transcription in a PDX1- and calcium-dependent manner. *J Biol Chem* **275**, 15330-15335
223. Haataja, L., Gurlo, T., Huang, C. J., and Butler, P. C. (2008) Islet amyloid in type 2 diabetes, and the toxic oligomer hypothesis. *Endocr Rev* **29**, 303-316
224. Kiriyama, Y., and Nochi, H. (2018) Role and Cytotoxicity of Amylin and Protection of Pancreatic Islet beta-Cells from Amylin Cytotoxicity. *Cells* **7**
225. Mukherjee, A., Morales-Scheihing, D., Salvadores, N., Moreno-Gonzalez, I., Gonzalez, C., Taylor-Presse, K., Mendez, N., Shahnawaz, M., Gaber, A. O., Sabek, O. M., Fraga, D. W., and Soto, C. (2017) Induction of IAPP amyloid deposition and associated diabetic abnormalities by a prion-like mechanism. *J Exp Med* **214**, 2591-2610
226. Gotz, J., Ittner, L. M., and Lim, Y. A. (2009) Common features between diabetes mellitus and Alzheimer's disease. *Cell Mol Life Sci* **66**, 1321-1325
227. Smith, M. A., Taneda, S., Richey, P. L., Miyata, S., Yan, S. D., Stern, D., Sayre, L. M., Monnier, V. M., and Perry, G. (1994) Advanced Maillard reaction end products are associated with Alzheimer disease pathology. *Proc Natl Acad Sci U S A* **91**, 5710-5714

228. Yan, S. D., Chen, X., Fu, J., Chen, M., Zhu, H., Roher, A., Slattery, T., Zhao, L., Nagashima, M., Morser, J., Migheli, A., Nawroth, P., Stern, D., and Schmidt, A. M. (1996) RAGE and amyloid-beta peptide neurotoxicity in Alzheimer's disease. *Nature* **382**, 685-691
229. Cao, D., Lu, H., Lewis, T. L., and Li, L. (2007) Intake of sucrose-sweetened water induces insulin resistance and exacerbates memory deficits and amyloidosis in a transgenic mouse model of Alzheimer disease. *J Biol Chem* **282**, 36275-36282
230. tool, P. *https://web.expasy.org/protparam/*